공학박사 학위논문

A Study of Intercalation Kinetics and Electrodeposition Behavior of Zinc for High Performance Aqueous Zinc Ion Batteries

고성능 수계 아연 이차전지를 위한
아연 삽입/탈리 및 전착 연구

2020년 8월

서울대학교 대학원
화학생물공학부
신 재 호

Abstract

A Study of Intercalation Kinetics and Electrodeposition Behavior of Zinc for High Performance Aqueous Zinc Ion Batteries

Jaeho Shin
School of Chemical and Biological Engineering
Seoul National University

Aqueous zinc ion batteries (AZIBs) are an emerging field of rechargeable battery technology that address certain issues of commercial lithium-ion batteries (LIBs). Safety is at the top of this list. Most commercial LIBs contain liquid electrolytes based on organic solvents, which are considered to be fire accelerants due to their combustible nature. In the event of a fire (due to a massive short circuit or abusive conditions), the mere presence of such electrolyte solutions can exacerbate its consequences, potentially harming consumers and/or innocent bystanders. However, the risk of fire hazards can be minimized by replacing organic solvents with non-combustible ones. Water is a prime example of such a solvent. Thus, the use of aqueous electrolytes can neutralize the risk of catastrophic fires. In this regard, AZIBs are considered to be promising post-LIB candidates.

A typical AZIB consists of a zinc (Zn) metal anode, aqueous electrolyte, separator, and an (in)organic cathode material. This configuration is analogous to the LIB half-cell, which is composed of Li metal (anode), organic electrolyte, polymer separator, and a (de)intercalation cathode. However, as the emergence of AZIB-related research is considerably later than that of LIBs, the AZIB system faces many hurdles before it can become a reliable, high performance battery. Two paths for research dominate this effort: i) discovery and analysis of viable cathode materials and ii) promoting the reversibility of Zn anodes.

First, discovering new materials for reversible reactions with Zn^{2+} ions constitutes an important research direction. Transition metal oxides are the mainstream cluster of materials that are explored for either intercalation or conversion, most of which are based on manganese (Mn) or vanadium (V). In particular, V-oxides are known to exist in numerous polymorphs, offering a wide range of possibilities for exploring Zn^{2+} (de)intercalation. In this study, V_6O_{13} was discovered to be a promising material for AZIB cathodes. Electrochemical analyses of V_6O_{13} resulted in high capacity levels (~ 400 mAh g^{-1}), rate performance (~ 140 mAh g^{-1} at 24 A g^{-1}), and cycling stability (~ 93% capacity retention after 2000 cycles at 4 A g^{-1}). *In situ* X-ray diffraction (XRD) studies *via* synchrotron radiation were employed to investigate the structural dynamics of this material, revealing single-phase behavior upon (dis)charge.

Further analyses coupled with density functional theory (DFT) calculations suggest the critical role of water during Zn^{2+} (de)intercalation, whereby water co-intercalates with Zn^{2+} to mitigate the de-solvation energy penalty at the electrode-electrolyte interface as well as shields the highly charged Zn^{2+} ion from electrostatic interactions with oxygen atoms in the host crystal. This is coined as "hydrated intercalation," a phenomenon which is believed to account for the anomalously high electrochemical performance in aqueous settings.

Second, while preliminary research into AZIBs mainly focused on cathode materials, more researchers have begun to realize the importance of the anode—Zn metal. In studies that pertain to cathodes, Zn metal is often employed in excess to minimize the impact of the anode on cell performance. Consequently, Zn anodes have rarely been the focus of AZIB-related investigations. However, concerns for energy density and performance have led many to account for Zn anodes, which are actually quite problematic upon close examination. In fact, while Zn metal is often lauded for its advantages in aqueous conditions, recent investigations reveal that Zn anodes suffer from several problems such as hydrogen evolution, dendritic growth, and corrosion. The consequences of such issues have not been recognized in previous studies. However, considering the myriad of cathode-related works thusfar, the time is ripe for dealing with Zn anodes. Accordingly, the merits and problems of Zn metal are discussed in detail with respect to AZIB applications. Representative strategies to resolve the main issues of Zn anodes are categorized and examined

to extract key lessons and insights in order to guide future research in this field. Moreover, rough energy density calculations are performed to ascertain the impact of the amount of Zn at the anode, showing significant differences in energy density. Thus, considering practical conditions, effective strategies to maximize Zn utilization are desirable for energy-dense AZIBs.

This dissertation is divided into four chapters. The first chapter introduces the concept and history of aqueous rechargeable batteries (ARBs), where a socio-technological context is established to discuss the reality and future opportunities of ARBs in the battery market in terms of scientific merit. Prospective aqueous battery chemistries are proposed, among which AZIBs are most promising for grid-scale energy storage system (ESS) applications. The second chapter is dedicated to the study of a promising AZIB cathode, V_6O_{13}, and its peculiar hydrated intercalation mechanism. The third chapter focuses on Zn metal anodes, a previously neglected topic in the field of AZIBs. Energy density and Coulombic efficiency calculations emphasize the role of reversible Zn anodes in realizing practically relevant AZIBs. Finally, the fourth chapter summarizes the key findings and insights from the previous chapters, suggesting prospective directions for future research.

Keywords: aqueous zinc battery, aqueous electrolyte, energy storage system, hydrated intercalation, zinc anode, in situ X-ray diffraction, vanadium oxide

Student number: 2018-36496

Table of Contents

List of Tables

List of Figures

1. Introduction

1.1 Why aqueous?

Despite the prevalence of LIBs in the global battery market, they are not free from certain drawbacks such as safety and slow charging rates. Such shortcomings have prompted research into alternative battery chemistries that address these issues. In this sense, ARBs have recently begun to garner academic interest as post-LIB systems due to the attractive features of water-based electrolytes.[1] Not only is water resistant to fire hazards, but its inherently higher ionic conductivity (compared to organic solvents) can also facilitate high rate battery operation.[2] Moreover, water is highly accessible, easy to handle, and capable of dissolving many salts. In addition, one can expect less initial fixed costs for dry room installation and maintenance from a manufacturing viewpoint. Thus, water serves as a versatile platform for which a wide variety of cost-effective electrolyte solutions can be formulated for specific battery chemistries. Such attractive features of aqueous electrolytes have inspired numerous works in ARBs, most of which can be categorized based on the main charge carrier ion. Representative categories include Li^+,[3] Na^+,[4] K^+,[5] Mg^{2+},[6] Zn^{2+},[7] OH^-,[8] H^+,[9] and sometimes a combination of two[10] for hybrid systems.

Ironically, what makes ARBs safe and fast limits their energy. Water is notorious (from a battery perspective) for its narrow electrochemical window, outside of which unwanted gas evolution reactions can occur. The

thermodynamic value of this window is 1.23 V, although kinetic considerations may extend this limit. Even so, this range is quite narrow compared to that of commercial LIBs, imposing a lower ceiling on the energy density [Wh kg^{-1} or Wh L^{-1}] of ARBs. In more tangible terms, this translates to shorter usage time or driving distance of devices/vehicles per charge.

These distinct pros and cons of ARBs pose a crucial question: are ARBs worth the effort? Answering this question entails a careful examination of the circumstances that have shaped the reality for non-LIBs such as ARBs, shining a light on opportunities that may guide future works in this field. A brief history of rechargeable batteries is provided to establish a socio-technological context, upon which the current position of ARBs in relation to modern battery technology is discusses. In this framework, viable directions and opportunities for commercial applications of ARBs can be put forth.

1.2 A brief history of ARBs

1.2.1 *Classical batteries – Pb-acid, Ni-Cd, Ni-metal hydride*

The history of ARBs dates much further back than the LIB, which was commercialized only three decades ago. In fact, given their relatively longer history, ARBs were the dominant players in the battery market. The origins of the first rechargeable battery—which was aqueous—can be traced back to the mid-19th century (**Figure 1-1**). In 1859, Gaston Planté first demonstrated the concept of rechargeable lead-acid batteries,[11] which are designed with the Pb

|| H_2SO_4 || PbO_2 configuration as depicted in **Figure 1-2a**. During discharge, the positive electrode (PbO_2) is reduced to form $PbSO_4$, while the negative electrode is oxidized to form the same compound, $PbSO_4$. Recharging this system is merely reversing the reactions at each electrode, returning them to their initial state.

Surprisingly, the 160-year-old lead-acid battery technology remains steadfast in commercial use today. While its low energy density levels ranging from 30−40 Wh kg^{-1} (this value may be lower depending on cell packaging or how the cell is defined)[12] prevent its use in electric vehicle (EV) applications, its unparalleled cost-effectiveness has locked its dominant position in markets such as starting batteries for cars and power sources for golf carts and wheelchairs. Despite additional drawbacks such as limited cyclability, slow charging, and the requirement of regular maintenance, a cost-effective alternative for such applications has yet to emerge. Thus, lead-acid batteries have been able to retain a market share where more recent batteries would be too expensive.

Lead-acid batteries were followed by nickel-cadmium (Ni-Cd) rechargeable batteries (**Figure 1-2b**), which were first created in 1901 by Waldemar Jungner.[13] Ni-Cd batteries offer higher energy densities of 40-60 Wh kg^{-1} with the notable advantage of being resilient to high rate operations, which prompted their use in a number of applications such as power tools,

photography equipment, and early mobile phone models. However, Ni-Cd batteries have two critical drawbacks which caused them to fall out of favor: the notorious “memory effect” and the toxicity of Cd. Some niches may still exist where the Ni-Cd technology may be unbeatable, but its share of the battery pie in the past few decades has been minimal and continues to fade.

Nickel-metal hydride (Ni-MH) batteries were quick to succeed the throne (**Figure 1-2c**). Ni-MH batteries were first conceptualized in 1967 and became commercially available two decades after.[14] The Ni-MH battery quickly became popular due to its absence of Cd and heightened energy density. Instead of the Cd electrode, the Ni-MH battery takes advantage of a metal alloy capable of absorbing hydrogen. Upon discharge, the hydrogen de-intercalates from the metal hydride, combining with hydroxide ions to form water. Simultaneously, the Ni electrode is reduced from NiOOH to $Ni(OH)_2$, identical to the cathodic reaction in Ni-Cd batteries.

This electrochemistry allowed Ni-MH batteries to attain higher energy density levels that were previously unachievable in lead-acid and Ni-Cd batteries. They quickly penetrated the battery market, becoming the go-to battery for consumer electronics. More importantly, Ni-MH batteries were used in the first hybrid-electric vehicles—the Toyota Prius—and first generation all-electric vehicles such as the GM EV1 and Honda EV Plus. However, LIBs soon emerged as a fierce contender in the battery market, quickly dethroning the Ni-MH battery with respect to EVs. Nevertheless, Ni-MH batteries are still widely

available as small rechargeable batteries and some hybrid electric vehicles even today.

1.2.2 *The emergence of LIBs*

LIBs, though sometimes taken for granted, were a game-changer to the battery industry. Ironically, the first demonstration of a LIB came from Exxon, a U.S. oil company. M. Stanley Whittingham is credited with the discovery, who began working on materials for lithium (Li) intercalation at Exxon in the early 1970s. Coincidentally, the historic 1973 oil crisis prompted the U.S. government to support research and development in electric and hybrid electric vehicles, lending support to alternative energy storage technology like LIBs. Whittingham discovered that Li could be reversibly (de)intercalated into (from) TiS_2 and demonstrated its potential by pairing it with a Li metal anode.[15] A few years later, John B. Goodenough showed that replacing TiS_2 with $LiCoO_2$, a layered transition metal oxide, could boost the operating voltage of LIBs.[16] However, the prototype LIB at that time used Li metal as the anode, which limited its performance in practical conditions. It was not until Akira Yoshino discovered that carbonaceous materials could (de)intercalate Li ions at the anode that a relatively safe and reliable LIB prototype was born for the first time. This was 1986.[17]

Not long after, Sony succeeded in commercializing the LIB in 1991. The initial battery had an energy density of 80 Wh kg^{-1}, which is considerably

low in today's standards and comparable with the Ni-MH battery. However, this value quickly rose to unprecedented levels with continued advances in materials chemistry, electrolyte formulation, and cell engineering. Such progress can be linked with many socio-technological trends at the time, but the rapid expansion of the EV market is the protagonist in this story.

The 1990s signifies a time of increasing environmental awareness that renewed interest in EVs, exemplified by the passage of the Clean Air Act Amendment (1990) and the Energy Policy Act (1992) in the U.S. However, interest in EVs was barely trending in spite of such legislative efforts. In fact, it was not until the year 2008 when the race to dominate the EV market truly began. In 2008, Tesla Motors (now Tesla, Inc.) rolled out its first EV, the Tesla Roadster, which was the first highway-capable EV to use LIBs (120 Wh kg^{-1}). Even by today's standards, the Roadster showed an impressive driving distance of 390 km (Environmental Protection Agency combined cycle). This came as a shock to the automobile industry, considering that a small start-up company out of Silicon Valley achieved what large automakers deemed out of reach at the time. Soon enough, automakers worldwide began to join the wagon, raising expectations for a new market with explosive potential.

Today, a rapidly expanding EV market has intensified competition among the major players in the automobile industry, each hoping to establish a strong foothold. A competitive edge in this market calls for, above all, cars with

longer driving distance per charge. For most consumers, this is the primary criteria for comparing EVs, which is directly linked to battery energy density. Simply put, the higher the energy density of a battery is, the more batteries can be installed in a vehicle. This increases the total energy of the vehicle, resulting in longer driving distances. Therefore, the competition among major EV manufacturers is translated to the battery industry; the most energy-dense, safe, and long-lasting battery would prove most attractive to original equipment manufacturers (OEMs).

Over the course of 160 years, the rechargeable battery industry has often been closely intertwined with socio-technological trends of the time. Before the 1990s, interest in EVs was intermittent. Market demand for batteries may have been more consistent, but their performance requirements were lenient. Thus, advances in rechargeable battery technology were incremental. It was only after the 1990s when unwavering commercial interest in EVs took hold, calling for better batteries. A similar trend emerged in consumer electronics as societal demand for mobile technology was beginning to simmer. While it is difficult to define a causal relationship between socio-technological trends and advances in science, the bond between rechargeable batteries and their target technologies has been, and always will be, inseparable. The limits of LIBs continue to be pushed today, culminating in a compulsive demand for higher energy density levels for a wide spectrum of applications. Today, LIB

energy densities approach 250 Wh kg^{-1} for EV applications at the cell level (**Figure 1-3**).

1.3 Reality of ARBs

A brief overview of the history of rechargeable batteries provides a valuable context in which we can consider the position of ARBs. The current battery industry relies mostly on LIBs for high energy applications, but there are niche markets where well-established, old-school battery technology such as lead acid and Ni-MH batteries are a better fit in terms of performance and/or cost. In this context, we may begin to discuss the status and prospects of ARBs.

Most ARB-related research today benchmark LIBs by involving intercalation at either one or both electrodes. Such a trend probably reflects the difficulty of making significant breakthroughs in more classical ARBs (e.g. lead-acid or Ni-MH), which are known to rely on conversion reactions. The origins of this approach date back to 1994—just three years following LIB commercialization—when Li et al. first demonstrated a fully aqueous LIB with $LiMn_2O_4$ and VO_2(B) as electrodes.[18] Ever since, efforts have been directed towards mimicking LIB chemistry with aqueous electrolytes, including, but not limited to, Li ions as charge carriers. **Table 1-1** summarizes several representative ARBs with respect to their electrode materials, corresponding energy densities, advantages, and disadvantages. Note that this table is not comprehensive, as a detailed overview of existing systems deviates from the

scope of this dissertation. Other review articles provide such comprehensive information.[1a, 1b, 2, 19]

The motivation for LIB-like ARBs is clear. The organic electrolyte in LIBs poses safety issues in abusive environments, which can be resolved by replacing it with an aqueous electrolyte. At the same time, better performance can be expected compared to classical ARBs. Switching out the solvent seems simple enough, but behind this simplicity lies a double-edged sword. From a scientific standpoint, ARBs provide an interesting platform to study different intercalation chemistries due to the innate qualities of water. For example, electrochemical reactions in aqueous environments inherently involve protons that may compete/interact with the intended charge carriers during (de)intercalation. Furthermore, the solvation environment in aqueous solutions is quite different from that of non-aqueous ones on a molecular level, which could affect intercalation kinetics and/or thermodynamics at the electrode/electrolyte interface. Exploring the effect of protons and solvation in comparison to LIB analogues could have significant scientific implications, not only limited to ARBs but also for unexplored battery chemistries.

From a practical viewpoint, however, what makes ARBs interesting ends up being its most crucial weakness: water. In any electrochemical system, the LUMO/HOMO levels of the electrolyte determine its operation limits (**Figure 1-4a**). The gap between the two levels serves as the electrochemical stability window (ESW), outside of which the electrolyte is reduced/oxidized.

For example, if the chemical potential of the anode (e.g. Li metal) were to lie above the LUMO of the electrolyte, the anode would reduce the electrolyte.[20] The beauty of the LIB lies in the fact that such electron transfer between the electrolyte and electrodes can be prevented by creating a passivation layer, commonly known as the solid-electrolyte interphase (SEI) layer. This stabilizes the electrode surface so that only ion transfer occurs, confining electron transfer reactions to the active material.[21] Despite the mysterious nature of the SEI, its essential role in sustaining LIB operation is indisputable.

Unfortunately, a SEI is usually absent in ARBs due to the lack of decomposable organic solvents in general aqueous electrolytes. As a result, the aqueous electrolyte is subject to reduction/oxidation, which manifests in the form of gas (H_2/O_2) evolution; this limits the ESW of ARBs to 1.23 V. There are three problems associated with this. First, a narrow ESW implies less choices for electrode materials (**Figure 1-4b**). Such an intrinsic limit on material selection deprives us of options for optimizing ARB chemistry. Second, low energy density is inevitable. A narrow ESW translates to low operating voltage, which is directly proportional to energy density. In fact, approximately a two-fold deduction in energy density can be expected. Most importantly, gas evolution and electrode redox are in constant competition in the absence of surface-stabilizing SEI layers. Unintended reactions such as H_2/O_2 evolution may degrade the electrode surface and deplete the electrolyte over time, hurting the durability of ARBs for commercial applications.

Depending on the cell packaging, internal gas build-up could cause aqueous cells to burst, which may cause physical damage to their surroundings. However, this is unlikely to develop into total combustion due to the lack of organic solvents that are known to act as fuel for fires.

Overall, ARBs suffer from low energy density and cycle life, stemming from the absence of surface passivation mechanisms like SEI formation. In this respect, competing with LIBs for high energy density applications seems infeasible. Instead, they are more suited for areas where safety is of the utmost importance, such as grid-scale energy storage. Of course, even these applications still demand a certain level of battery performance. Therefore, in order for ARBs to make their way into the battery market, such performance requirements must be met with respect to their target applications while guaranteeing safety. Accordingly, two recently emerging tracks in ARB-related research hold promise.

1.4 Prospective aqueous battery chemistries

The first path is the aqueous analogue of LIBs (ALIBs). While this concept was first demonstrated in 1994, performance improvements were incremental at best. In fact, over the next two decades, most efforts were directed toward finding the right pairing of electrodes that offered reversibility. The anode was the limiting factor; LIB anodes such as graphite or Li metal were unsuitable due to voltage constraints and chemical instability in water, resulting in the need for

new candidates that could intercalate Li ions before the onset of hydrogen evolution. This led to numerous works targeting new and stable anode materials for ALIBs, though their voltage/capacity levels remained stagnant.[22]

A major breakthrough came in 2015, when Suo et al. proposed a simple solution to the ALIB problem—high concentration aqueous electrolytes.[23] This simple approach shifted the paradigm with respect to SEI layers in ARBs. Previously, a crucial setback of aqueous batteries—the lack of a SEI layer—was accepted as an inconvenience by default. However, an extremely high concentration electrolyte, namely "water-in-salt" electrolyte (WiSE), allowed a SEI layer to be generated for the first time in ALIBs. Such a feat is attributed to the difference in solvation environments at the molecular level, whereby the extremely high concentration causes Li ions to coordinate with $TFSI^-$ anions rather than water (**Figure 1-5a**). These newly formed complexes allow $TFSI^-$ anions to be reduced at the anode, forming a LiF-rich SEI layer. The resulting SEI layer, in concert with the low content of water, extends the ESW and suppresses unwanted side reactions in the ALIB.

An extended voltage window offers the obvious benefit of a wider variety of electrode materials from which to choose. This means new electrode material pairings could be employed to heighten the average voltage of ALIBs. Sure enough, ensuing efforts have focused on maximizing the potential of this new class of aqueous electrolytes, pushing the conventional limits of ALIBs by

optimizing electrode pairings and employing additional strategies such as a hydrophobic layer to extend this window even further.[24] Today, the original pioneers of this strategy at the University of Maryland and the Army Research Laboratory in the U.S. spearhead the effort to guide ALIB technology toward practically relevant scales. At their current state, it seems unlikely that even ALIBs as advanced as these will rise to a competitive level for EV or smartphone applications due to cost, but this remains to be seen. Balancing the merits of WiSE with issues like high electrolyte costs and short shelf life owing to changes in concentration and viscosity will likely be the focus of future efforts in this direction.[25]

The second path is the aqueous zinc-ion battery (AZIB), which has only recently begun to gain some attention from the battery community. Previously, aqueous zinc (Zn) batteries were mostly primary in nature, stemming from the irreversibility of Zn metal in alkaline electrolytes. In 1986, Yamamoto *et al.* showed that Zn metal could be plated/stripped reversibly by switching to a more acidic electrolyte such as a zinc sulfate solution.[26] This meant that zinc-based aqueous batteries could become rechargeable. Unfortunately, LIBs were the hype in the battery community, leaving AZIBs with minimal attention.

Fast-forwarding to the 2010s, interest in post-LIB technology re-ignited efforts in alternative rechargeable battery systems like the AZIB. In 2011, a rechargeable AZIB was demonstrated by Xu et al. with a Zn metal ||

$ZnSO_4$ || α-MnO_2 configuration, paving the way for future investigations along this path.[27] AZIBs also operate in a semi-"rocking chair" fashion, the details of which are portrayed in **Figure 1-5b**. Zn metal is usually fixed as the anode, in most part due to its high theoretical capacity, relative aqueous stability, and high HER overpotential.[19c] Plating/stripping reactions at the metal surface are the primary mode of electron transfer. The electrolyte is also formulated as a mildly acidic solution, with $ZnSO_4$ or $Zn(CF_3SO_3)_2$ salts being the most common. With two major components fixed, the challenge lies with the cathode, which must be capable of (de)intercalating Zn^{2+} ions during operation. Thus, most research efforts have focused on the discovery and analysis of cathode materials for AZIBs.

This search has resulted in a number of viable candidates, most of which can be divided into three categories: Mn-oxides,[7b, 28] V-oxides (or sulfides),[7a, 7c, 29] and Prussian blue analogues (unlike LIBs, materials that initially contain the charge carrier ion, Zn^{2+}, rarely exist as viable cathodes).[30] Reported capacity levels are quite high (except Prussian blue analogues), usually ranging from 200–400 mAh g^{-1}, depending on the material. For example, *birnessite*-type MnO_2 exhibits a capacity of ~ 320 mAh g^{-1} with an average voltage of ~ 1.5 V.[7b] Practically speaking, this is good news. However, from a more scientific perspective, this is puzzling. Conventional wisdom dictates that multivalent ions usually exhibit sluggish intercalation/diffusion

kinetics due to their high Coulombic charge.[31] Yet, the high performance levels seem to suggest otherwise. Such a dichotomy warrants further investigation.

From a practical vantage point, the pros and cons of AZIBs are clear. First, AZIBs are expected to be cost-effective in the following respects: i) the production of zinc metal sheets is a well-established industrial process, ii) moisture regulation facilities such as dry rooms are not needed, and iii) Zn is not region-dependent like Li or Co. Second, numerous lab-scale investigations show good performance results in terms of capacity, rate performance, and cycle life. However, AZIBs are subject to a low operation voltage of 1.5 - 2 V (at best), suggesting their inferiority to LIBs in terms of practical energy density. For the record, an AZIB pouch cell (43 stacks) with ~ 150 Wh kg^{-1} has recently been reported,[32] which is an impressive feat within the limits of AZIBs. However, this barely matches up against LIBs from 5-10 years ago. Thus, competing with LIBs for EV applications is unrealistic at this point. Instead, AZIBs should be targeted for applications (e.g. grid-scale energy storage) that play to their strengths—safety and cost—rather than trying to compete in areas where high energy density is a top priority. This direction holds hopeful prospects for AZIB commercialization, but it would still require certain cycling stability and capacity retention levels to be met, which largely depends on material/electrolyte choice and optimization.

1.5 Opportunities for ARBs

Renewable energy sources such as wind and solar energy have become a reality. The energy from these sources can be quite significant, depending on the time and place. However, the intermittent nature of such clean energy sources makes them unpredictable, meaning that their direct integration into the power grid is a difficult task. Instead, newly generated energy can be stored in the interim through large-scale energy storage systems (ESSs). In this way, ESSs can act as buffers to level the imbalance between power supply and demand. The potential market size of ESS technology has attracted many battery manufacturers, exemplified by Tesla's aggressive expansion of the Gigafactory to supply batteries for their EV product line as well as their ESS products (Powerwall, Powerpack).

A good ESS entails two conditions among many: high rate performance and safety. In performing its role as a power grid stabilizer, an ESS must be able to respond to fluctuations in the grid in a real-time manner to maximize its role. This requires high rate capability on the battery's part. In addition, grid-scale ESSs are often installed on a massive scale, consisting of multiple battery modules. Consequently, the smallest fire in an ESS could have devastating consequences on its surroundings or even human lives, not to mention considerable financial loss.

Fortunately, grid-scale ESSs are less sensitive to energy density due

to their stationary nature. This is a huge advantage for ARBs, considering their lower energy densities compared to LIBs. Furthermore, in light of recent fires in LIB-based ESSs, priorities in the ESS market have shifted toward safety as the primary concern. LIBs at such large scales are vulnerable in this respect. In this sense, AZIBs fit the needs of ESS technology, considering the high rate performance levels[33] and inherent safety of aqueous electrolytes. However, AZIBs may have a long way to go before they can be considered for commercialization at the module scale. Not only is a general consensus on cathode material and electrolyte needed for pilot-scale optimization, but commercially viable ways to stabilize the Zn metal surface to ensure reversible plating/stripping are also required for longer cycle life. Furthermore, the possibility of gas evolution could limit the cycling stability of AZIBs by the concomitant buildup of gas pressure with electrolyte depletion. Such problems could be negligible at lab-scale investigations, but strategies for de-gassing and suppression of gas evolution are critical in practical conditions. Therefore, while an ESS-oriented approach holds much promise, obstacles such as material selection, anode stabilization, and gas evolution must be addressed with active research and development.

1.6 A two-pronged approach for AZIBs

Considering the promise of AZIBs for grid-scale applications, maximizing their performance in terms of energy density and cycling stability is essential for

practical viability. This requires a combined effort on two fronts: the cathode and the anode. The ideal cathode would need to satisfy the following conditions: high capacity, high operating voltage, minimal dissolution, fast (de)intercalation kinetics, and high reversibility. The anode, which is often fixed as Zn metal, has different requirements: uniform plating/stripping, minimal dendritic growth, resistance to hydrogen evolution, and aqueous stability. A full cell with an excellent cathode with a limited amount of unstable Zn anode would show sub-optimal performance; the same goes for that with a highly reversible anode paired with a mediocre cathode. It is imperative for both electrodes to retain maximum performance and stability for energy-dense, long-lasting AZIBs. Therefore, a two-pronged approach that addresses both electrodes is a must.

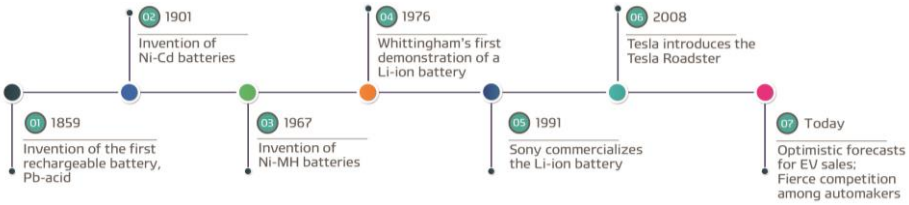

Figure 1-1. Timeline of major developments in rechargeable batteries.

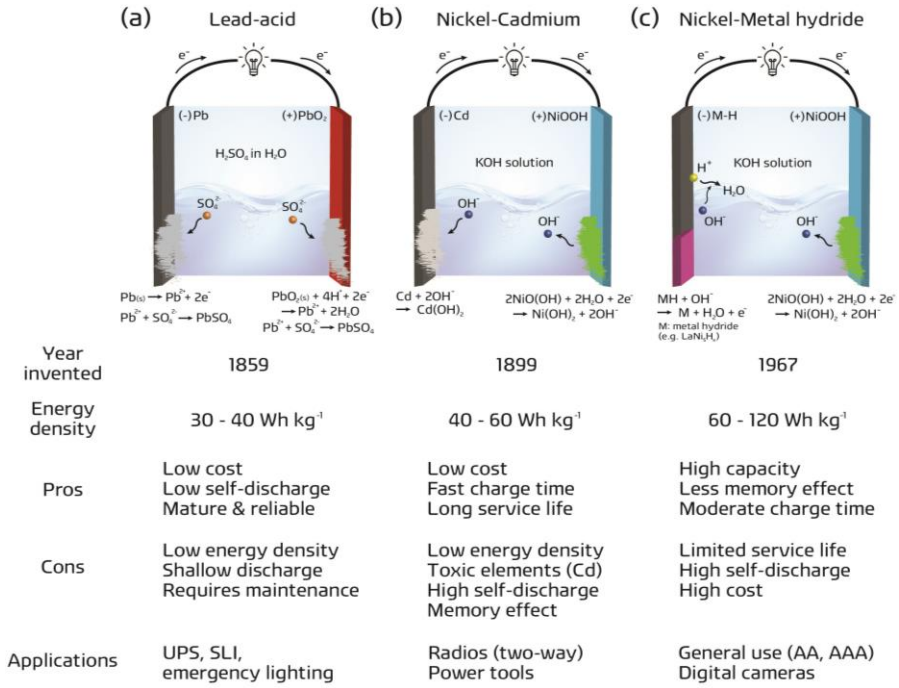

Figure 1-2. Working mechanisms and information for three classical ARBs: (a) Lead-acid, (b) Ni-Cd, and (c) Ni-MH batteries.

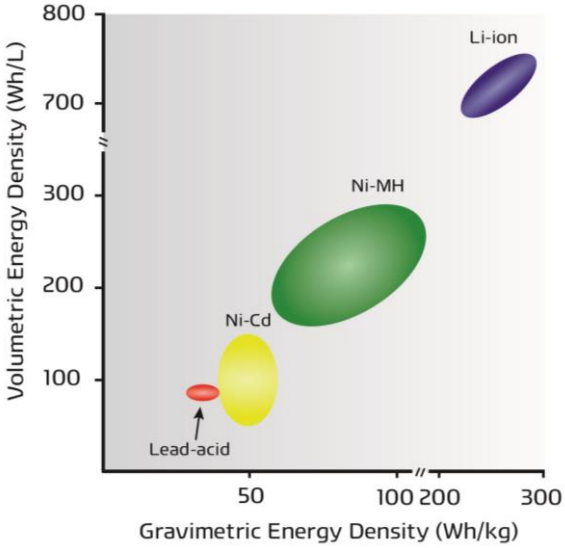

Figure 1-3. Volumetric/gravimetric energy density plots for four types of rechargeable batteries: Lead-acid, Ni-Cd, Ni-MH, and Li-ion batteries.

Category	Type	Cathode	Anode	ED [Wh kg^{-1}]	Pros	Cons	Ref.
Rocking-chair	ALIB	$LiMn_2O_4$	VO_2(B)	75[a]	Reversibility	Generally impossible to use metallic anodes; Suitable anode materials are scarce; Low operating voltage	[18]
		$LiCoO_2$	LiV_3O_8	58			[22a]
		$LiNi_{1/3}Co_{1/3}Mn_{1/3}O_2$	carbon	n/a (3-electrode)			[34]
		$LiFePO_4$	LiV_3O_8	n/a (3-electrode)			[35]
		$LiVPO_4F$	Li metal	480			[24i]
	ASIB	$Na_{0.44}MnO_2$		115			[4a]
		$Na_{0.66}Mn_{0.66}Ti_{0.34}O_2$	$NaTi_2(PO_4)_3$	91			[36]
		$K_{0.27}MnO_2$		56			[37]
	AZIB	V_2O_5	Zn metal	423	Aqueous stability of Zn metal as anode; High capacity	Low operating voltage; Dendritic Zn growth at anode	[38]
		MnO_2		495			[7b]
		ZnHCF		102[b]			[30c]
		$Li_3V_2(PO_4)_3$		156[a]			[32]
Hybrid	Zn-Li	$LiMn_2O_4$	Zn metal	180[b]	Numerous permutations of battery chemistry available	Energy density is limited by the electrolyte concentration	[39]
		$LiFePO_4$		137			[40]
		$LiNi_{1/3}Co_{1/3}Mn_{1/3}O_2$		154[b]			[41]
		$Li_3V_2(PO_4)_3$		179			[10c]
	Zn-Na	$Na_{0.95}MnO_2$	Zn metal	78[b]			[42]
		$Na_3V_2(PO_4)_3$		128			[43]
		$Na_2MnFe(CN)_6$		170[b]			[44]
Dual-ion	Li-Br,Cl	Graphite	Graphite	460[b]	Same material can be used for both electrodes	Energy density is limited by the electrolyte concentration; Anion intercalation requires high voltage	[24k]
	Na-ClO_4^-	$Ni(OH)_2$	$NaTi_2(PO_4)_3$	40			[45]
	Li-OH^-	$LiFePO_4$	Fe_2O_3	75			[46]
Conversion	AZIB	MnO	Zn metal	320[b]	High capacity	Material degradation due to repeated phase transitions	[47]
		Co_3O_4		361			[48]

Table 1-1. Summary of electrode materials, energy density, and (dis)advantages of various types of ARBs.

Most energy density levels are given with respect to the mass of the cathode active material, unless marked otherwise.
[a] Cell-level energy density; [b] (cathode + anode) weight considered.

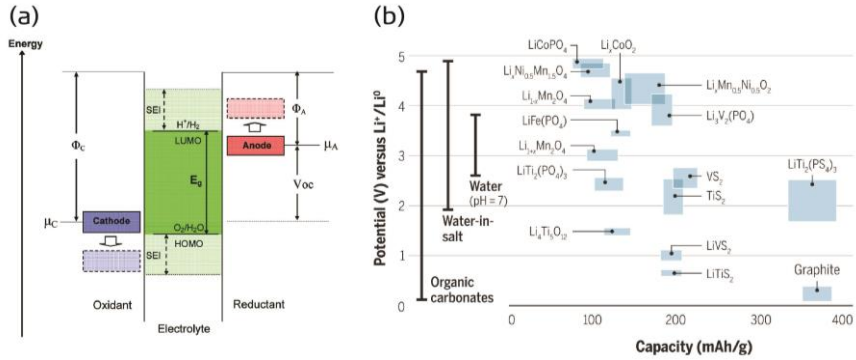

Figure 1-4. (a) Schematic energy diagram of an electrochemical cell. Φ_A and Φ_C denote anode and cathode work functions and μ_A and μ_C denote the electrochemical potentials of the anode and cathode, respectively. Reproduced with permission.[20] Copyright 2010, American Chemical Society. (b) Voltage windows of organic, water-in-salt, and aqueous electrolytes plotted with the chemical potentials of various Li-intercalating materials. Reproduced with permission.[49] Copyright 2015, American Association for the Advancement of Science.

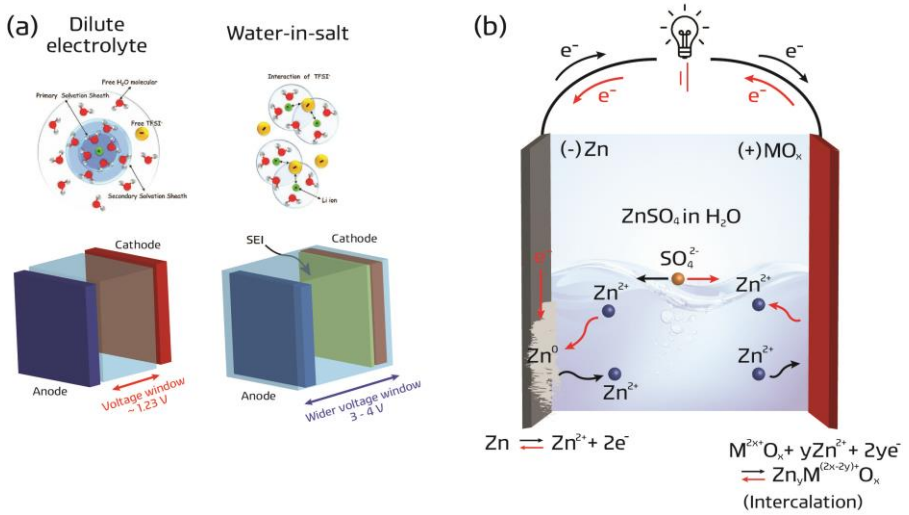

Figure 1-5. (a) Scheme showing the different solvation environments for low and high salt concentrations at a molecular level (top) and their effect on the electrochemical stability windows (bottom). Reprinted with permission (a, top).[23] Copyright 2015 American Association for the Advancement of Science. (b) A general battery configuration and working mechanism for AZIBs.

2. Hydrated Intercalation for High Performance Aqueous Zinc Ion Batteries

2.1 Material selection

The use of Zn^{2+} ions as charge carriers in aqueous media demands a highly selective screening process of suitable cathode materials. First, redox reactions at the cathode must occur before the OER limit, restricting the choice of transition metals. Second, the cathode must be chemically stable in an aqueous environment. Metal dissolution or side reactions could undermine the reversibility of the electrode. Third, the main transition metal should have a wide redox swing in order to fully utilize the bivalent Zn^{2+} ion. Most importantly, the host framework should be able to accommodate the insertion of the charge carriers, as multivalent ions are usually slow in diffusing through the solid-state matrix of electrode materials due to high electrostatic interaction with the matrix,[50] imposing a significant hurdle in realizing decent electrochemical performance. With such highly demanding conditions, it is not an easy task to find a suitable cathode for the AZIB system. Previous investigations have probed the possibility of various organic/inorganic materials such as MnO_2,[27-28, 51] $ZnMn_2O_4$,[28b] $Zn_{0.25}V_2O_5{\cdot}nH_2O$,[7a] LiV_3O_8,[52] VS_2,[29b] $V_2O_5{\cdot}nH_2O$,[7f] $H_2V_3O_8$,[53] $Ca_{0.25}V_2O_5$,[7e] $Na_{0.33}V_2O_5$,[54] p-chloranil,[55] and pyrene-4,5,9,10-tetraone[56] as AZIB cathodes. Nevertheless, considering the dramatically different multivalent nature of the Zn ion compared to Li, there

is much room for improvement in terms of understanding the intercalation chemistry and its correlation with the electrochemical behavior observed in aqueous systems.

In this respect, we hereby present V_6O_{13} not only as a promising cathode material that shows excellent electrochemical performance in an AZIB setting, but also as a model material with which relevant chemical analyses can be performed in order to elucidate the key parameters involved in Zn^{2+} intercalation. V_6O_{13} is attractive for several reasons. First, the wide range of oxidation states of vanadium allows for the possibility of multi-electron reaction upon Zn (de)intercalation. Second, V_6O_{13} is known to be metallic at room temperature,[57] which must be beneficial for high rate battery operation. In fact, due to these innate characteristics of the material, several studies have already dealt with V_6O_{13} in non-aqueous LIBs.[58] Those investigations have shown that V_6O_{13} offers high specific capacities that exceed 300 mAh g^{-1}, implying that the material possesses numerous sites for the storage of intercalant ions; some studies have even shown that V_6O_{13} can accommodate up to 8 Li ions per each chemical formula.[58b, 59] Based on such promising features and previous results, herein, V_6O_{13} is employed as a cathode in an aqueous environment against Zn metal as the anode. Results show extraordinary electrochemical performance, especially in terms of rate capability, In an effort to understand the underlying reaction mechanisms responsible for the observed performance, these results are correlated with a

series of *ex situ* analyses along with *in situ* synchrotron X-ray diffraction (XRD) results and density functional theory (DFT) calculations. In particular, we focus on the intercalation behavior of Zn^{2+} ions within the lattice framework of V_6O_{13}. Interestingly, a series of analyses reveals "hydrated intercalation" as the origin of the peculiar electrochemical activity and stability of V_6O_{13} and illuminates this intercalation mechanism as a key factor in improving the performance of AZIB systems.

2.2 Results and discussion

2.2.1 *Material characterization*

The V_6O_{13} cathode material was first characterized with XRD, scanning electron microscopy (SEM), and transmission electron microscopy (TEM). As indicated by the XRD data in **Figure 2-1a**, the peaks are consistent with the monoclinic crystalline phase of V_6O_{13} (ICSD #16779) with no signs of impurity phases. The crystal structure of V_6O_{13} is shown in **Figure 2-1b**, projected down the *b* axis. This structure consists of alternating single and double layers of distorted VO_6 octahedra. In both layers, the octahedra propagate down the *b* axis in a zigzag manner. The SEM image in **Figure 2-2a** shows a magnified image of a V_6O_{13} particle, the morphology of which indicates an agglomeration of platelets that size up to ~ 10 μm. On a sub-micrometer scale, the TEM image (**Figure 2-2b**) shows the platelet-like morphology of this material. Further magnification shows that this material possesses high crystallinity with distinct

lattice fringes corresponding to the (110) plane (inset of **Figure 2-2c**). In addition, energy dispersive X-ray spectroscopy (EDS) mapping results (**Figure 2-2d**) with respect to vanadium and oxygen show that these elements are abundant and well-distributed throughout the particle.

2.2.2 *Electrochemistry*

The electrochemical performance of V_6O_{13} was evaluated with various protocols. **Figure 2-3a** shows the cyclic voltammetry profiles of V_6O_{13} measured over 10 cycles at a scan rate of 0.1 mV s^{-1}. The profiles overlap well for the cycles with negligible peak shifts. A pair of main reduction/oxidation peaks was observed at 0.5/0.6 V, along with other peaks with less intensity at higher potentials, indicating the reversible electrochemical activity of V_6O_{13} in the given potential range. Galvanostatic charge/discharge profiles for 10 cycles tested at 200 mA g^{-1} are displayed in **Figure 2-3b**. During these cycles, the cell delivers a specific capacity of ~ 360 mAh g^{-1}, and the galvanostatic profile remains overlapped during the cycling period. In order to evaluate the cyclability of this material at a low rate, a cell was cycled at 400 mA g^{-1} for 200 cycles (**Figure 2-3c**). This resulted in some capacity fading with retention of ~ 80%, an occurrence often observed in aqueous batteries tested at low current densities.

Cycle performance was also evaluated at 4.0 A g^{-1}. As is evident in **Figure 2-4a**, the cell showed stable performance for over 2000 cycles, during which a capacity of ~ 230 mAh g^{-1} was extracted. Moreover, the same cell

shows minimal capacity fading, retaining 92% after 2000 cycles with respect to the maximum capacity. Note that the initial rise in capacity is most likely due to the gradual activation of the active material. This phenomenon has been observed with other aqueous battery materials[7d, 7f, 53] and requires further analysis for an in-depth understanding. Finally, the V_6O_{13} cathode was subjected to rigorous rate capability testing protocols to assess its ability to (de)intercalate Zn ions at low to extremely high current densities. As displayed in **Figure 2-4b**, the material is able to endure current densities of up to 24.0 A g^{-1}. In fact, it is worth noting that a capacity of 145 mAh g^{-1} was attained at this level, which, to the best of our knowledge, is one of the highest reported capacity levels thus far at such a high current density.[33] Upon returning to 4.0 A g^{-1}, the cell rebounds to its previous capacity at this rate with no observable loss.

2.2.3 *Structural and chemical analysis*

In order to observe morphological changes upon battery operation, SEM and TEM analyses were conducted. **Figure 2-5** shows *ex situ* SEM and TEM images of V_6O_{13} after full discharge and charge, respectively. From the SEM images, it is clear that electrochemical cycling does not have a significant impact on the original morphology of the V_6O_{13} material. The agglomeration of platelets originally observed in the pristine material appears to be preserved. TEM images also confirm this tendency, in which the platelet-like morphology of the V_6O_{13} material was observed.

Having confirmed the morphological stability of the cathode materials, X-ray absorption spectroscopy (XAS) experiments with a synchrotron light source were conducted to investigate the oxidation state changes of the material at its bulk. **Figures 2-6a, b** show XAS results for four samples: V_6O_{13} pristine electrode (black), discharged electrode (red), charged electrode (blue), and V_2O_5 reference powder (purple). The results shown here pertain to the X-ray absorption near-edge structure (XANES) region of the XAS data set for the V K-edge energy window, as highlighted with the pink box in **Figure 2-6a**. From these results, it is clear that the pristine and charged samples are almost identical in their absorption edge energy levels, which indicates that the oxidation states of V for both samples are nearly the same. On the other hand, the absorption edge of the discharged sample (red) is clearly shifted toward a lower energy level, implying a lower oxidation state of V compared to the pristine and charged samples. Therefore, these XANES results allow us to conclude that reversible redox flip of V occurs at the bulk scale, in a consistent fashion with the surface as shown by the *ex situ* X-ray photoelectron spectroscopy (XPS) results in **Figure 2-6c-e**. In addition, the manner in which the electrons are accepted by the material can be explained with the changes in the pre-edge peak intensities as marked with the green ellipse in **Figure 2-6a**. Here, distinct pre-edge peaks can be observed for the three samples. Previous investigations[60] with XAS studies of various vanadium oxides show that the presence of such pre-edge peaks indicates $s \rightarrow d$ transitions that are usually forbidden according

to dipole selection rules. However, it has been shown that deviation from octahedral symmetry causes V 3d states to mix with O 2p states, allowing the *s* → *d* transition at a lower energy prior to the main absorption edge.[60-61] As V_6O_{13} comprises distorted VO_6 octahedra throughout its crystal structure, the occurrence of such pre-edge peaks is feasible. More importantly, a drop in the pre-edge peak intensity for the discharged sample points to a change in the electronic state of the material. As Zn intercalates into V_6O_{13}, the accompanying electrons progressively fill the hybridized 3d–2p states, resulting in less X-ray absorption intensity at the pre-edge region.

On a related note, several electrochemical and chemical analyses were conducted in order to correlate the redox swing of V with Zn (de)intercalation (**Figure 2-7**). **Figures 2-7a-b** show EDS results of discharged and charged samples, respectively. Noting that each scan was limited to 100,000 counts, one can observe that the discharged sample shows significantly higher levels of Zn than the charged sample, supporting the claim that Zn is intercalated into V_6O_{13} upon discharge. The same trend is translated to the bulk scale, which has been confirmed by XAS measurements of the (dis)charged electrodes for Zn K-edge (**Figure 2-7c**). At the absorption edge for Zn K-edge, the discharged sample (Zn intercalated) shows a distinctly higher absorption edge compared to the charged sample. In fact, the XAS spectra for the charged sample can barely be distinguished from measurement noise peaks, further implying the relative absence of Zn at the fully charged state. Furthermore, V_6O_{13} has been shown to

be susceptible to proton intercalation. In order to discount the possibility of proton intercalation contributing to the electrochemical capacity in this case, 3-electrode beaker cell configurations were adopted with an aqueous 0.1 M H_2SO_4 electrolyte. **Figure 2-8** shows the results of this experiment, where an initial discharge capacity of ~ 110 mAh g^{-1} was observed at 100 mA g^{-1}. In the following cycles, this drops severely to negligible capacity levels, indicating the irreversibility of proton (de)intercalation in this material. On the other hand, the electrochemical results in **Figure 2-3 and 2-4** show high Coulombic efficiency levels, implying that proton intercalation has a negligible impact on electrochemical performance. Therefore, based on the EDS and XAS measurements coupled with the 3-electrode experiments, Zn (de)intercalation is mainly responsible for the changes that occur in V_6O_{13} during battery operation.

The structural changes upon Zn (de)intercalation were examined with *in situ* synchrotron XRD experiments performed in a coin cell setting. Among approximately 200 images that were collected for one discharge/charge cycle, a total of 20 images that correspond to the red and blue markers on the voltage–time profile (**Figure 2-9**) were selected and plotted with respect to 2θ values. Note that the 2θ values have been recalculated for Cu K_α wavelength for easy comparison with existing literature. Overall, one can distinguish significant peak shifts on several fronts, represented by the (110), (−401), (−311), and (020) planes that have been magnified in **Figure 2-9c-e**. The general trend in peak

shifts is consistent among these planes, where discharge is accompanied by a gradual leftward shift (increase in d-spacing) and charge by a rightward one (decrease in d-spacing), albeit a difference in the degree of shifting depending on the plane. Such a continuous and reversible nature of the peak shifts hints at single phase reactions during Zn intercalation, reflecting the solid solution-like intercalation behavior of V_6O_{13}; it accommodates the ions *via* reversible expansion and contraction on several fronts without forming phase boundaries, although minor peaks are newly formed at low state-of-charge (*ex situ* XRD, **Figure 2-10**). Thus, with the exception of a minor secondary phase at high levels of Zn intercalation, a single-phase reaction appears dominant throughout most of the (de)intercalation process.

In terms of electrochemical performance and stability, this solid solution-like intercalation is preferred. Although it is a well-established fact that aqueous media have considerably higher ionic conductivity than organic solutions by several orders of magnitude, the active materials comprising the electrodes should keep up with the kinetics in the electrolyte to boost the overall cell kinetics. In the case of two-phase reactions, the formation and progression of phase boundaries would impose a higher energy penalty, leading to inferior rate performance.[62] In contrast, single-phase reactions allow the material to uptake/extract carrier ions while largely maintaining its original crystal framework. Without the need for an additional phase formation step, such behavior results in fast reaction kinetics in the electrode.

The single-phase reaction mechanism appears to be an inherent trait of V_6O_{13}.[63] However, we believe that the extent to which Zn ions can be intercalated while retaining this reaction mechanism is intricately linked with hydrated intercalation. This particular intercalation mechanism involves the co-intercalation of water molecules with the carrier ion into the crystal structure of a host material. Consequently, hydrated intercalation has been shown to mitigate the de-solvation energy penalty at the electrode–electrolyte interface.[6, 64] In typical rechargeable batteries based on organic electrolytes, carrier ions are de-solvated at the interface at the expense of overpotential. Evidently, this de-solvation energy penalty is higher for multivalent ions due to the higher electrostatic interaction between the carrier ion and solvent molecules. Hydrated interaction circumvents this energy loss, leading to more facile carrier ion diffusion at the interface. Furthermore, hydrated intercalation can even cause a change in the original structure by forming new crystal planes consisting of water molecules.[6, 64f, 64g] In fact, it was discovered that this structural rearrangement stemming from water co-intercalation dramatically enhanced the electrochemical performance of the material in question. Such influence of water indicates that, under the right conditions, water co-intercalation can facilitate the intercalation of multivalent ions at the interface as well as in the host framework. These ions have strong charge densities that can impede carrier ion diffusion *via* high electrostatic interaction with the host matrix, quite possibly distorting the original crystal structure of the material.

With the help of co-intercalated water molecules, however, these effects can be mitigated by shielding the electrostatic interactions between the charge carrier and the host matrix. Under the conditions of low de-solvation energy and electrostatic shielding,[65] it is postulated that hydrated intercalation significantly extends the degree to which Zn ions are intercalated into the material with minimal distortion in a solid solution-type fashion, thus improving electrochemical activity. To this end, we focus on comparing the cases for non-aqueous, partially aqueous, and fully aqueous electrolytes with experiments and DFT calculations.

2.2.4 *Hydrated intercalation and its effect on performance*

The presence and effect of water were analyzed with various chemical and electrochemical characterizations. First, the V_6O_{13} cathode was tested in different electrolyte compositions: pure anhydrous acetonitrile (AN), 0.1 mol% H_2O in AN, 0.2 mol% H_2O in AN, 0.4 mol% H_2O in AN, 1.0 mol% H_2O in AN, 3.0 mol% H_2O in AN, and pure H_2O with 1 M $Zn(CF_3SO_3)_2$ (**Figure 2-11a**). Evidently, an increase in capacity can be observed in proportion to increasing water content in the electrolyte. *Ex situ* XAS V K-edge measurements verify this trend, as fully charged and discharged samples for pure AN, 0.2 mol% H_2O in AN, and pure H_2O show increasing shifts in energy (**Figure 2-11b**). Moreover, *in situ* XRD experiments in **Figure 2-11c and 2-11d** for pure AN and 0.2 mol% H_2O in AN, respectively, show increased degrees of peak shifts for cells with higher levels of water in the electrolyte. From these results, it is

clear that even trace amounts of water have a significant impact on the extent of Zn intercalation upon discharge. Similar to the aqueous case (**Figure 2-9**), both XRD profiles indicate a single-phase intercalation pathway, but the low extent of the main peak shift indicates less Zn intercalation when less water is present. This point is further elaborated upon in the following sections. Although it is difficult to precisely quantify the amount of water that co-intercalates into the material, *ex situ* thermogravimetry analyses (TGA) in **Figure 2-12a** confirm the relatively high presence of water in the crystal lattice, as shown by the distinct inflection point at approximately 150°C. The rather steep weight loss is a trademark of hydrated metal oxides such as $V_3O_7 \cdot H_2O$[66] and layered double hydroxides,[8] where structural water accounts for the sudden weight loss above 100°C. Furthermore, *ex situ* Fourier transform infrared spectroscopy (FT-IR) results in **Figure 2-12b** for the discharged sample in 1 M $Zn(CF_3SO_3)_2$ in pure water show a heightened presence of water compared to the pristine and charged sample at a wavenumber of 3500 cm^{-1}. The slight rise in absorbance for the charged sample may be due to some remaining co-intercalated water molecules. Nevertheless, based on the combined trends in the electrochemical capacity levels, degree of energy shift in the XANES region, shifts of the main peak in the *in situ* XRD profiles, TGA, and FT-IR results, hydrated intercalation is indeed responsible for enhanced Zn (de)intercalation.

2.2.5 *DFT calculations*

Based on these experimental findings, we employed density functional theory calculations to investigate the "water effect" in terms of ion diffusion and structural stability by comparing the cases of Zn intercalation with (1.75 mol H_2O / Zn) and without water. In constructing a model for DFT calculations, water was inserted into the V_6O_{13} framework along with Zn to simulate the experimental conditions of discharge (Zn insertion with water co-intercalation). As discussed in detail in the Experimental Section, Zn was successively inserted into the most energetically favorable sites in the V_6O_{13} framework. Since our model consists of two unit cells (corresponding to 24 vanadium atoms and 52 oxygen atoms), up to 8 Zn atoms were inserted when fully discharged for the case without any water (**Figure 2-13a-d**). The optimized intercalation sites for Zn coincide with the previous Li ion storage cases for V_6O_{13}.[57] For comparison, 3, 7, 11, and 14 water molecules were inserted into the V_6O_{13} framework for each two-Zn insertion step (**Figure 2-13e–h**), respectively, to model the H_2O/Zn ratio of 1.75 obtained from TGA results. For reference, the pristine V_6O_{13} unit cell is displayed in **Figure 2-13i**.

A difference in the coordination environments of Zn depending on the presence of water can be observed, as shown in the optimized geometries of Zn-intercalated V_6O_{13} for both cases (**Figures 2-14a, b**). These visual representations show that the presence of water is the key to determining the

coordination sites of Zn, where octahedral coordination is preferred when water is present and under-coordinated when not. This difference in coordination sites has a pronounced effect on the original crystal framework such that the former case appears to cause minimal distortion of the host lattice. The simulated XRD profiles of V_6O_{13} with various Zn and water contents are displayed in **Figure 2-15a**. For the aqueous case (left), a gradual leftward shift of the main peak around 25° can be seen (up to 2 Zn insertion). Accordingly, a distinct rise in the unit cell volume (**Figure 2-15b**) for the aqueous case can be observed, indicating increased lattice parameters. In the anhydrous case (right), a slight leftward shift was also observed in the simulated pattern (0.5 Zn insertion), albeit with a negligible change in unit cell volume. An interesting point of difference, however, lies in the early onset of new phases beyond 0.5 Zn insertion for the anhydrous case, indicating the distorting nature of Zn intercalation without assistance from water. In fact, although the changes in cell parameters and volume are larger in the hydrated case, actual atomic displacements in fractional coordinates (**Figure 2-15c**) change to a greater extent for the anhydrous case. These structural signatures can be related with the electrochemical results for non-aqueous cells (**Figure 2-11a**, profile in black) in which significantly lower capacity levels were observed. In the absence of water, fewer Zn can intercalate into the host material because excessive intercalation may result in a largely distorted different crystal phase. Indeed, this seems to be the case, where previous reports show that V_6O_{13} can

intercalate up to only 0.4 Zn (40–50 mAh g^{-1} in capacity) in a similar non-aqueous electrolyte formulation, despite the use of a low current electrochemical titration protocol.[63] On the other hand, hydrated intercalation permits the same material to accept more Zn ions upon discharge to a higher limit before new phases start to form in the simulated XRD profiles. This is corroborated by the *in situ* XRD results for the three cases of pure AN, 0.2 mol% H_2O in AN, and pure H_2O (**Figures 2-11c-d**, **2-9** respectively), where all cases show single-phase intercalation, but the amount of water in the electrolyte determines the degree to which the material can accommodate Zn ions. Thus, water co-intercalation facilitates Zn insertion by minimizing structural distortion, resulting in higher capacity.

Voltage calculations were performed in order to elucidate the relative energetic stability of the cathode material upon discharge depending on the presence of water (**Figure 2-15d**). The potential profile in the case of water co-intercalation overlaps with experimental data reasonably well with a continuous decrease of the potential upon additional Zn insertion. The latter decrease in voltage, which is generally observed in most battery anode materials, is a result of Zn ions experiencing repulsion between those intercalated at an early state of discharge and at a later one. On the other hand, the anhydrous case shows a higher potential overall along with an increase in potential after the insertion of 1 Zn ion. The latter increase in the calculated voltages at later stages of

discharge in the absence of water is unusual and may be due to a (potentially irreversible local) structural change of the host material to optimally accommodate incoming Zn ions. This interpretation can be linked to the observed electrochemical performance of V_6O_{13} in a non-aqueous electrolyte (**Figure 2-11a**, profile in black), where less than 1 Zn is reversibly intercalated (in terms of capacity). Therefore, based on the optimized geometry, their corresponding XRD simulation patterns, and voltage calculations for both cases, the DFT calculation results imply the relatively stable nature of Zn-intercalated V_6O_{13} framework in aqueous environments due to water molecules acting as coordinating ligands to maintain the original structural motifs.

Lastly, in order to observe the effect of water on Zn ion diffusion kinetics within the solid-state matrix, the kinetic energy barrier for Zn diffusion was evaluated for both cases (**Figure 2-16**). In doing so, nudged elastic band (NEB) calculations were performed along the possible Zn ion diffusion paths for the same distance. An intercalation state of $Zn_{1.0}V_6O_{13}$ was assumed for this estimation. As expected, among numerous possible diffusion paths, those along the *b* axis showed the lowest kinetic barrier for both cases, consistent with previous works regarding Li ion batteries.[57, 67] The projected diffusion paths for Zn ions can be seen in **Figure 2-16a, b**. In the case of water co-intercalation (**Figure 2-16a**), Zn prefers to travel along a zig-zag route along the *b* axis from one octahedral site to the adjacent octahedral site, with water molecules rearranging to minimize electrostatic repulsion from the lattice oxygen atoms.

In the anhydrous case (**Figure 2-16b**), Zn ion diffusion takes a more straightforward path, though it tends to skew toward one side at the end. In both cases, it is useful to examine the cross-sectional area through which Zn travels. As shown in **Figure 2-16c**, it turns out that the cross-sectional area (formed by V and O) for the anhydrous case is significantly smaller than that with water. This can be understood in relation to **Figure 2-15b**, where the aqueous case shows significantly larger unit cell volumes upon Zn insertion than the anhydrous case. As Zn diffuses from one site to a symmetrically identical site, co-intercalated water has the effect of expanding the diffusion channel so that the Zn ion traverses more freely. On a related note, we have also calculated the charge difference between the two cases. A simple integration of the projected density of states (PDOS) (**Figure 2-17**) indicates that Zn, when coordinated with water, has a lower charge than Zn without water (**Table 2-1**). We anticipate that this difference originates from the oxygen atoms in H_2O, whereby the donation of electrons from O to Zn lowers its charge. With a lower charge, Zn ions are able to withstand the electrostatic interaction with the host lattice, resulting in a relatively higher degree of freedom for movement compared to their anhydrous counterpart. With this in mind, an examination of the kinetic barrier for Zn ion diffusion (**Figure 2-16d**) for both cases gives a more definitive comparison of the relative ease with which the carrier ion can diffuse. Notably, a significantly lower energy barrier of 0.87 eV (~10^{-17} cm^2 s^{-1} as calculated by transition state theory) in the presence of water is calculated,

whereas the anhydrous case entails a barrier of 2.85 eV. Therefore, hydrated intercalation of Zn permits a low kinetic energy barrier by expanding the cross-sectional area along the diffusion path and lowering the charge of Zn, the combined effects of which may account for the high-rate performance.

2.2.6 *Experimental*

Synthesis: V_6O_{13} pristine powder was synthesized from a hydrothermal procedure. For the precursor materials, ammonium metavanadate (1.62 g) and oxalic acid dihydrate (2.01 g) were added to 60 mL DI water. Once this solution was thoroughly mixed, it was transferred to a Teflon-lined parr bomb (100 mL capacity) that was sealed in an autoclave. The reaction protocol was set to a temperature of 180 °C for 44 h. After the hydrothermal process was complete, the resulting materials were recovered via washing and filtering with DI water. Then, the materials were set to dry in a convection oven at 70 °C overnight. The resulting powder was then annealed in an argon atmosphere in a tube furnace at 300 °C for 12 h with a ramping rate of 5 °C min^{-1}. All precursor reagents were purchased from Sigma Aldrich and used without additional purification.

Characterization: X-ray diffraction measurements were conducted to characterize the pristine powder using an X-ray diffractometer (Smartlab, Rigaku, 40 kV, 200 mA) with Cu K_α radiation (λ=1.5406 Å). The scan rate and interval were set at 5° min^{-1} and 0.02°, respectively. *Ex situ* XAS experiments were conducted under transmission mode at the 7D (**Figure 2-6a, b**) and 1D

(**Figure 2-11b, Figure 2-7c**) beamlines at Pohang Accelerator Laboratory (PAL). After cycling five times, the coin cells were dissembled to recover the electrodes, which were washed with appropriate solvents and freeze-dried overnight. The obtained spectra were processed by using ATHENA in the IFFEFIT package.[68] XPS measurements were performed with a Sigma Probe (ThermoFisher Scientific, UK) equipped with an Al source. The lattice water content was quantitatively analyzed with a thermogravimetry analyzer (TGA Q500, TA Instruments). SEM images were obtained from a FE-SEM 7800F Prime microscope (JEOL Ltd., Japan). High-resolution TEM images and EDS analyses were also performed with a Cs-corrected TEM microscope (JEM-ARM200F, JEOL Ltd., Japan). FT-IR spectra were obtained from a Nicolet 6700 FT-IR spectrophotometer (Thermo Scientific, USA). Samples for FT-IR analysis were carefully rinsed with appropriate solvents and freeze-dried overnight. The resulting powders were collected and kept in a convection oven for 2 h at 70 °C before measurements. These powders were pelleted with potassium bromide (KBr) with careful attention to consistent pellet thickness and sample amount. The measurements were conducted under vacuum to minimize the peaks from atmospheric moisture.

In situ XRD Measurements: *In situ* XRD measurements were conducted at the 1D beamline (λ = 0.999873 Å) at PAL. A MAR345 image plate detector was used under transmission mode. The typical duration for collecting an individual diffraction pattern was 150 s. The obtained ring

patterns were converted to 2θ data with the *Dawn* program.[69] The storage ring energy was set at 3 GeV under a top-up mode with a maximum current of 350 mA. A modified coin cell sealed with imide tape at both ends was used to cycle the cell at 0.3C using a galvanostatic charge/discharge protocol with a Biologic (SP-50) instrument.

Electrochemistry: 2-electrode measurements were employed for battery testing protocols. For cathode fabrication, the active material powder, conductive carbon (Super-P), and binder (poly-vinylidenefluoride, Kynar) were mixed homogeneously in *N*-methyl 2-pyrolidone (NMP) to form a slurry with a weight ratio of 7:2:1. The slurry was then cast onto a sheet of pyrolytic graphite film (MTI Korea) with an areal active mass loading of ~ 1.0–1.5 mg cm^{-2}. The coated electrodes were dried in a vacuum oven set at 70 °C overnight. In assembling the coin cells (SUS316L, Wellcos, Korea), 3 M $Zn(CF_3SO_3)_2$ aqueous solution was used as the aqueous electrolyte and 1 M $Zn(CF_3SO_3)_2$ in acetonitrile (anhydrous) as the non-aqueous electrolyte. Electrolytes with varying water content were carefully formulated in an argon-filled glove box with H_2O levels less than 2.0 ppm using anhydrous acetonitrile (Sigma Aldrich). The corresponding coin cells were also fabricated in the glove box. Zn metal foil (Alfa Aesar) was employed as the anode and cellulose filter paper (Whatman) was used as the separator. The assembled coin cells were tested with a WBCS3000L battery cycler (Wonatech, Korea). The active material weight alone was used to calculate the current densities and specific capacities.

3-electrode beaker cell measurements were conducted with a Biologic (SP-50) instrument. The working, counter, and reference electrodes were V_6O_{13}, graphitic film, and Ag/AgCl, respectively.

DFT calculations: To perform periodic DFT calculations, the Vienna *ab initio* simulation package (VASP) was utilized.[70] The generalized gradient approximation (GGA) within Perdew–Burke–Ernzerhof exchange correlation functional and projector-augmented-wave method were utilized with Grimme's D3 dispersion correction (zero damping).[71] U correction parameter was set for vanadium as 3.1 eV.[72] For all calculations, the Monkhorst–Pack k-point mesh was utilized with a grid spacing of <0.03 $Å^{-1}$.[73] Kinetic barriers for Zn diffusion were calculated with the nudged elastic band method using the same GGA–PBE functional.[74] The energy cutoff for the plane-wave basis set was set as 400 eV except for screening single point calculations which was set as 200 eV. Since Zn changes its oxidation state by 2 before and after the intercalation, the chemical potential difference is divided by two for each Zn to calculate the voltage.[75] With the water inclusion condition, the chemical potential of water has to be considered. We have calculated the energy of the water from TIP4P geometry with 10 water molecules where the energy of the water molecules are nearly converged.[76]

$$\mathrm{V} = -\frac{E(Zn_xV_6O_{13}) - E(V_6O_{13}) - xE(Zn) - yE(H_2O)}{2x}$$

To describe the discharge process, a total of 8 Zn atoms were inserted

in a stepwise manner (two Zn per step) into the V_6O_{13} supercell (stoichiometry of $Zn_2V_6O_{13}$). The V_6O_{13} structure was adopted from the Materials Project (mp-19457). For all calculations, two unit cells of V_6O_{13} were stacked along *b* axis to have 24 vanadium atoms and 52 oxygen atoms in the supercell. To find the most stable positions of Zn for each step, the following three steps were taken hierarchically: Ewald summation, single point DFT calculation, and full DFT geometry optimization. First, a 3D network of 6720 grid points was considered inside of V_6O_{13} framework with grid spacing of 0.5 A. Potentially stable Zn positions were evaluated through Ewald summation and single point DFT calculation with a cutoff energy of 200 eV.[77] Then, the full DFT optimization for the latter subset of candidates was performed to finalize the search for stable sites. As a result, 52 stable positions were identified. These positions could be categorized into 6 different sites where 5 sites correspond to the sites that were previously identified with Li atoms.[57, 67] For each successive two-Zn insertion, all 2 combinations of 52 different Zn positions were considered and evaluated with the same three-step screening process described above. Favorable configurations of water for water co-intercalated cases were determined similarly. Since the water molecule was most stable when conjugated to Zn, another grid network with 0.5 Å spacing was considered around Zn with a radius of 2.5 Å for water co-intercalation conditions. For each such radial position, 48 different water rotation possibilities were considered, corresponding to 48,000 different configurations total. Again, the three-step

screening process was utilized to identify the most stable structure of water. At the end of the screening process for both conditions (with and without water), the most stable configuration was used for subsequent two-Zn insertion steps. To match the experimental H_2O/Zn ratio of 1.75 obtained from TGA results, 3, 7, 11, and 14 water molecules were inserted together with Zn for each two-insertion step.

2.3 Summary

In conclusion, through various analytical techniques and electrochemical evaluations, we have shown the potential of V_6O_{13} as a viable cathode material for AZIBs. V_6O_{13} achieves a high specific capacity of 230 mAh g^{-1} at 4.0 A g^{-1} with stable cycle performance (92% retention after 2,000 cycles). In particular, the Zn || $Zn(CF_3SO_3)_2$ in water || V_6O_{13} cell exhibits extraordinary rate capability, evidenced by a capacity of 145 mAh g^{-1} at 24.0 A g^{-1}. Post-mortem analyses including *ex situ* SEM, TEM, XPS, XAS, EDS, FT-IR, along with *in situ* XRD reveal that the electrochemical performance of V_6O_{13} is associated with hydrated intercalation and a single-phase reaction mechanism. DFT calculations coherently verify that co-intercalating water molecules can play a vital role in enhancing the electrochemical performance by facilitating Zn ion diffusion *via* shielding electrostatic interactions with the host matrix and enlarging the channel dimensions. This study suggests that hydrated intercalation is key to understanding the structural dynamics of electrode

materials in aqueous electrolytes and ultimately developing high performance aqueous battery systems in the near future.[78]

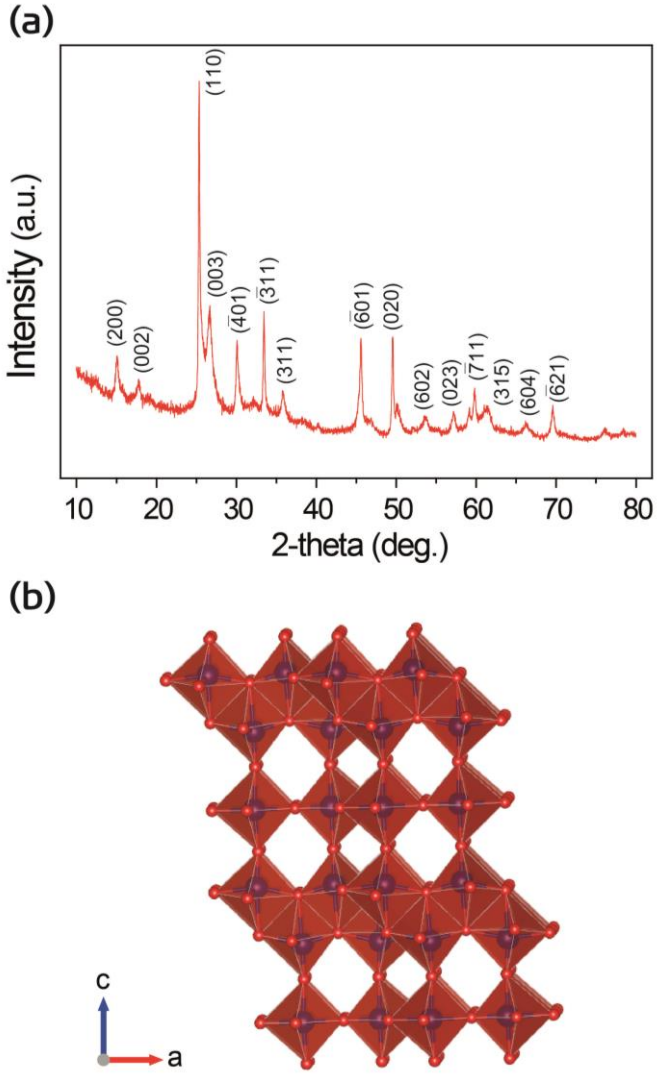

Figure 2-1. (a) XRD profile for as-synthesized V_6O_{13} powder. (b) Crystal structure of V_6O_{13} along [010] direction.

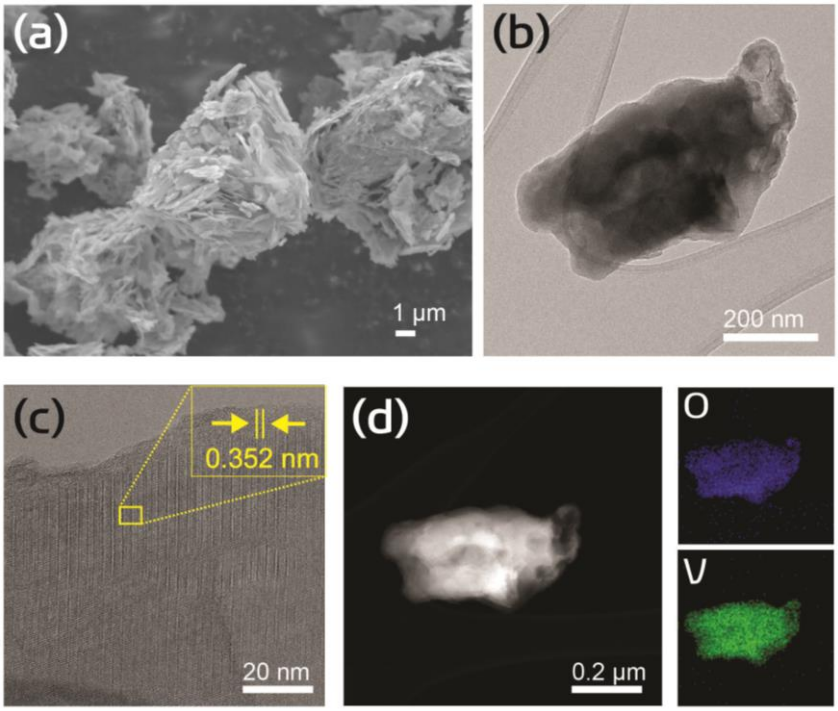

Figure 2-2. (a) SEM and (b) TEM image of as-synthesized V_6O_{13} powder. (c) Magnified TEM image (inset: lattice fringe for (110) plane) with a lattice fringe of d_{110} = 0.352 nm. (d) STEM image of V_6O_{13} particle (left) and EDS mapping results with respect to V and O (right)

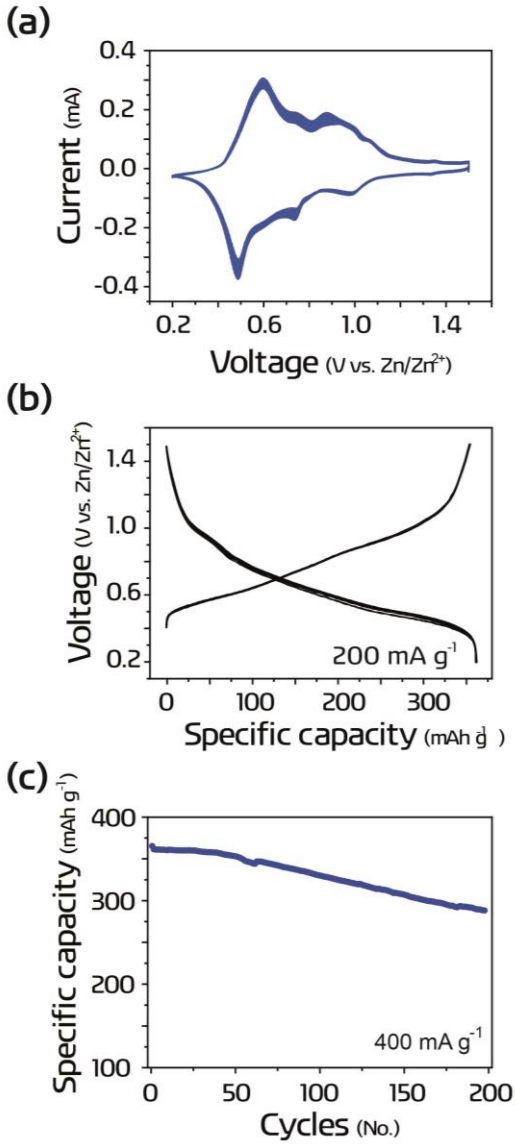

Figure 2-3. Electrochemical performance results for Zn/V_6O_{13} full cells. (a) Cyclic voltammetry profiles (10 cycles at 0.1 mV s^{-1}). (b) Galvanostatic voltage-capacity profiles for 10 cycles (0.2 A g^{-1}). (c) Galvanostatic cycling results of V_6O_{13} at 0.4 A g^{-1}.

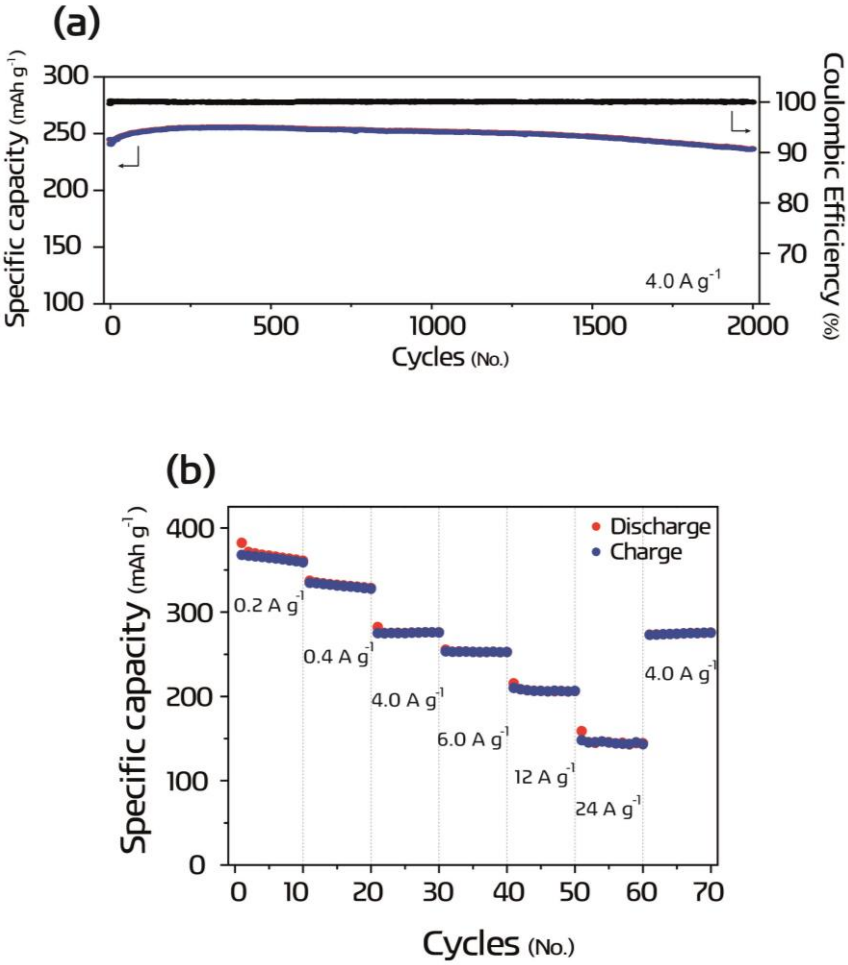

Figure 2-4. (a) Long-term galvanostatic cycling results for 2000 cycles (4.0 A g^{-1}). (b) Rate capability test results for V_6O_{13} at 0.2, 0.4, 4.0, 6.0, 12.0, 24.0, and 4.0 A g^{-1}, respectively.

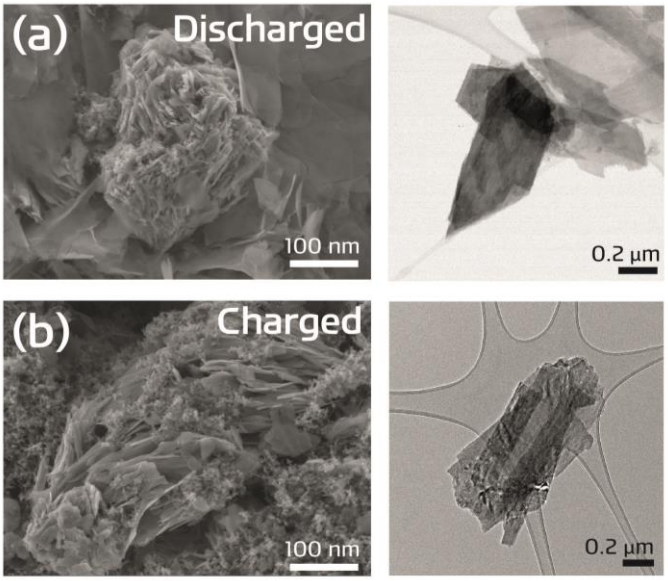

Figure 2-5. Ex situ SEM images of (a) discharged and (b) charged electrode material after five cycles each.

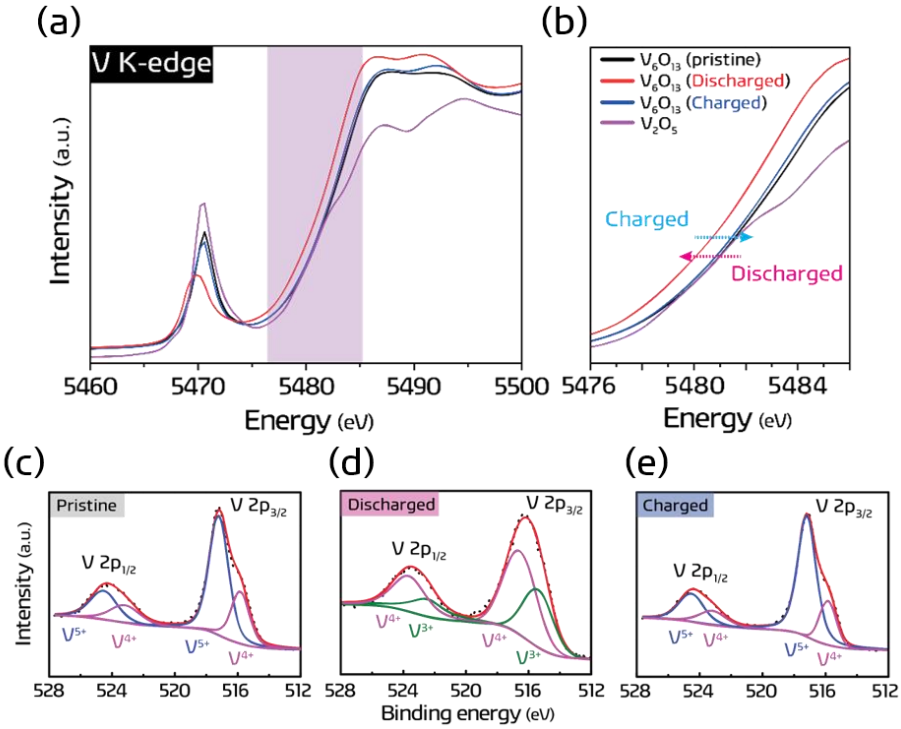

Figure 2-6. (a) Synchrotron XAS results (V K-edge, transmission mode) for pristine and cycled V_6O_{13} electrodes (after 5 cycles). Dashed ellipse in green indicates pre-edge peak region. (b) Magnified data in the XANES region at the main absorption edge. (c-e) Ex situ XPS results for (c) pristine, (d) discharged, and (e) charged V_6O_{13}.

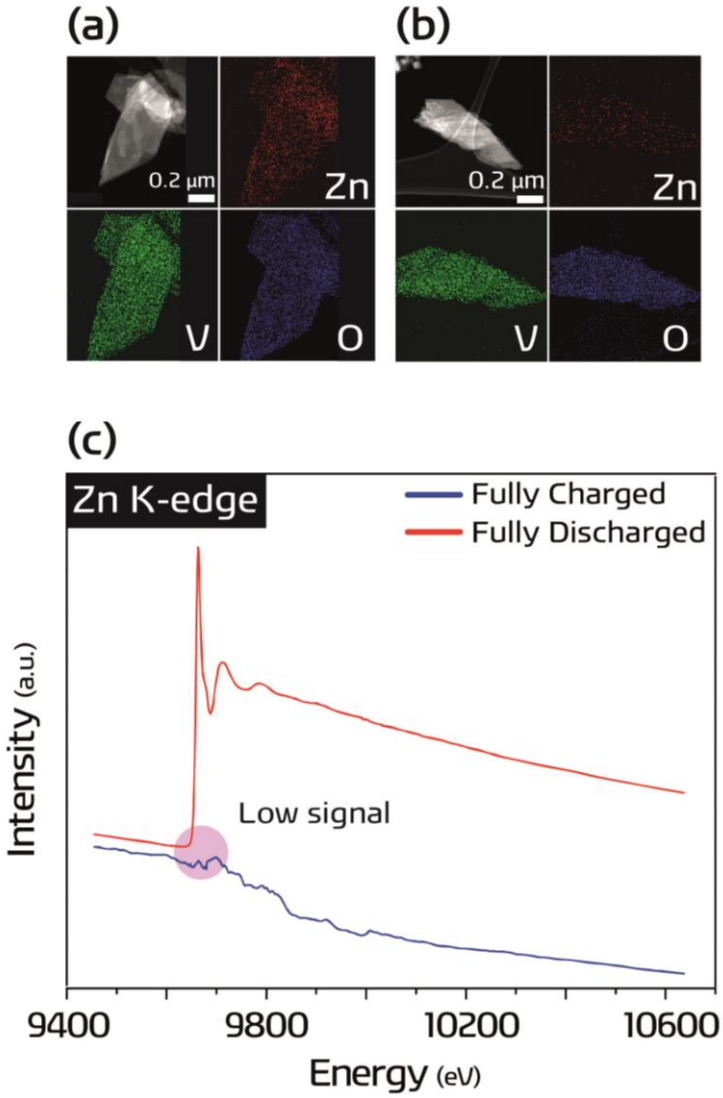

Figure 2-7. (a, b) *Ex situ* EDS results for (a) discharged and (b) charged samples in aqueous electrolyte. (c) *Ex situ* XAS Zn K-edge results (transmission mode) for (dis)charged electrodes in aqueous electrolyte. Electrode mass loading was in the range of 1.5 – 2.0 mg cm^{-2} for both electrodes. These are the same electrodes as those shown in **Figure 2-6a**.

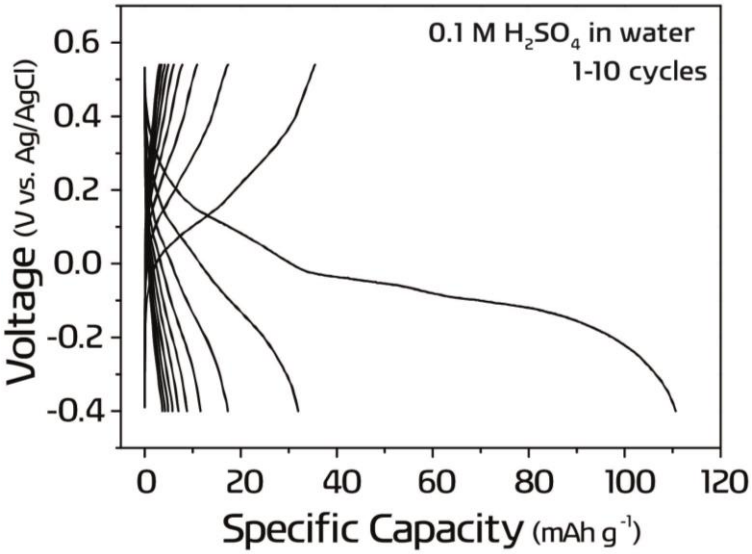

Figure 2-8. Galvanostatic profile of V_6O_{13} cycled in a three-electrode beaker cell configuration with 0.1 M H_2SO_4 aqueous electrolyte.

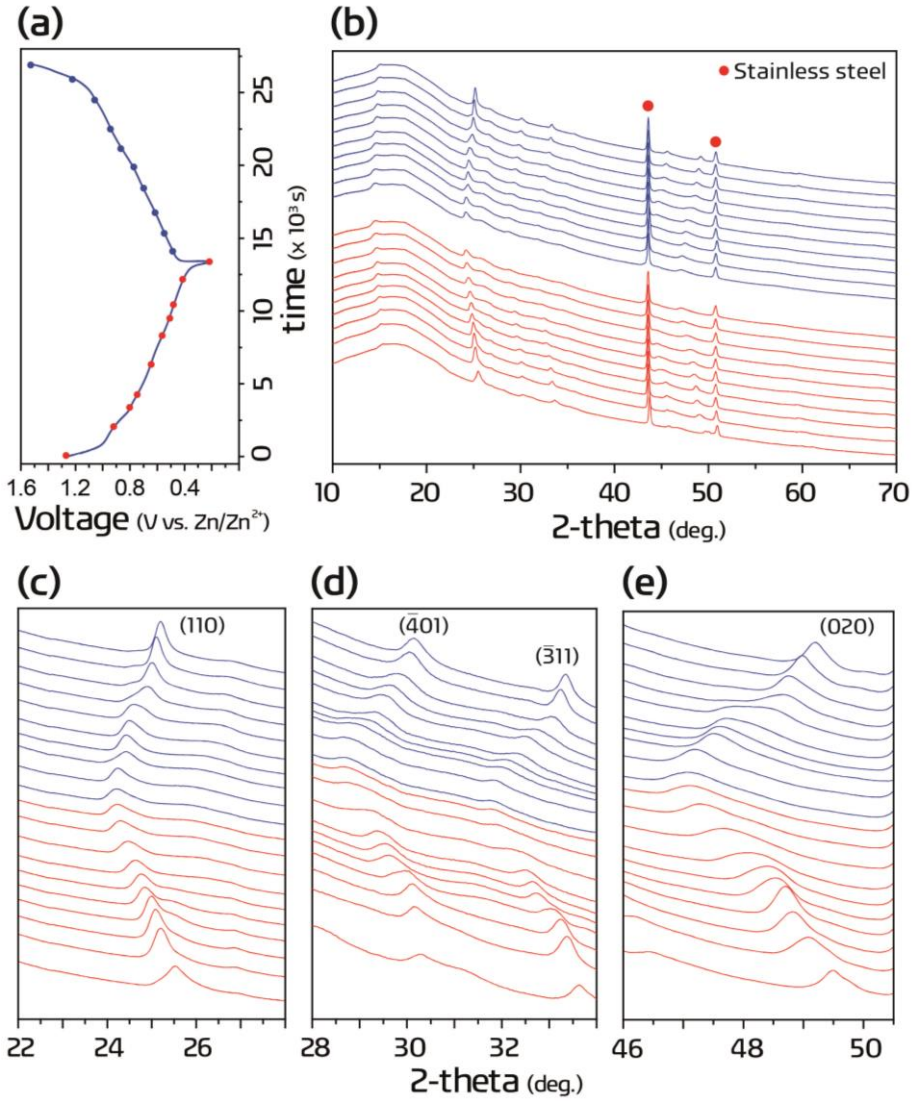

Figure 2-9. *In situ* synchrotron XRD results for Zn/V_6O_{13} aqueous coin cells cycled at 100 mA g^{-1}. (a) Galvanostatic voltage-time profile for *in situ* analysis. The red and blue dots correspond to each XRD profile in Figure 2-7b. (b) Overall XRD results for wide 2θ range. (c-e) Magnified XRD profiles at specific 2θ ranges for different planes.

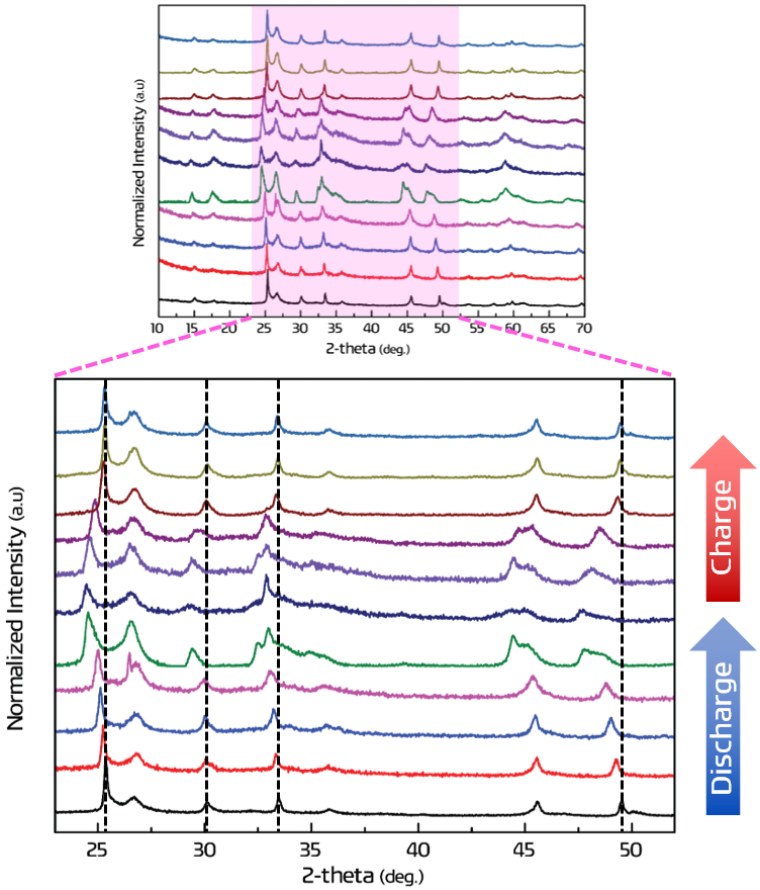

Figure 2-10. *Ex situ* XRD results for V_6O_{13} after one cycle.

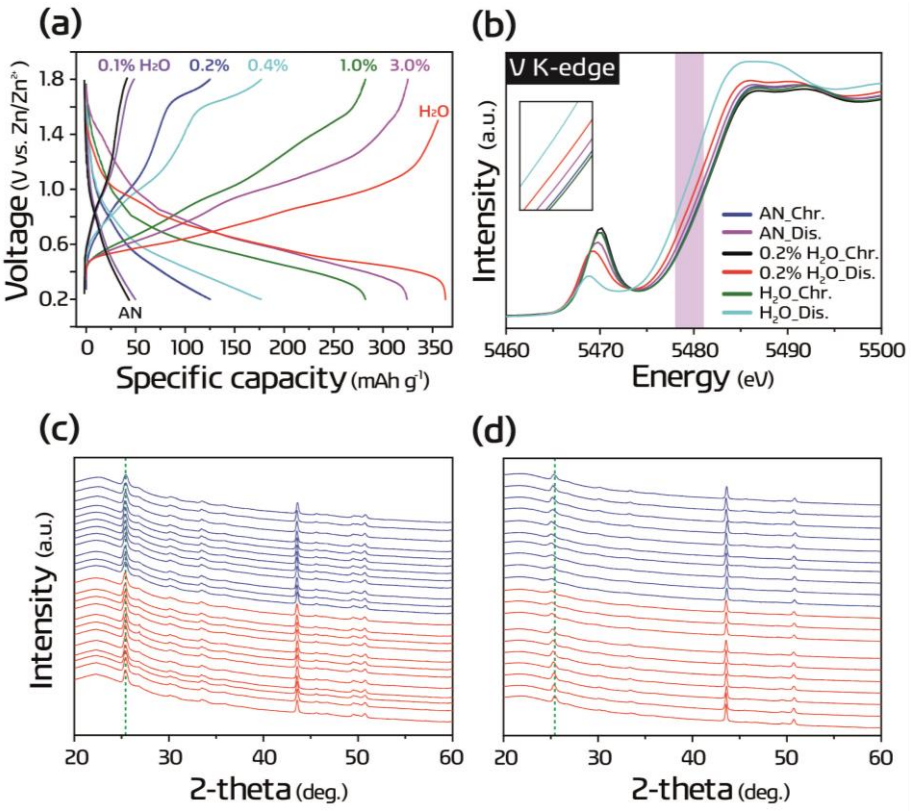

Figure 2-11. (a) Galvanostatic voltage-capacity profiles for V_6O_{13} cycled in electrolytes with increasing water content in 1 M $Zn(CF_3SO_3)_2$ acetonitrile (anhydrous). Each profile corresponds to the 10th cycle. (b) *Ex situ* XAS results (transmission mode) for charged (Chr) and discharged (Dis) V_6O_{13} electrodes in electrolytes containing no water, 0.2 mol% H_2O in AN, and pure water in 1 M $Zn(CF_3SO_3)_2$. Each electrode was cycled five times before measurement. (c-d) In situ XRD results for V_6O_{13} cycled in (c) 1 M $Zn(CF_3SO_3)_2$ in acetonitrile (anhydrous) and (d) the same electrolyte with 0.2 mol% H_2O added. Galvanostatic conditions of 40 mA g^{-1} were selected for these experiments.

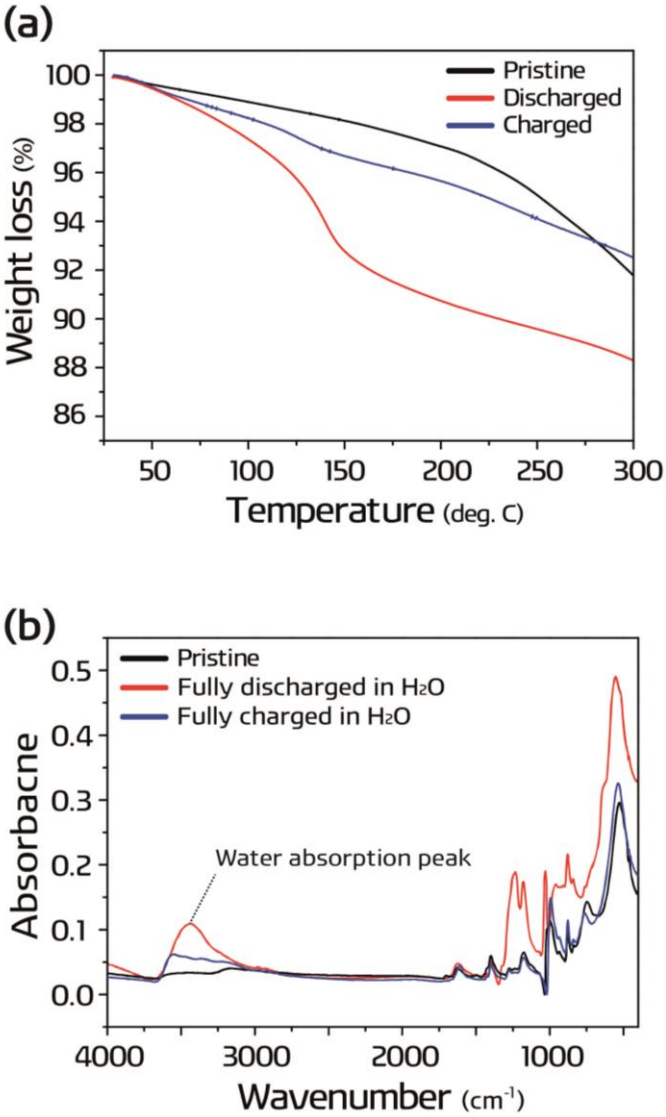

Figure 2-12. (a) *Ex situ* TGA results for pristine, charged, and discharged samples in aqueous electrolyte. (b) *Ex situ* FT-IR spectra for pristine, charged, and discharged samples in aqueous electrolyte. Each electrode was cycled five times before measurements.

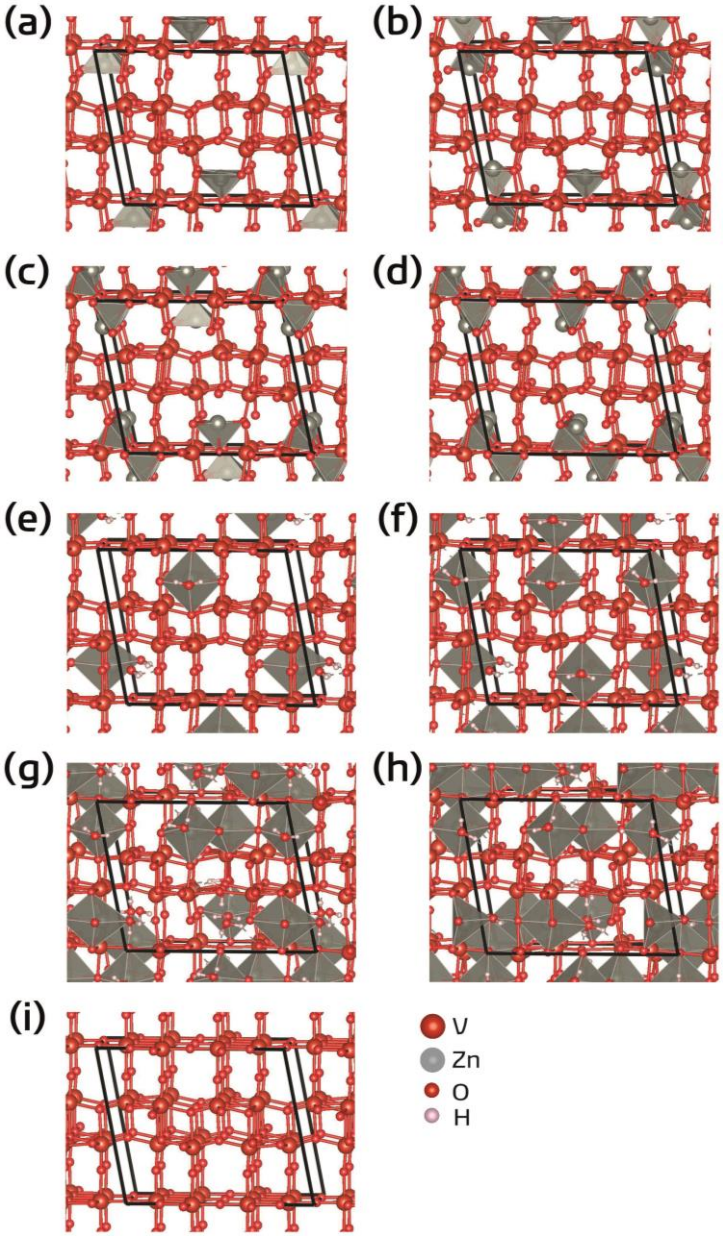

Figure 2-13. Optimized geometry from DFT calculations. (a) 0.5 Zn, (b) 1.0 Zn, (c) 1.5 Zn, and (d) 2.0 Zn inserted into V_6O_{13} without water. (e) 0.5 Zn, (f) 1.0 Zn, (g) 1.5 Zn, (h) 2.0 Zn inserted into V_6O_{13} with water. (i) pristine V_6O_{13}.

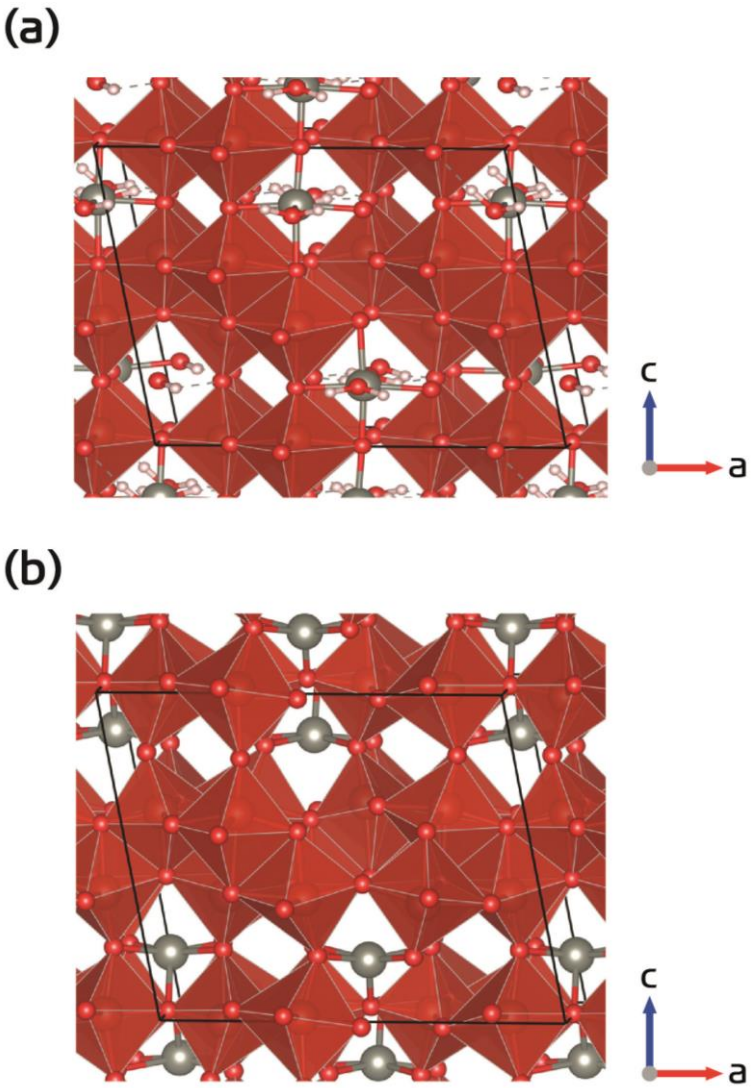

Figure 2-14. Optimized geometry of Zn-intercalated V_6O_{13} (a) with water and (b) without water.

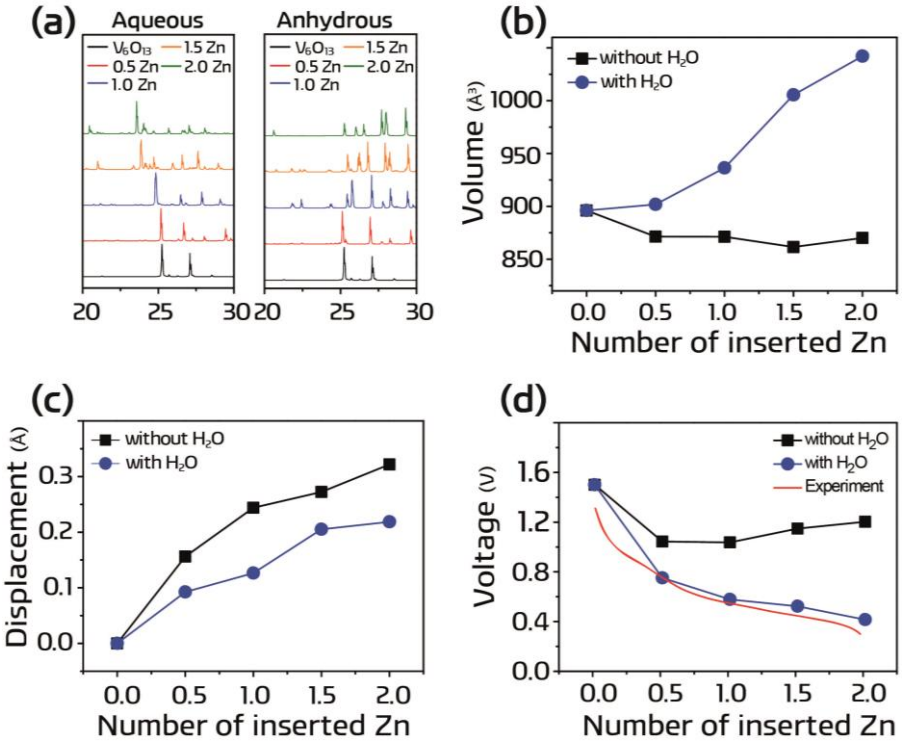

Figure 2-15. DFT calculation results for V_6O_{13} with Zn intercalation. For varying amounts of Zn intercalation into V_6O_{13}, (a) simulated XRD results with and without water, (b) unit cell volume changes during intercalation with and without water, (c) atomic displacement with and without water, and (d) calculated voltage profiles with and without water.

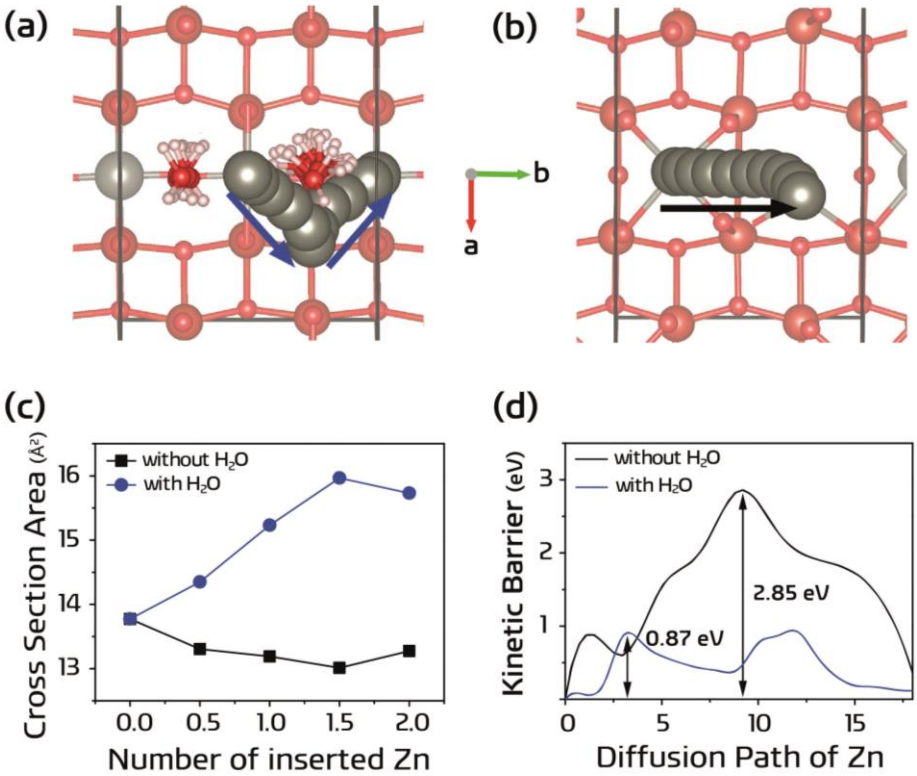

Figure 2-16. Diffusion paths of Zn within V_6O_{13} (a) with water and (b) without water obtained from NEB calculations. (c) Changes in cross-sectional area of Zn diffusion paths with and without water. (d) Calculated diffusion barriers for paths in (a-b).

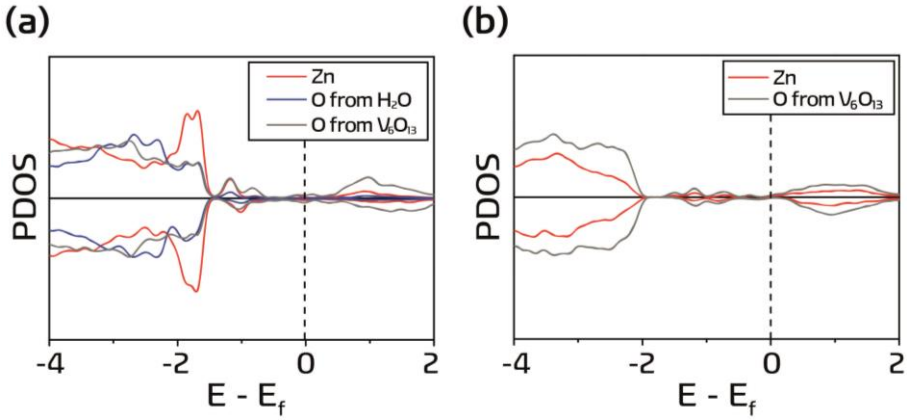

Figure 2-17. Change in projected density of states (PDOS). (a) PDOS of Zn and O in cathode with water. (b) PDOS of Zn and O in cathode without water.

# of Zn intercalated	Δ Charge (e^-)
0.5	– 0.167
1	– 0.113
1.5	– 0.108
2	– 0.101

Table 2-1. Zn charge difference between the cases with and without water during the course of Zn intercalation.

* All text, figures, and tables of Chapter 2 in this dissertation have been reproduced with the permission of Wiley-VCH. Copyright 2019.[7c]

3. The Importance of Zinc Metal Anodes in Aqueous Zinc Ion Batteries

3.1 Background: renewed interest in Zn anodes

Zn offers several advantages in aqueous electrochemical systems. First, not only is it readily accessible and relatively cheap as a resource, but it is also known for its non-toxicity and chemical stability in aqueous media compared to alkali metals such as lithium or sodium.[19b] Second, in mildly acidic conditions (pH = 4 - 6), Zn is oxidized to Zn^{2+} without forming intermediate phases[79] and possesses a high overpotential for hydrogen evolution reactions (HER).[80] Third, considering the rather narrow operating window beyond which gas (H_2, O_2) evolution occurs in water,[81] Zn has a suitable redox potential of – 0.76 V (vs. standard hydrogen electrode) for battery operation. Lastly, Zn possesses a high theoretical capacity (820 mAh g^{-1}, 5854 mAh L^{-1}) in its metallic state.

The use of Zn in aqueous batteries is not a new concept. In fact, commercial batteries such as Zn-air and Zn-MnO_2 contain alkaline electrolytes as media for discharge electrochemistry. Unfortunately, most commercial batteries that employ aqueous zinc chemistry are primary in nature, with limited rechargeability at best. This is mainly due to the different chemical behavior of Zn under different pH conditions, as demonstrated by the Pourbaix diagram in **Figure 3-1a**. Above a certain pH, Zn forms hydroxides and oxides upon

discharging. This is common in alkaline environments, a phenomenon that entails severe dendritic growth and/or passivation on the Zn metal surface (**Figure 3-1b**).[82] Consequently, the reverse process (charging) is limited in its capacity due to diminished active material, worsening the rechargeability of a battery. This issue has been discussed in numerous publications[83] and will not be dealt with in this perspective. On the other hand, the Pourbaix diagram also indicates that the formation of such discharge products can be avoided simply by changing the pH of the solution. At near-neutral pH levels, Zn takes a direct reaction pathway to form Zn^{2+} ions upon discharge. The absence of discharge products such as Zn-hydroxides and ZnO makes it easy to charge the battery, where Zn^{2+} is reduced to its metallic state ($Zn^{2+} + 2e^- \rightarrow Zn$). This has played a key role in revitalizing academic interest in AZIBs as post-LIB systems.

The use of mildly acidic aqueous electrolytes dates back to the 1980s when Yamamoto et al.[26] first reported on the electrochemical behavior of Zn in a $ZnSO_4$ aqueous electrolyte (paired with MnO_2), fueling the battery community's interest in rechargeable AZIBs in recent years. Such interest has led to the search for viable candidates for cathode materials, partly due to the long-held belief that multivalent ion (de)intercalation is a formidable task in most materials. This search has resulted in numerous investigations probing the performance and reaction mechanisms of potential cathode materials, the results of which are summarized well in other review articles.[19a, 19b, 79]

As important as it is to continue the search for suitable cathode

materials, such growing interest in AZIBs warrants a careful examination of other battery components, especially the Zn anode. In most situations, the cathode of interest is paired with a Zn metal anode in a mildly acidic electrolyte. Zn metal is often used in excess to offset its potential fading effects on the overall cell performance. While this approach is commonplace for investigating the cathode, it also renders the entire system impractical because excess electrode material inevitably results in diminished energy density. In other words, maximum energy density can only be achieved by minimizing the weight/volume of individual components, among which excess Zn metal takes up a significant portion. Thus, the ideal scenario would certainly entail a precise balance between the amount of Zn needed at the cathode and that supplied by the Zn anode.

Unfortunately, this is easier said than done. Although the Pourbaix diagram indicates a direct redox process between Zn and its cationic form (without formation of intermediate compounds), the deposition/stripping behavior of Zn is a different story. In order to minimize the amount of Zn while ensuring the same level of performance, maximum reversibility must be achieved. This involves increasing the ratio between the amount of Zn^{2+} ions generated upon discharge (stripping) and that deposited at the anode upon charge (plating). In more familiar terms, the Coulombic efficiency determines the extent of reversibility. Unfortunately, despite the use of near-neutral aqueous electrolytes, the behavior of Zn metal anodes in electrochemical

systems is far from ideal. In fact, Zn anodes suffer from problems such as dendritic growth and passivation, which ultimately results in low reversibility.[84] In turn, excess Zn must be employed to compensate for the continuous loss of usable Zn during cycling, resulting in a fatal setback in energy density. The strenuous efforts to discover high capacity/voltage cathodes for AZIBs may all be for nothing if their full potential cannot be realized due to mediocre anode performance.

Therefore, in light of the recently sparked interest in AZIBs, this chapter discusses an often overlooked issue: the Zn metal anode. The chapter is structured as follows. In the first section, recent investigations with Zn metal anodes in mildly acidic aqueous systems will be briefly summarized with the following questions in mind: i) In what manner does Zn deposit on the Zn metal surface? ii) How does this relate to irreversibility? iii) What types of strategies should be implemented to enhance reversibility? In doing so, we hope to extract valuable lessons on which future research initiatives can be embarked. In the following section, we examine the ramifications of Zn metal reversibility on energy density. A summary of energy density calculations for selected works are provided for different Zn amounts, along with hypothetical calculations for various Coulombic efficiency scenarios to grasp the implications of these two factors on the final energy density of an AZIB. Lastly, we conclude this chapter by summarizing the key points and providing an outlook regarding this field.

3.2 Zn electrochemistry in aqueous media

Zn exhibits different electrochemistry in different environments. Typically, upon discharge, Zn metal is oxidized to Zn^{2+} (electro-oxidation), whereby the generated electrons are transferred to the cathode through an external circuit. The pH of the electrolyte determines what happens next. In alkaline media, the oxidized Zn^{2+} ions form $Zn(OH)_4^{2-}$ complexes (complexation) due to the abundance of hydroxide ions in the vicinity of the anode. These zincate ions not only diffuse away from the surface due to a concentration gradient, resulting in a loss of active material, but also precipitate in the form of ZnO (dehydration/precipitation) once the local solubility limit of zincate is reached. Such precipitation results in dendritic growth and/or passivation, impairing the rechargeability of batteries that employ alkaline aqueous electrolytes (**Figure 3-1b**). Thus, Zn-air, Zn-MnO_2, and Ni-Zn batteries that utilize 6 M KOH solutions are mostly primary in nature. The reactions mentioned above are summarized below.[85]

$$\text{Electro-oxidation: } Zn(s) \rightarrow Zn^{2+}(aq) + 2e^-$$

$$\text{Complexation: } Zn^{2+}(aq) + 4OH^-(aq) \rightarrow Zn(OH)_4^{2-}(aq)$$

$$\text{Dehydration/Precipitation: } Zn(OH)_4^{2-}(aq) \rightarrow ZnO(s) + H_2O(l) + 2OH^-(aq)$$

In mildly acidic media (pH 4 ~ 6), such a series of reactions is suppressed. In contrast to alkaline environments, this pH window permits Zn^{2+} ions to exist in their ionized form. By employing salts such as $ZnSO_4$ or

$Zn(CF_3SO_3)_2$ that offer mildly acidic aqueous solutions, reversible Zn plating/stripping becomes possible to a certain extent. Thus, recharging the battery becomes much easier by means of the following reactions.

$$\text{Stripping (discharge): } Zn(s) \rightarrow Zn^{2+}(aq) + 2e^-$$

$$\text{Plating (charge): } Zn^{2+}(aq) + 2e^- \rightarrow Zn(s)$$

Unfortunately, a lower pH also means that the potential for HER is higher, as predicted by the Nernst equation and the resulting Pourbaix diagram. For example, the HER potential for a pH = 10 electrolyte is calculated to be - 0.59 V (vs. SHE), while that for a solution with pH = 4 is - 0.236 V (vs SHE). This implies that low pH solutions are more susceptible to HER during a cathodic step. In fact, this is quite higher than the standard reduction potential of Zn (- 0.76 V vs. SHE), indicating thermodynamic favorability for HER rather than Zn deposition. However, kinetics says otherwise. In fact, different metal surfaces exhibit different kinetic overpotentials for surface reactions such as HER. Luckily, Zn metal is equipped with the advantage that HER is significantly deterred from occurring on its surface due to kinetic overpotential.[80, 86] As a result, the actual potential at which hydrogen gas evolves is significantly lowered, making it possible for Zn to deposit instead (**Figure 3-1c**). However, it must be noted that the extent of the overpotential highly depends on the applied current density. Thus, the C-rate of an AZIB is a crucial parameter that determines the competition between gas evolution and

Zn deposition.

3.3 Zn deposition in aqueous media

Before delving into recent works, it is helpful to consider the manner in which Zn metal deposits/dissolves at the surface. This process is not much different from that of lithium (Li) metal in Li-ion batteries (LIBs). Assuming a symmetric cell configuration where both the counter and working electrodes are Zn metal foils, when a negative potential is applied to the working electrode, the mobile Zn^{2+} ions are driven toward the working electrode. Upon reaching the Zn surface, these ions are reduced and deposited in the form of metallic Zn. Simultaneously, metallic zinc at the counter electrode is oxidized into its corresponding ions for the sake of charge neutrality (**Figure 3-1d**).

However, the different operating environments and innate differences between Zn and Li (aqueous vs. non-aqueous) have profound implications on the resulting electrochemistry at the respective anode surfaces, especially with respect to the SEI. In the case of Li metal batteries, an organic solvent with Li salt is used as the electrolyte. The extremely low standard reduction potential of Li (- 3.04 V vs. SHE) implies its strong tendency to oxidize, which manifests in the form of a spontaneously generated, native SEI layer upon contact with the electrolyte. Moreover, when a reductive potential is applied, the electrolyte is decomposed to form a SEI layer consisting of inactive components such as

LiF, Li_2CO_3, Li_2O, and R-OCO_2Li. This SEI formation is prior to Li plating in terms of potential and is based on consuming the electrolyte.[87] It goes without saying that a vicious exothermic reaction occurs when Li is exposed to an aqueous environment, forming LiOH and H_2 gas products. On the other hand, Zn is relatively stable in both non-aqueous and aqueous environments, meaning that the spontaneous formation of a SEI layer is insignificant. In fact, Zn directly deposits on the bare Zn surface, leaving some regions exposed to side reactions such as HER and/or the formation of undesirable, inactive products.

The SEI plays an ambivalent role. On one hand, a SEI that is i) a dense and uniform, ii) ionically conducting, iii) electronically insulating, and iv) mechanically/chemically stable would constitute an ideal scenario where metal anodes are protected from parasitic reactions that undermine discharge-charge efficiency.[88] Moreover, in LIBs, the SEI extends the electrochemical stability window and allows Li metal to operate in a more reductive environment. On the other hand, as these conditions are hardly met in reality with metallic electrodes in non-aqueous electrolytes, a resulting unstable SEI is usually a major performance deterrent.

The absence of a SEI creates its own set of problems. In the case of Li metal, failure to passivate the surface with a stable SEI would lead to unwanted side reactions that involve Li and electrolyte consumption, undermining cell performance. More importantly, Zn is susceptible to some degree of HER in aqueous environments (where a SEI does not exist) despite kinetic limitations.

Not only does this consume the electrolyte solvent, but it can also corrode the metal surface and cause locally “dead” regions on which Zn deposition cannot occur. Furthermore, as HER is a reduction process, some portion of the electrons transferred to the Zn electrode are used for proton reduction rather than Zn deposition. This inevitably diminishes plating efficiency. Thus, be it aqueous or organic, any metal-based battery chemistry can benefit from a well-formed SEI, but only if its drawbacks are thoroughly addressed.

Therefore, while a mildly acidic environment enables direct plating/stripping of Zn, the lack of a well-formed, protective SEI may subject it to detrimental reactions that degrade its reversibility. Accordingly, numerous research efforts are invested in addressing this dichotomy by attempting to improve the performance of Zn metal anodes. Recent investigations take various routes in attempting to heighten their reversibility, most of which can be divided into four categories: i) electrolyte formulation, ii) electrode modification, iii) host development, and iv) electrochemical modulation.

3.4 Recent works with Zn in mildly acidic electrolyte

3.4.1 *Electrolyte formulation*

The electrolyte is a crucial component in enabling high performance AZIBs. Not only does its pH dictate the reaction mechanisms at the surface, but the type of salt also has a significant impact on the electrochemical and

morphological characteristics of the Zn anode. In this respect, Zhang *et al*. conducted a systematic investigation of the effect of different salts and their electrochemical profiles.[28b] A survey of four mildly acidic solutions of $ZnCl_2$, $Zn(NO_3)_2$, $ZnSO_4$, and $Zn(CF_3SO_3)_2$ revealed that while nitrate- and chloride-based electrolytes were unfit for reversible deposition/dissolution, sulfate- and triflate-based solutions offered favorable environments for this process. In particular, the Zn-triflate electrolyte exhibited high stability (**Figure 3-2a**), supposedly due to a reduced solvation effect from the presence of bulky anions. In a high concentration of 3 M $Zn(CF_3SO_3)_2$, *ex situ* SEM images after galvanostatic cycling indicate a smooth morphology of Zn deposition (**Figure 3-2b**). Ever since, the $Zn(CF_3SO_3)_2$ salt has often been employed in many studies focusing on exploring cathodes for AZIBs.

In the context of anode optimization, however, the Zn triflate salt alone is not enough to meet the ever-increasing expectations of the battery community in terms of performance and cycle life. Moreover, its high cost compared to $ZnSO_4$ could negate its relative electrochemical stability.[89] Various alternative strategies have been explored in this regard, among which electrolyte manipulation is a popular research direction. With the common purpose of heightening Coulombic efficiency and suppressing dendrite formation, numerous formulations including triethyl phosphate (TEP),[90] polyacrylamide (PAM),[91] polyethyleneamine,[92] bio-ionic liquid,[30a] Ni triflate,[93] SDBS,[94] $Zn(ClO_4)_2$,[95] and deep eutectic solvents like acetamide-

$Zn(TFSI)_2$[96] have been reported as performance-enhancing electrolytes. In addition, the effect of salt concentration on cell performance has been discussed with conventional salts such as $ZnCl_2$[97] and $ZnSO_4$.[98] In terms of performance, the use of TEP and PAM demonstrates impressive results. Naveed *et al*. employ a co-solvent approach with a 0.5 M $Zn(CF_3SO_3)_2$ in TEP:H_2O (7:3) electrolyte formulation. The use of this composition induces a well-connected, porous network of Zn rather than the commonly observed dendritic morphology (**Figure 3-2c**). This non-dendritic deposition behavior translates into dramatically enhanced cycle life and Coulombic efficiency levels (**Figures 3-2d, e**). The underlying cause for different morphologies has yet to be elucidated, but this strategy clearly demonstrates the importance of the relation between initial deposition morphology and electrochemistry. On a related note, PAM has also been reported to serve as an effective mediator for smooth Zn deposition (**Figure 3-3a**). Galvanostatic tests in symmetric cells confirm the positive effect of PAM, as evidenced by the stable nucleation overpotentials along with extended cycle life (**Figure 3-3b**). These results are corroborated with DFT calculations that indicate a higher binding energy between the acyl groups of PAM and Zn atoms. In this sense, PAM is capable of guiding uniform Zn deposition at the electrode/electrolyte interface, reaffirming the crucial relationship between deposition morphology and electrochemical stability.

Another interesting study was recently conducted by Wang *et al*. involving the use of an extremely high concentration electrolyte.[39] Instead of

an additive, they opted for a “water-in-salt” electrolyte formulation. This strategy takes advantage of the fact that the nature of the coordination environment of the metal cation in solution can be changed on a molecular level, inducing a completely different electrodeposition morphology and electrochemistry. In moderate concentrations, Zn^{2+} cations are usually solvated by water in a six-fold coordination in bulk water.[99] However, the conventional solvation sheath structure can be altered at sufficiently high concentrations, such as 1 M $Zn(TFSI)_2$/20 M Li(TFSI) in water. Close ion pairs $(Zn\text{-}TFSI)^+$ form due to the abundance of anions in the vicinity of Zn^{2+} cations, suppressing the presence of $(Zn\text{-}(H_2O)_6)^{2+}$. This is confirmed through experimental (FT-IR and ^{17}O NMR) and molecular dynamics simulations (**Figure 3-4a**), where the cations are coordinated with the oxygen atoms of the TFSI anions rather than those of bulk water molecules. Such an altered coordination environment. Accordingly, dense, non-dendritic deposition occurs (**Figure 3-4b**), leading to a high Coulombic efficiency of ~ 100% in plating/stripping tests (**Figure 3-4c**) in a high concentration electrolyte, as well as significantly enhanced cycling stability in hybrid configurations with $LiMn_2O_4$ and $Zn\text{-}O_2$ batteries.

This particular work teaches us an important lesson: water is an essential component in aqueous batteries, but its activity may have negative consequences with respect to Zn anode performance. Wang *et al*.[39] speculate that this could be tied to the solvation sheath structure of Zn in an aqueous environment. The bivalent nature of the Zn^{2+} cation induces strong interaction

with surrounding water molecules. This would incur a high de-solvation energy penalty upon deposition, driving localized growth in energetically favorable spots on a microscopic scale. On a related note, the presence of bulk water would also expose the Zn anode to side reactions such as HER. Although there is a kinetic overpotential to overcome for this reaction, HER may occur to some extent and destabilize the anode. There has yet to be a definitive explanation with respect to the downside of water-based electrolytes, but it is becoming increasingly clear that other cell components can be utilized to mitigate those drawbacks associated with water.

3.4.2 *Electrode modification*

A widely adopted strategy is concerned with constructing new types of electrodes *via* coating or mixing additives with active Zn. Some examples include sputtering gold nanoparticles,[100] carbon-zinc composites,[101] and coating with materials such as carbon nanotubes,[102] graphene oxide (*via* spontaneous reduction),[103] polyamide,[104] $CaCO_3$,[105] TiO_2,[106], and 3D ZnO.[107] Several strategies stand out. First, modifying the electrode/electrolyte interface with an inorganic coating layer can result in enhanced electrochemical performance. In this approach, Zhao *et al*. recognize the importance of applying a thin, homogeneous coating, thus employing the well-established atomic layer deposition (ALD) technique to apply a ~ 8 nm-thick TiO_2 coating on Zn metal (**Figure 3-5a**). In doing so, the TiO_2 coating acts as a passivation layer to prevent direct contact between the electrode and electrolyte, avoiding

undesirable gas evolution at the interphase. The degree to which gas evolution occurs is evidenced by the formation of $Zn(OH)_2$, which is catalyzed by the local increase in [OH^-] due to HER at the surface. Under this assumption, it is indeed the TiO_2-coated Zn that shows less HER, as shown by the lower degree of $Zn(OH)_2$ formation from the *ex situ* XRD in **Figure 3-5b**. SEM images of cycled pristine and coated Zn electrodes also show a flaky deposition morphology for bare Zn, whereas that for coated Zn appears more dense in nature. Symmetric cell tests reflect the positive effect of such a coating layer, evidenced by a distinctly stable voltage profile for TiO_2-coated Zn. A similar approach was taken by Kang *et al*. where an inorganic $CaCO_3$ coating layer was coated on Zn metal (**Figure 3-6a**).[53] In this case, the high porosity of the coating layer allows the electrolyte to readily infiltrate the electrode, inducing a relatively uniform plating morphology with small-sized Zn nuclei, which also resulted in improved performance.

Second, inducing easier nucleation at the surface is an interesting approach.[100] Zhi *et al*. implemented this strategy by sputtering gold nanoparticles (Au NPs) on the surface of Zn (**Figure 3-6b**). The Au NPs were dispersed *via* ion sputtering and the resulting morphology appears uniform. In essence, the Au NPs are intended to serve as seeds for facile Zn nucleation and deposition, whereas such nuclei are absent on bare Zn foil. The effects of this strategy are confirmed by the vastly different deposition morphology in **Figure 3-6c**, where the Au-sputtered host (top right) guides a compact manner of Zn

deposition compared to the control sample (top left). The electrochemical effects of this strategy are significant, shown by lower nucleation overpotentials and prolonged cycling (bottom).

Third, a polymer coating strategy was employed by Cui *et al*.[104] Taking a lesson from metal brighteners, the authors simply coated Zn foil with a polyamide (PA)/$Zn(CF_3SO_3)_2$ solution in order to suppress dendritic Zn growth (**Figure 3-7a**). As a result, Zn was able to deposit in a uniform, compact manner whereas a bare Zn electrode shows a less dense morphology (**Figure 3-7b**). The difference in deposition behavior translates to electrochemical stability, where the coated Zn exhibits a drastic improvement in cycle life (**Figure 3-7c**). Synergy between ion conduction and metal protection is key to this work. A uniform coating layer protects the Zn anode from HER and undesirable side products while the trapped Zn salt allows ionic conduction toward the coating/metal interface and transfers non-solvated Zn^{2+} ions for deposition. Ultimately, the protection layer induces reversible Zn plating/stripping beneath the layer, leading to enhanced electrochemistry.

The aforementioned works highlight the importance of uniform deposition in their own way. An extremely thin, inorganic TiO_2 layer notably mitigates HER, reducing passivation by undesirable side products such as $Zn(OH)_2$. Accordingly, more Zn remains active over cycling, inducing a higher, uniform utilization of the entire electrode on a macroscopic scale. Au-sputtered Zn electrodes act in a similar fashion, where Au NPs facilitate the nucleation

of Zn by serving as pre-formed seeds. Assuming uniform dispersion, this also allows for a uniform, reversible manner of Zn deposition. Furthermore, coating Zn foil with a protective polymer layer infused with Zn salt is an effective strategy. The coating layer mitigates the possibility of side reactions originating from water while facilitating ionic conduction toward the layer/metal interface, inducing a dense and compact deposition step underneath the layer. Thus, it appears that a positive relationship exists between deposition uniformity and reversibility.

3.4.3 *Host-type anodes*

Taking a lesson from a myriad of research initiatives in Li metal batteries, several works report the benefits of using Zn hosts rather than bare Zn metal as efficient anodes for AZIBs. While there are numerous works concerned with hosts for Li, relatively few works deal with developing good hosts for Zn. Nevertheless, a few examples are described in this section in order to convey the promise of this strategy.

The main reason for using a separate host for Zn rather than bare Zn foil lies with the need for electrodes that offer higher capacity and Coulombic efficiency levels. This can be achieved in many ways, such as utilizing materials with different form factors (usually with high surface areas) or physicochemical modification of pre-existing surfaces and/or materials. Once the hosts are proven to work, they are filled to a fixed capacity of Zn (*via* electrodeposition) to be paired with a cathode in full cell tests.

A typical example of materials with different form factors is demonstrated by Wang *et al*.[108] Conductive graphite fiber (GF) is employed as such a substrate in order to deposit Zn under a constant potential of – 1.0 V (vs. Zn/Zn^{2+}) in a two-electrode setting (**Figure 3-7d**). A comparison with Zn foil shows that the GF-Zn host offers higher stability at an areal capacity of 1 mAh cm^{-2} (**Figure 3-7e**). While it is unclear if the original morphology is maintained during cell operation, the proposed host seems to offer lower overpotential and cycling stability through its large electroactive surface area.

ZIF-8-derived hosts are a good example of making use of pre-existing materials, a strategy demonstrated by Wang *et al*. ZIF-8 is a zeolitic framework in which ZnN_4 tetrahedral units are bridged with imidazolate linkers to form a three-dimensional structure.[109] Upon annealing this material in an inert atmosphere, one can create a microporous host matrix with trace amounts of metallic Zn nuclei. This causes partial decomposition of the original ZIF-8, but retains its original morphology and well-dispersed Zn particles. The annealed ZIF-8 is initially plated with Zn at an areal capacity of 10 mAh cm^{-2}, which is used as an anode in plating and symmetric cell tests. In fact, electrochemical plating tests with a wide range of areal capacities reveal high Coulombic efficiency levels approaching 99.8% as well as alleviated dendritic growth (**Figures 3-8a, b**). Such improved performance is mainly attributed to the presence of well-dispersed Zn^0 particles from ZIF-8, which induce uniform deposition at the electrode.

Mesh-type substrates are also promising hosts for Zn. Zhang *et al*. demonstrate the merits of using copper (Cu) mesh as a three-dimensional host (**Figure 3-3a**).[91] Note that the same article has been discussed previously in the "electrolyte formulation" section with respect to the PAM additive. Macroscopically, the unique, three-dimensional form factor of Cu mesh allows easier access to the electrolyte, inducing thorough electrodeposition of Zn. Similar approaches confirm the potential of Cu in such form factors in other works.[110] Interestingly, the same cannot be said for other foam-type electrodes such as nickel. A fundamental explanation is lacking, but this is probably related to the inherent "zinc-philicity" of the metal. A Zn-philic metal may form a self-limiting alloy phase at the interface, promoting favorable electrodeposition behavior. Zhang *et al*. briefly address this idea, claiming that Cu plays an interesting role at the atomic scale. Not only does it act as a substrate, but also as a dopant for which a minor alloy phase—$CuZn_5$—can be formed (**Figure 3-8c**). This alloy phase, compared to pure Cu, turns out to have a higher affinity toward Zn in terms of binding energy (**Figure 63-8d**) according to DFT calculations. Thus, a Cu-Zn solid solution phase formed on the Cu mesh substrate, in concert with the Zn-philic additive PAM, is deemed responsible for regulating Zn nucleation, offering enhanced cycling stability at various current densities.

Archer *et al*. take an innovative approach of inducing epitaxial Zn electrodeposition on a horizontally aligned graphene surface.[111] Taking

advantage of the fact that graphene has a low lattice mismatch for Zn, the authors were able to design a surface where the basal plane of graphene is aligned parallel to the substrate surface on a macroscopic scale (**Figure 3-9a**). This allows Zn deposition to occur in an epitaxial fashion, exhibiting preferential growth of the (002) plane as evidenced by the XRD results (**Figure 3-9b**). Upon subjecting the electrically formed anode to plating/stripping tests, high Coulombic efficiencies of > 99% over 1000 cycles, along with extended cycle life when paired with MnO_2 cathodes were observed (**Figure 3-9c**). These results have significant implications where Zn plating is concerned. Dendritic Zn usually arises from localized growth during electrochemical operation. However, if the manner in which Zn deposits at the surface can be manipulated on a microscopic scale (**Figure 3-9d**), such undesirable forms of growth can be delayed or even prevented outright to guarantee high reversibility.

These four investigations all have one thing in common: the physical/chemical traits of the host influence the manner in which Zn is electrodeposited during the initial sequence. The cases introduced above employ graphite fiber, annealed ZIF-8, Cu mesh, and meticulously aligned graphene-steel substrates in achieving this purpose. Despite the different substrates in all cases, the electrochemical performance results indicate that regulating the initial deposition of Zn is key to ensuring high reversibility in the following cycles. Developing a host with chemical affinity with Zn and/or favorable form factors appears to be a promising direction in this regard.

3.4.4 *Electrochemical modulation*

Current density is a key factor in determining the manner of Zn electrodeposition. Yang *et al*. focus on this aspect through a systematic investigation of Zn growth behavior at various current densities and propose an "electro-healing" approach to mitigate dendritic growth at high rate operation.[112] It is shown that cycle life is inversely proportional to current density; the origin of this relationship lies in the non-uniform growth of Zn at higher currents. The authors take advantage of this tendency by designing an electrochemical protocol for prolonging the lifespan of symmetric Zn cells at high current densities. This protocol includes a "healing" step, where the cell is cycled at a lower current density of 1 mA cm^{-2} for several cycles before resuming its operation in high current mode. According to the authors, once dendrites have been formed at a high current density, a low current density induces Zn to strip preferentially from the tips of these dendrites. Afterwards, plating at low current smoothens the surface through relatively uniform deposition (**Figure 3-10a**). As a result, the lifespan of cells operating at 7.5 and 10 mA cm^{-2} are extended by four- and five-fold, although both cases fail to exceed lifetimes of 20 hours (**Figure 3-10b**). On a related note, another interesting study by Glatz *et al.* revealed that, in some cases, high current densities can actually improve the cycle life of Zn anodes.[98] This appears to be in conflict with the electro-healing strategy, most likely due to inevitable differences in experimental protocols and materials. Nevertheless, both works

emphasize the importance of the relationship between current density and long-term stability, the nature of which deserves more attention.

The breadth of Zn anode-related investigations spans across a wide spectrum of strategies. The problem can certainly be tackled from many angles, but the common goal is straightforward: high reversibility. Two factors stand out as key players in achieving this objective. First, the manner of deposition dictates the presence of dendritic growth. Non-uniform deposition is at the heart of the notorious dendrite problem; localized growth leads to protrusions that are often characterized as dendrites. Inducing uniform deposition from the beginning is an obvious solution, but this is easier said than done. A majority of the summarized investigations attempt to do so from various angles such as nuclei pre-formation, electrolyte additives, and high surface area hosts. Their effects have been demonstrated through improved performance and stability, highlighting the importance of achieving a continuous, uniform manner of Zn deposition for long-lasting Zn anodes. Second, the presence of water offers an interesting perspective in using metallic Zn foil in aqueous environments. While water is an essential component as the medium for ionic conduction, its activity at the metal/electrolyte interface appears to affect the manner in which Zn electrodeposition occurs. The previously discussed two articles[39, 104] are a testament to this. High concentration electrolytes can effectively suppress the solvation of Zn^{2+} cations by water molecules, replacing them with anions instead. Anion-solvated Zn^{2+} ions migrate and plate onto the anode surface,

excluding the effect of bulk water during electrodeposition. This induces highly compact, uniform deposition that has a positive impact on the corresponding electrochemistry. The potentially adverse effect of water can be observed in another article, where a polyamide layer infused with Zn triflate salt is coated on the Zn surface to minimize its exposure to the aqueous electrolyte while ensuring ionic conductivity. It is claimed that this coating layer "sieves" the water molecules as Zn^{2+} ions migrate toward the surface, inducing a dense Zn film rather than the commonly observed dendritic morphology. Thus, two important factors must be considered for future research initiatives: i) deposition uniformity and ii) water activity.

3.5 Energy density ramifications

Energy density is the most important criterion for evaluating the commercial viability of a battery. Unfortunately, detailed calculations such as those for LIBs are rarely performed for AZIBs, as they are far from reaching a level of mass production. Nevertheless, recently booming academic interest in aqueous battery systems calls for objective standards with which interested parties can make meaningful comparisons. In this context, this section is dedicated to providing energy density calculations of several recent works and discussing the repercussions of using excess Zn metal through some hypothetical battery operation scenarios.

3.5.1 *Initial Zn loading effects: energy density calculations for recent*

works

The energy densities of the reported works shown below (**Table 3-1**) are calculated for two scenarios. The first one assumes a 100% plating/stripping efficiency, upon which the theoretical amount of Zn is calculated based on the reported capacity and loading level of the cathode. This is combined with the cathode active material weight to obtain the theoretical gravimetric energy density. Second, we consider the case where excess Zn is used as the anode (as often is the case in most academic works). The energy density is recalculated for two different disc-type Zn anodes with different thickness and weight (~ 250 μm and ~ 50 μm). Detailed assumptions below should be noted.

1. The weights of the electrode active material are the only factors considered; cell casing, packaging, separator, current collector, etc. are excluded from these calculations.

2. Active material loading levels are used as reported by the authors; if an approximate range is given, the average value is taken as the loading. If this information is missing, a loading level of 2.0 mg cm^{-2} is assumed.

3. The average operating voltage is taken as reported by the authors; if not available, it is arbitrarily taken as the approximate mid-point voltage of the galvanostatic voltage profile.

4. Two types of commercial Zn foil have been weighed and used for these calculations: i) 1.2 cm in diameter, 0.25 mm thickness: 0.205277 g and ii) 1.2 cm in diameter, 0.05 mm thickness: 0.040045 g.

5. The following equation has been used to calculate the theoretical amount of Zn for 100% efficiency:

Amount of Zn (g)

$$= Q_{cathode}(\frac{\text{mAh}}{g}) \times loading(\frac{g}{cm^2}) \times area(1.131\ \ cm^2)$$

$$\times \frac{3600\ \ s}{1\ \ h} \times \frac{1\ \ A}{1000\ \ mA} \times \frac{1}{F}(\frac{mol\ \ e^-}{96485\ \ C}) \times \frac{1\ \ mol\ \ Zn}{2\ \ mol\ \ e^-}$$

$$\times \frac{65.39\ \ g\ \ Zn}{1\ \ mol\ \ Zn}$$

6. The following equation has been used to calculate the energy density:

Energy density (Wh kg^{-1})

$$= \frac{cathode\ \ capacity(mAh) \times Avg.voltage(V)}{(cathode\ \ wt. +\ \ anode\ \ wt.)(g)}$$

The results of these calculations are tabulated in **Table 3-1**. Despite the rough manner in which these calculations were performed (in terms of selecting average voltage, capacity, and loading), they point to the vital role of the Zn anode with respect to the energy density. Clearly, the cathode mass loading and average voltage are key factors. However, the weight of the anode cannot be discounted. In fact, the type of Zn metal foil used influences these values by order(s) of magnitude, making any attempts to increase voltage, capacity, or loading irrelevant. It is no secret that commercial Zn foil is employed for investigating potential cathode materials. This is reasonable when

the cathode is the sole focus of an investigation. Unfortunately, most works report energy densities that are solely based on the weight of the cathode, which makes them appear to be competitive with conventional LIBs. However, the calculations in Table 1 suggest otherwise; one should be wary of being misled by certain calculations and heed the impact of the Zn anode on energy density.

3.5.2 *Plating/stripping efficiency*

The calculations in **Table 3-2** speak to the strong relationship between plating/stripping efficiency and cycle life. For example, a comparison of the two cases where efficiency levels are 99.9% and 99.99%, the percentage of remaining Zn after 1,000 cycles differs by ~ 54 percentage points. From a commercial standpoint, the criterion for a battery with satisfactory performance is 80% capacity retention after 1,000 cycles. If an AZIB's cycle life were to be predominantly dependent on the reversibility of the Zn anode—which could very well be the case—the Coulombic efficiency to guarantee this condition would have to be 99.9777%. Under more lenient conditions, say 60% retention after 500 cycles, this number drops to 99.9%, which is still a formidable challenge in metal plating/stripping tests.

The key to comprehending the ramifications of these calculations lies in their context. With any battery system, one must decide on the minimum performance requirements tailored to its applications (e.g. power drills, smartphones, tablet PCs, electric vehicles, etc.). This is usually given by capacity retention at a certain cycle number. As illustrated above, this criterion

determines the threshold Coulombic efficiency, allowing one to determine the amount of Zn needed at the anode, which ultimately affects the gravimetric energy density. The weight of the anode is a key metric with respect to energy density, but it should also be stressed that the target performance of a cell must be taken into consideration. Therefore, while minimizing the anode undoubtedly heightens energy density levels, this should be done in conjunction with regard for target performance levels of that specific cell.

In this context, strategies for minimizing Zn weight are essential for maximizing energy density. As reversibility plays a crucial role in weight reduction, host development is a good place to start. Assuming a reliable degree of reversibility, the amount of Zn can be customized with electrodeposition simply by designating a specific areal capacity value. This can be extended to an interdisciplinary approach, whereby integrating highly efficient hosts with strategies such as electrolyte additives could have the potential to reach a breakthrough in performance for AZIBs.

3.6 Summary

AZIBs are considered to be promising alternatives to LIBs due to their potential for safe, cheap, and high power density batteries. Notable progress has been made in this field, especially where potential cathode candidates are concerned. However, the spotlight has for too long been shone upon investigating the electrochemical behavior of said cathodes. Considering the complex nature of

Zn electrochemistry in aqueous solutions, researchers can no longer afford to neglect the massive impact that Zn anodes have in the AZIB system. In this regard, this perspective is dedicated to the Zn anode by i) discussing the manner in which Zn electrodeposition/stripping occurs, ii) addressing known problems such as dendritic growth, HER, and diminished Coulombic efficiency, iii) summarizing recent progress for improved Zn anode performance, and iv) providing simple energy density and Coulombic efficiency calculations to demonstrate the importance of devising strategies for lighter, efficient, and long-lasting Zn anodes.

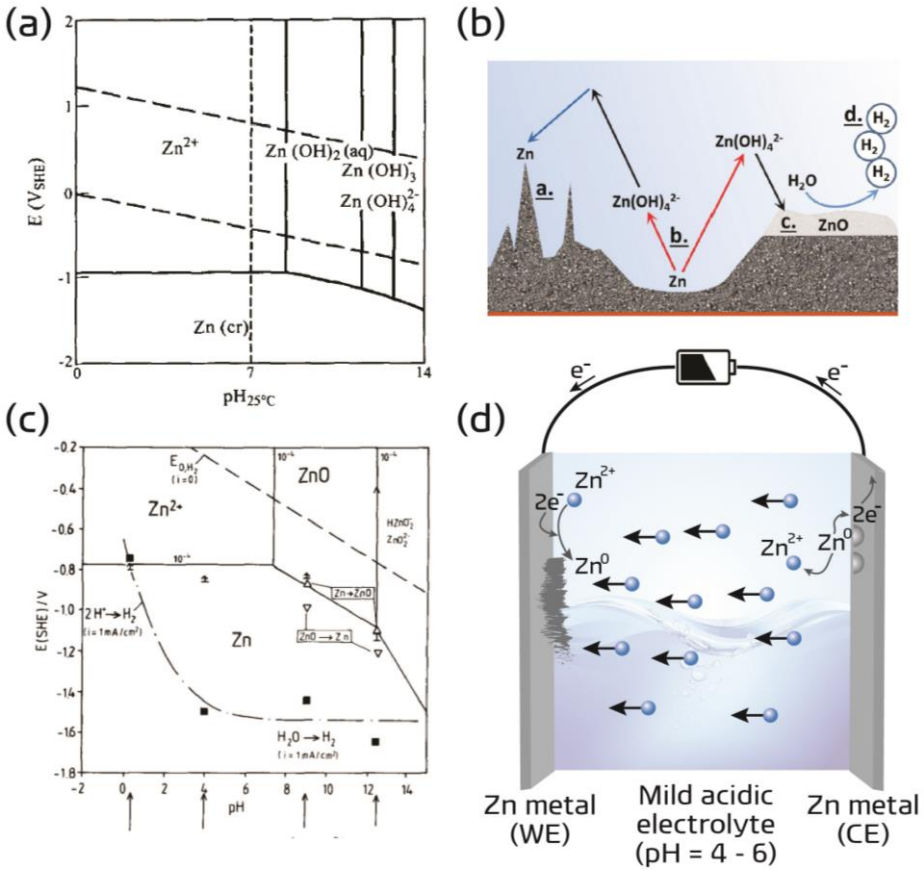

Figure 3-1. (a) Pourbaix diagram of a Zn/H_2O system. Reprinted with permission.[81] Copyright 1996 Elsevier. (b) Schematic illustration of the reaction pathways and potential problems of Zn anodes in alkaline environments. Reprinted with permission.[82] Copyright 2016 Wiley-VCH. (c) Pourbaix diagram of a Zn/H_2O system with HER overpotential considerations. Reprinted with permission.[86] Copyright 1990 Elsevier. (d) A schematic illustration of the Zn plating/stripping process in a mildly acidic environment (symmetric cell configuration).

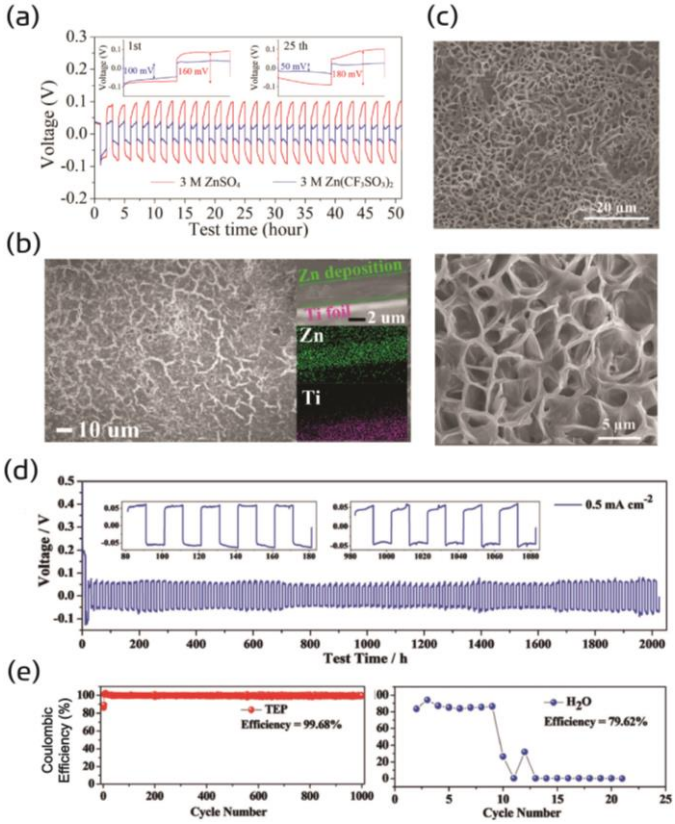

Figure 3-2. (a) Galvanostatic voltage profiles of Zn symmetric cells with 3 M $ZnSO_4$ (red) and 3 M $Zn(CF_3SO_3)_2$ (blue). (b) *Ex situ* SEM images and EDS results of Zn deposited on Ti foil at 0.2 V vs. Zn in a CV test (0.5 mV s^{-1} in 3 M $Zn(CF_3SO_3)_2$). (a-b) Reprinted with permission.[28b] Copyright 2016, American Chemical Society. (c) SEM images of Zn anode after 1000 cycles in TEP- 0.5 M $Zn(CF_3SO_3)_2$ electrolyte at 0.5 mA cm^{-2}. (d) Galvanostatic voltage profiles of Zn symmetric cells with TEP at 0.5 mA cm^{-2}. (e) plating/stripping tests on stainless steel with TEP-containing electrolyte (left) and without TEP right). (c–e) Reprinted with permission.[90] Copyright 2019, Wiley-VCH.

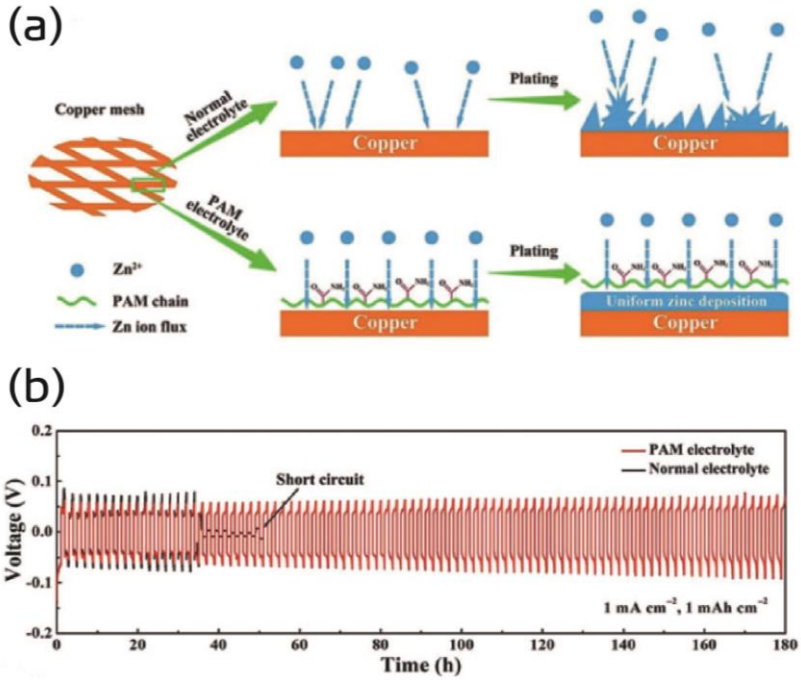

Figure 3-3. (a) A schematic illustration of Zn plating on Cu mesh with a normal aqueous electrolyte and that with a PAM additive. (b) Galvanostatic voltage profiles of Zn symmetric cells with (red) and without (black) the PAM additive at 1 mAh cm^{-2}. Reprinted with permission.[91] Copyright 2019, Wiley-VCH.

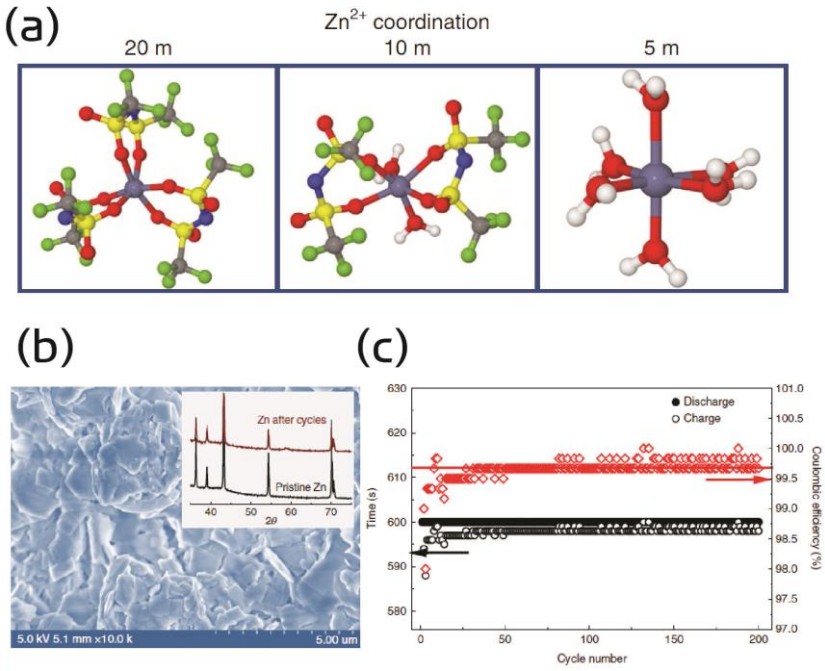

Figure 3-4. (a) Molecular dynamics simulations of Zn^{2+} coordination in different LiTFSI concentrations (20, 10, and 5 M). (b) SEM image of plated Zn in a high concentration electrolyte (20 M LiTFSI & 1 M ZnTFSI); inset: *ex situ* XRD profile of pristine (black) and cycled Zn (red). (c) Plating test results on Cu in a high concentration electrolyte. (c–e) Reprinted with permission.[39] Copyright 2018, Springer Nature.

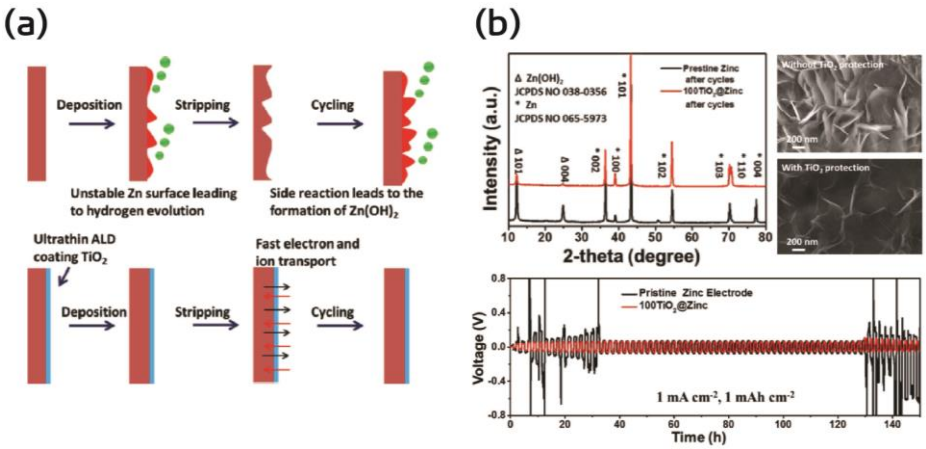

Figure 3-5. (a) A schematic illustration of Zn anode stabilization with ultrathin TiO_2 coating. (b) Ex situ XRD pattern of cycled Zn electrodes (top left) and SEM images of cycled pristine Zn and TiO_2-coated Zn (top right). Galvanostatic cycling results for pristine and TiO_2-coated Zn at 1mAh cm^{-2} (bottom). (a-b) Reprinted with permission.[106] Copyright 2018, Wiley-VCH.

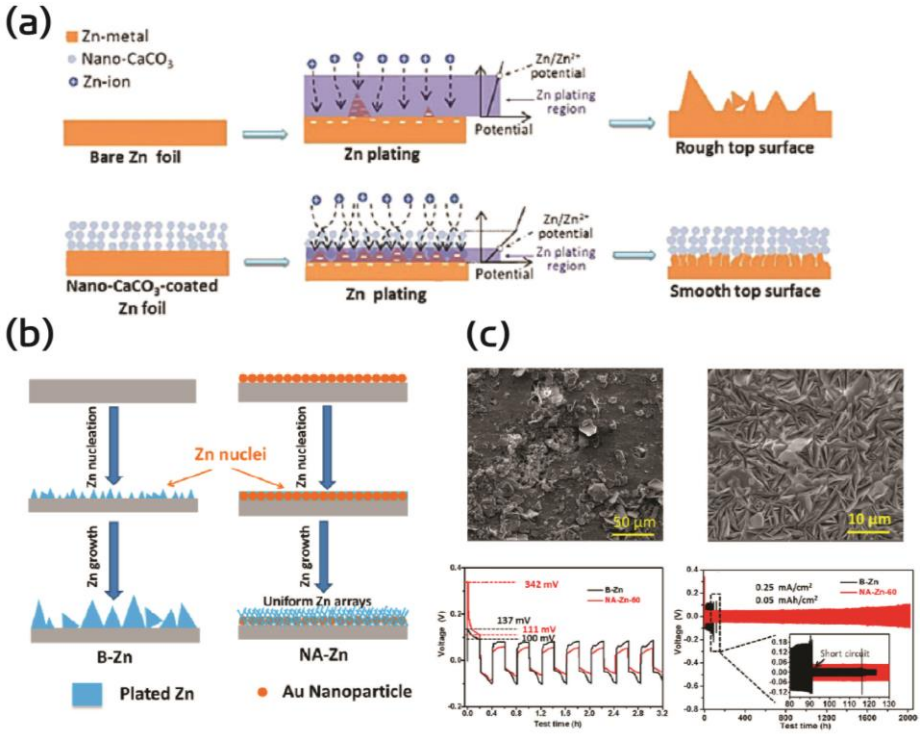

Figure 3-6. (a) A schematic illustration of the effects of $CaCO_3$-coating on Zn plating. Reprinted with permission.[105] Copyright 2018, Wiley-VCH. (b) A schematic illustration of the expected difference in Zn plating behavior between bare (left) and Au-sputtered Zn (right). (c) SEM images of bare (top left) and Au-sputtered (top right) Zn electrodes for 2000 cycles at 0.5 A g^{-1} paired with a CNT/MnO_2 cathode. Initial galvanostatic voltage profiles of bare (black) and Au-sputtered (red) Zn electrodes showing a difference in initial nucleation overpotential (bottom left). Long-term cycling performance of symmetric Zn cells for bare (black) and Au-sputtered (red) Zn electrodes (bottom right). (b-c) Reprinted with permission.[100] Copyright 2019, American Chemical Society.

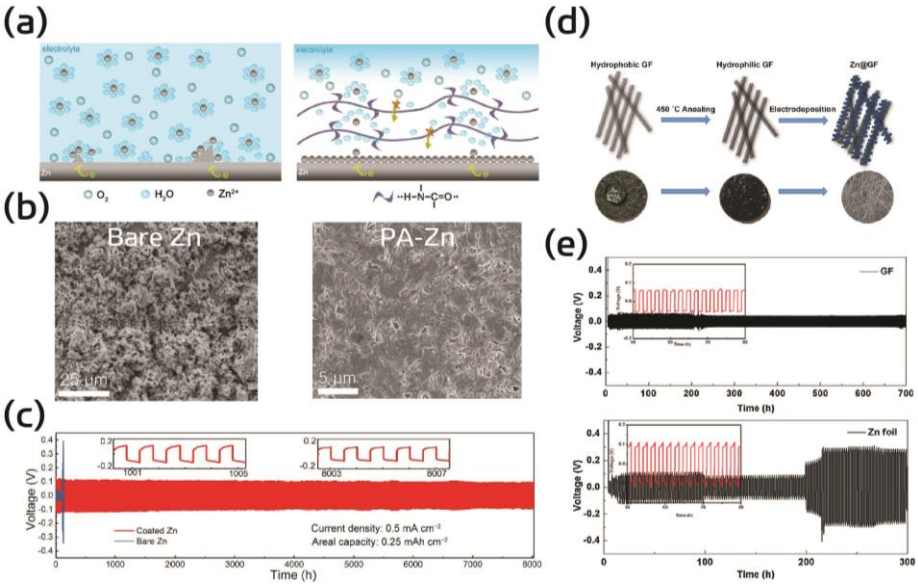

Figure 3-7. (a) A schematic illustration of Zn plating with bare (left) and PA-coated Zn (right). (b) SEM images of bare Zn (left) and PA-coated Zn (right) electroplated with Zn at a current density of 0.2 mA cm^{-2} (3.0 mAh cm^{-2}) on Ti foil. (c) Galvanostatic voltage profiles for bare Zn (blue) and PA-coated Zn (red) at a current density of 0.5 mA cm^{-2} (0.25 mAh cm^{-2}). (a–c) Reprinted with permission.[104] Copyright 2019, The Royal Society of Chemistry. (d) Experimental scheme for designing a Zn-graphite fiber host by means of annealing and electrodeposition. (e) Galvanostatic voltage profiles of a Zn symmetric cell with graphite fiber host anodes (top) and bare Zn foil (bottom). (d and e) Reprinted with permission.[108] Copyright 2017, Elsevier.

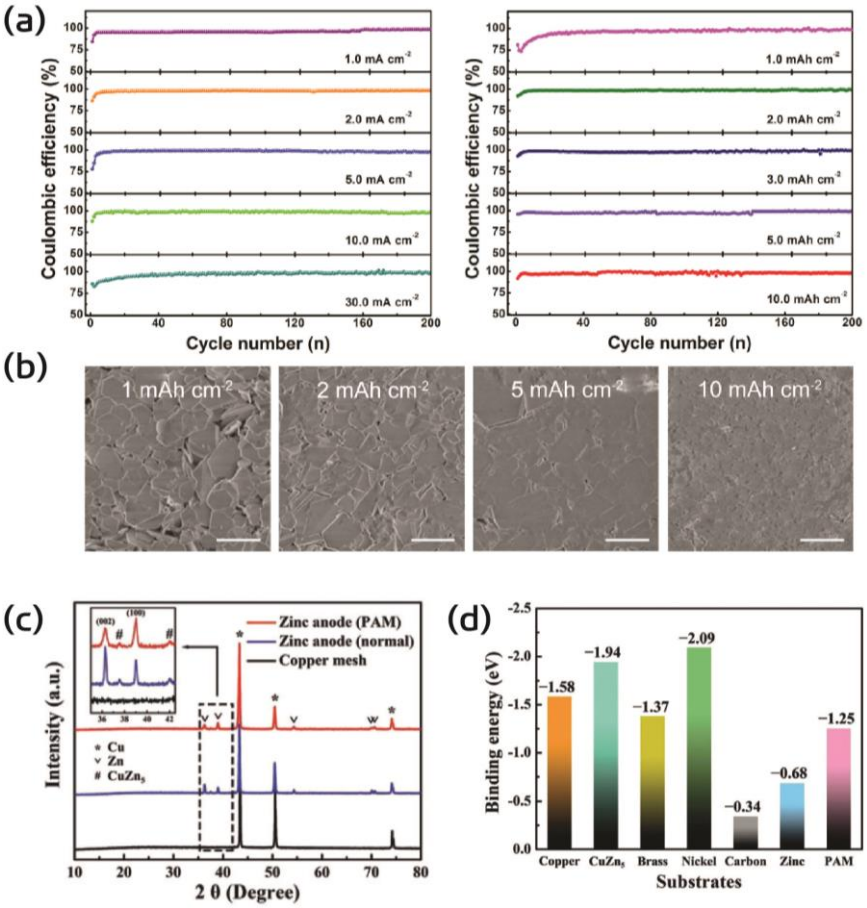

Figure 3-8. (a) Coulombic efficiency test results with annealed ZIF-8 host anodes and Cu foil at a fixed areal capacity of 1 mAh cm^{-2} (left) and a fixed current density of 20 mA cm^{-2} (right). (b) SEM images of Zn deposits at a current density of 1 mA cm^{-2} for different areal capacities. (a and b) Reprinted with permission.[109] Copyright 2019, Cell Press. (c) XRD results of synthesized host anodes (red: Zn-deposited Cu with the PAM additive, blue: Zn-deposited Cu, black: Cu mesh). (d) Calculated binding affinity between Zn and various materials. (c and d) Reprinted with permission.[91] Copyright 2019, Wiley-VCH.

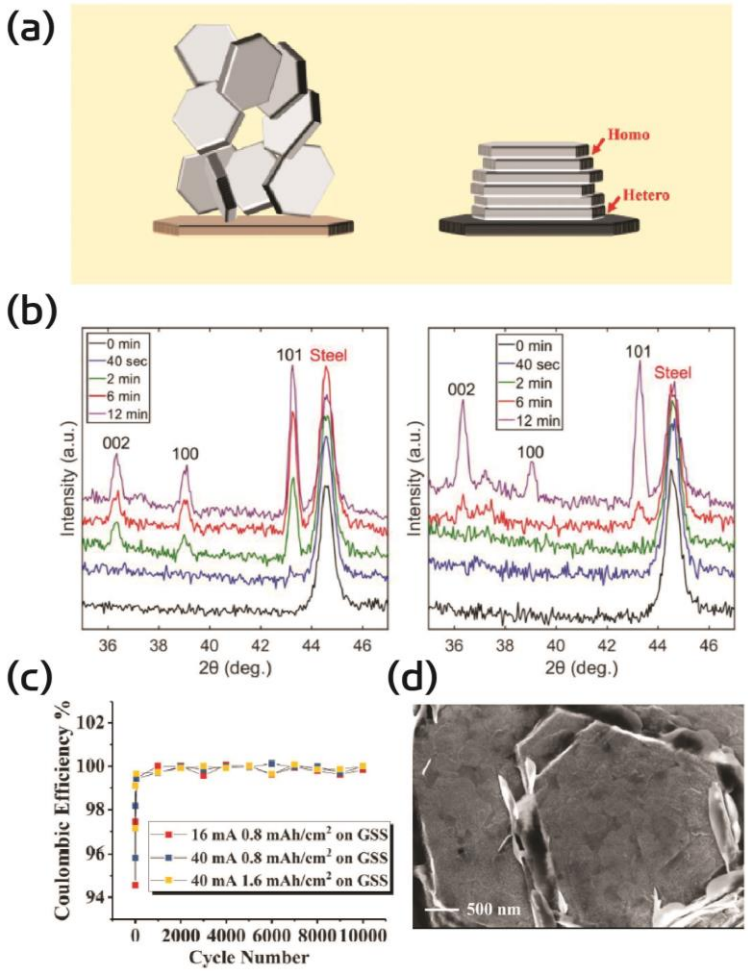

Figure 3-9. (a) A schematic illustration of the design principle for epitaxial metal electrodeposition. (b) Grazing incident XRD (GIXRD) of Zn electrodeposited on bare (left) and graphene-coated (right) stainless steel. (c) Coulombic efficiency levels at high current densities on epitaxially grown anodes. (d) SEM image of homoepitaxially deposited Zn on graphene-steel for 12 min. at a current density of 4 mA cm^{-2}. (e–h) Reprinted with permission.[111] Copyright 2019, American Association for the Advancement of Science.

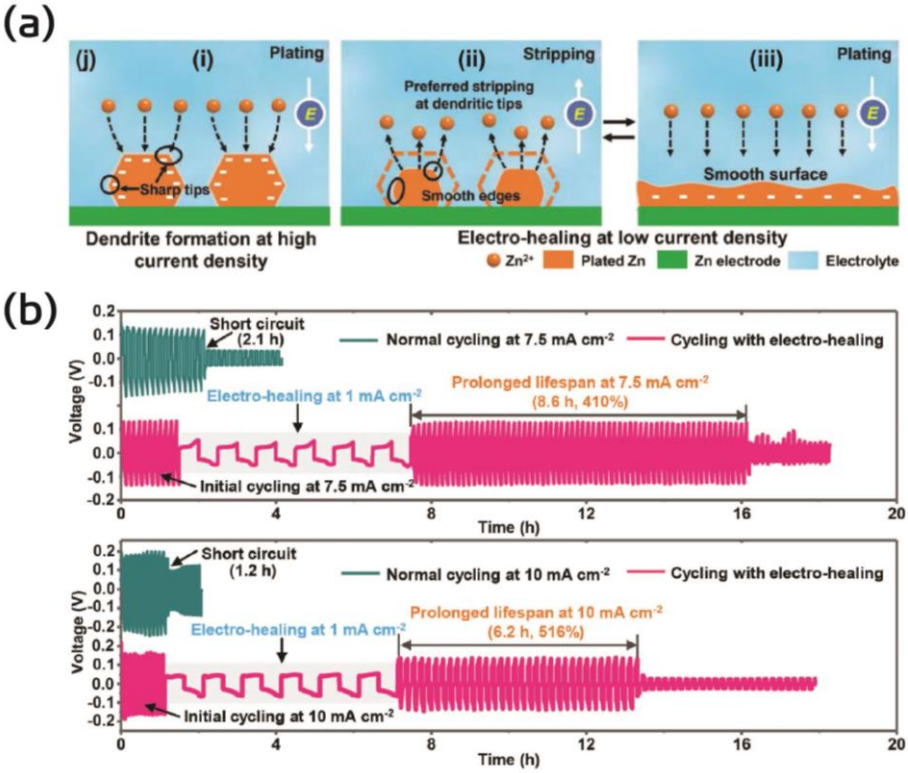

Figure 3-10. (a) A schematic illustration of the "electro-healing" strategy. (b) Galvanostatic voltage profiles of Zn symmetric cells with (magenta) and without (dark green) a healing step at different current densities (top: 7.5 mA cm^{-2}, bottom: 10 mA cm^{-2}). Reprinted with permission.[112] Copyright 2019, Wiley-VCH.

Cathode	Avg. V (vs. Zn)	Avg. Q (mAh g^{-1})	Current density (A g^{-1})	Mass loading (mg cm^{-2})	Theoretical Zn (mg)	ED theoretical (Wh kg^{-1})	ED 50μm-Zn (Wh kg^{-1})	ED 250μm-Zn (Wh kg^{-1})	Ref.
$Zn_{0.25}V_2O_5 \cdot nH_2O$	0.81	282	0.3	6.0	2.334	170	33.1	7.31	[7a]
$ZnMn_2O_4$	1.35	150	0.05	1.08	0.4794	167	10.8	2.21	[28b]
α-MnO_2	1.44	260	0.308	3.0	1.076	284	29.2	6.09	[28c]
$Na_2V_6O_{16} \cdot 3H_2O$	0.80	341	0.5	2.653	1.248	193	19.01	3.929	[7d]
Mn-VO_x	0.75	371	0.5	3.5	1.792	192	25.03	5.26	[113]
δ-MnO_2 (birnessite)	1.5	350	0.1	2.0	0.9675	368	28.07	5.72	[7b]
$Zn_{0.3}V_2O_5 \cdot nH_2O$	0.80	426	0.2	2.0	1.176	224	18.22	3.714	[114]
ZnHCF	1.7	65	0.06	8.0	*anode: 0.7	102 (actual)			[30c]
$Na_{0.33}V_2O_5$	0.7	276	0.2	1.5	0.5712	144	7.85	1.584	[54]
$CoFe(CN)_6$	1.75	173	0.3	n/a assume 2.0	0.4774	250	16.19	3.30	[26]
VO_2 (B)	0.75	357	0.1	n/a assume 2.0	0.9851	187	14.31	2.918	[33]
$LiV_2(PO_4)_3$/C	1.3	42-stack pouch cell				156 (actual)			[32]
β-MnO_2	1.35	258	0.2	2.0	0.7119	265	18.6	3.8	[115]
δ-MnO_{2-x}	1.5	345	0.2	1.0	0.421	364	12.6	2.51	[116]
$NaCa_{0.6}V_6O_{16} \cdot nH_2O$	0.75	347	0.1	1.1	0.5266	183	7.84	1.57	[117]
$Cu_3(HHTP)_2$	0.80	191	0.1	2.0	0.528	124	8.17	1.665	[118]
$MnO_2H_{0.16}$ -$(H_2O)_{0.27}$	1.35	236	0.1	2.5	0.814	247	21.01	4.329	[119]
p-chloranil	1.1	170	0.0434	2.4	0.563	155	11.87	2.44	[55]
Li-$V_2O_5 \cdot nH_2O$	0.7	470	0.5	0.735	0.477	209	6.69	1.327	[38]
PANI-MnO_2	1.5	280	0.2	2.0	0.7726	313	22.5	4.58	[120]
Calix[4]Quinone	1.0	335	0.02	2.5	1.156	238	22.1	4.55	[121]
$H_2V_3O_8$	0.7	400	0.1	1.2	0.6623	188	9.18	1.84	[122]
V_6O_{13}	0.7	360	0.2	1.25	0.6209	175	8.59	1.72	[7c]
$Mg_xV_2O_5 \cdot nH_2O$	0.7	330	0.1	4.2	1.912	165	24.50	5.225	[123]
V_2O_5	0.72	460	0.5	2.0	1.269	212	17.7	3.61	[124]

Table 3-1. Energy density calculations for recently reported AZIB cathodes for various amounts of Zn

* The anode mass loading is balanced with the cathode by using Zn powder instead of foil.

Coulombic Efficiency (%)	% Zn after 50 cycles	% Zn after 100 cycles	% Zn after 500 cycles	% Zn after 1,000 cycles	% Zn after 10,000 cycles
90	0.57	0	0	0	0
92	1.68	0.03	0	0	0
95	8.10	0.62	0	0	0
98	37.2	13.5	0	0	0
99	61.1	37.0	0.66	0	0
99.5	78.2	60.9	8.20	0.67	0
99.9	95.2	90.6	60.7	36.8	0
99.99	99.5	99.0	95.1	90.5	36.8

Table 3-2. Calculations for remaining weight percentage of Zn after 50 – 10,000 cycles for different Coulombic efficiencies.

4. Summary and Conclusions

As with any type of battery chemistry, AZIBs require a multi-faceted approach for optimal performance. The main bottlenecks in this field are identified as the cathode and the Zn anode. Accordingly, this dissertation is composed of three sections: i) a general overview of ARBs, ii) hydrated intercalation for high performance AZIB cathodes, and iii) a detailed discussion on the importance of Zn metal anodes. Chapter 1 provides socio-technological context for ARBs, identifying their current position within the framework of today's battery portfolio and opportunities for commercial applications. Chapter 2 elaborates on cathode-oriented research, where the electrochemistry and structural dynamics of V_6O_{13} are investigated with various tools to elucidate the effect of water during (de)intercalation. Results point to the critical role of hydrated intercalation, verified by (electro)chemical, spectroscopic, and simulated data. Chapter 3 is focused on the Zn anode, the importance of which cannot be over-emphasized for practical applications. This section is dedicated to discussing the merits and plating/stripping mechanisms of Zn in aqueous settings, various strategies that tackle the hurdles for enhancing the reversibility of Zn, energy density dependence on initial Zn loading and its Coulombic efficiency.

AZIBs are currently faced with the daunting challenge of being compared to existing systems such as LIBs. However, the growing need for diverse energy storage solutions calls for a wide spectrum of research initiatives

in addition to well-established ones. In particular, as AZIBs show promise for grid-scale energy storage applications such as ESSs, strategies should be formulated in such a way that they target the needs of this market, some of which are safety, long cycle life (maintenance costs), reasonable energy density, and high rate capability. High performance Zn anodes are key to satisfying such needs, as shown by the critical impact of efficiency and weight on cycle life and energy density. Therefore, considering the commercial value of AZIBs, future research should be directed towards this path along with more in-depth studies of viable cathode candidates. In time, such an integrated approach will advance AZIBs to the border between academia and industry, propelling their potential commercialization based on a long history of experience with primary Zn batteries, pre-established manufacturing processes, and know-how of the current rechargeable battery industry.

5. Bibliography

[1] a) R. Demir-Cakan, M. R. Palacin, L. Croguennec, *J. Mater. Chem. A* **2019**, 7, 20519; b) H. Kim, J. Hong, K.-Y. Park, H. Kim, S.-W. Kim, K. Kang, *Chem. Rev.* **2014**, 114, 11788; c) W. Tang, Y. Zhu, Y. Hou, L. Liu, Y. Wu, K. P. Loh, H. Zhang, K. Zhu, *Energy Environ. Sci.* **2013**, 6, 2093.

[2] J. Shin, J. Lee, Y. Park, J. W. Choi, *Chem. Sci.* **2020**, 11, 2028.

[3] a) P. Byeon, H. B. Bae, H.-S. Chung, S.-G. Lee, J.-G. Kim, H. J. Lee, J. W. Choi, S.-Y. Chung, *Adv. Funct. Mater.* **2018**, 28, 1804564; b) P. Byeon, H. J. Lee, J. W. Choi, S.-Y. Chung, *ChemSusChem* **2019**, 12, 787; c) H. J. Lee, J. H. Lee, I. H. Son, S. Han, P. Byeon, M.-S. Park, S.-Y. Chung, J. W. Choi, *ACS Appl. Energy Mater.* **2018**, 1, 5726; d) J.-Y. Luo, W.-J. Cui, P. He, Y.-Y. Xia, *Nat. Chem.* **2010**, 2, 760; e) J.-Y. Luo, Y.-Y. Xia, *Adv. Funct. Mater.* **2007**, 17, 3877.

[4] a) Z. Li, D. Young, K. Xiang, W. C. Carter, Y.-M. Chiang, *Adv. Energy Mater.* **2013**, 3, 290; b) L. Suo, O. Borodin, Y. Wang, X. Rong, W. Sun, X. Fan, S. Xu, M. A. Schroeder, A. V. Cresce, F. Wang, C. Yang, Y.-S. Hu, K. Xu, C. Wang, *Adv. Energy Mater.* **2017**, 7, 1701189; c) Y. Wang, J. Liu, B. Lee, R. Qiao, Z. Yang, S. Xu, X. Yu, L. Gu, Y.-S. Hu, W. Yang, K. Kang, H. Li, X.-Q. Yang, L. Chen, X. Huang, *Nat. Commun.* **2015**, 6, 6401.

[5] a) M. Pasta, C. D. Wessells, R. A. Huggins, Y. Cui, *Nat. Commun.* **2012**, 3, 1149; b) D. Su, A. McDonagh, S.-Z. Qiao, G. Wang, *Adv. Mater.* **2017**, 29, 1604007.

[6] K. W. Nam, S. Kim, S. Lee, M. Salama, I. Shterenberg, Y. Gofer, J.-S. Kim, E. Yang, C. S. Park, J.-S. Kim, S.-S. Lee, W.-S. Chang, S.-G. Doo, Y. N. Jo, Y. Jung, D. Aurbach, J. W. Choi, *Nano Lett.* **2015**, 15, 4071.

[7] a) D. Kundu, B. D. Adams, V. Duffort, S. H. Vajargah, L. F. Nazar, *Nat. Energy* **2016**, 1, 16119; b) K. W. Nam, H. Kim, J. H. Choi, J. W. Choi, *Energy Environ. Sci.* **2019**, 12, 1999; c) J. Shin, D. S. Choi, H. J. Lee, Y. Jung, J. W. Choi, *Adv. Energy Mater.* **2019**, 9, 1900083; d) V. Soundharrajan, B. Sambandam, S. Kim, M. H. Alfaruqi, D. Y. Putro, J. Jo, S. Kim, V. Mathew, Y.-K. Sun, J. Kim, *Nano Lett.* **2018**, 18, 2402; e) C. Xia, J. Guo, P. Li, X. Zhang, H. N. Alshareef, *Angew. Chem. Int. Ed.* **2018**, 57, 3943; f) M. Yan, P. He, Y. Chen, S. Wang, Q. Wei, K. Zhao, X. Xu, Q. An, Y. Shuang, Y. Shao, K. T. Mueller, L. Mai, J. Liu, J. Yang, *Adv. Mater.* **2018**, 30, 1703725.

[8] J. H. Lee, H. J. Lee, S. H. Choi, J. Shin, S.-Y. Chung, J. W. Choi, *Adv. Energy Mater.* **2018**, 8, 1703572.

[9] a) X. Wu, J. J. Hong, W. Shin, L. Ma, T. Liu, X. Bi, Y. Yuan, Y. Qi, T. W. Surta, W. Huang, J. Neuefeind, T. Wu, P. A. Greaney, J. Lu, X. Ji, *Nat. Energy* **2019**, 4, 123; b) Q. Zhao, L. Liu, J. Yin, J. Zheng, D. Zhang,

J. Chen, L. A. Archer, *Angew. Chem. Int. Ed.* **2020**, 59, 3048.

[10] a) P. Hu, M. Yan, T. Zhu, X. Wang, X. Wei, J. Li, L. Zhou, Z. Li, L. Chen, L. Mai, *ACS Appl. Mater. Interfaces* **2017**, 9, 42717; b) J. Yan, J. Wang, H. Liu, Z. Bakenov, D. Gosselink, P. Chen, *J. Power Sources* **2012**, 216, 222; c) H. B. Zhao, C. J. Hu, H. W. Cheng, J. H. Fang, Y. P. Xie, W. Y. Fang, T. N. L. Doan, T. K. A. Hoang, J. Q. Xu, P. Chen, *Sci. Rep.* **2016**, 6, 25809.

[11] P. Kurzweil, *J. Power Sources* **2010**, 195, 4424.

[12] a) G. J. May, A. Davidson, B. Monahov, *J. Energy Storage* **2018**, 15, 145; b) D. Pavlov, in *Lead-Acid Batteries: Science and Technology (2nd Edition)*, DOI: https://doi.org/10.1016/B978-0-444-59552-2.00001-8 (Ed: D. Pavlov), Elsevier, Amsterdam **2017**, p. 3.

[13] B. Scrosati, *J. Solid State Electrochem.* **2011**, 15, 1623.

[14] M. Sugiyama, K. Fujii, S. Nakamura, *Solar to Chemical Energy Conversion: Theory and Application*, Springer International Publishing, **2016**.

[15] M. S. Whittingham, *Science* **1976**, 192, 1126.

[16] K. Mizushima, P. C. Jones, P. J. Wiseman, J. B. Goodenough, *Mater. Res. Bull* **1980**, 15, 783.

[17] A. Yoshino, K. Sanechika, T. Nakajima, **1987**, US4668595A.

[18] W. Li, J. R. Dahn, D. S. Wainwright, *Science* **1994**, 264, 1115.

[19] a) G. Fang, J. Zhou, A. Pan, S. Liang, *ACS Energy Lett.* **2018**, 3, 2480;

b) A. Konarov, N. Voronina, J. H. Jo, Z. Bakenov, Y.-K. Sun, S.-T. Myung, *ACS Energy Lett.* **2018**, 3, 2620; c) L. E. Blanc, D. Kundu, L. F. Nazar, *Joule* **2020**, 4, 771; d) H. Ao, Y. Zhao, J. Zhou, W. Cai, X. Zhang, Y. Zhu, Y. Qian, *J. Mater. Chem. A* **2019**, 7, 18708.

[20] J. B. Goodenough, Y. Kim, *Chem. Mater.* **2010**, 22, 587.

[21] A. Wang, S. Kadam, H. Li, S. Shi, Y. Qi, *Npj Comput. Mater.* **2018**, 4, 15.

[22] a) G. Wang, L. Fu, N. Zhao, L. Yang, Y. Wu, H. Wu, *Angew. Chem. Int. Ed.* **2007**, 46, 295; b) V. S. Nair, Y. L. Cheah, S. Madhavi, *J. Electrochem. Soc.* **2013**, 161, A256; c) Y.-g. Wang, Y.-y. Xia, *J. Electrochem. Soc.* **2006**, 153, A450; d) H. Qin, Z. P. Song, H. Zhan, Y. H. Zhou, *J. Power Sources* **2014**, 249, 367; e) D. Zhou, S. Liu, H. Wang, G. Yan, *J. Power Sources* **2013**, 227, 111; f) H. Manjunatha, T. V. Venkatesha, G. S. Suresh, *J. Solid State Electrochem.* **2012**, 16, 1941.

[23] L. Suo, O. Borodin, T. Gao, M. Olguin, J. Ho, X. Fan, C. Luo, C. Wang, K. Xu, *Science* **2015**, 350, 938.

[24] a) L. Chen, J. Zhang, Q. Li, J. Vatamanu, X. Ji, T. P. Pollard, C. Cui, S. Hou, J. Chen, C. Yang, L. Ma, M. S. Ding, M. Garaga, S. Greenbaum, H.-S. Lee, O. Borodin, K. Xu, C. Wang, *ACS Energy Lett.* **2020**, 5, 968; b) F. Wang, L. Suo, Y. Liang, C. Yang, F. Han, T. Gao, W. Sun, C. Wang, *Adv. Energy Mater.* **2017**, 7, 1600922; c) L. Suo, O. Borodin, W. Sun, X. Fan, C. Yang, F. Wang, T. Gao, Z. Ma, M. Schroeder, A.

von Cresce, S. M. Russell, M. Armand, A. Angell, K. Xu, C. Wang, *Angew. Chem. Int. Ed.* **2016**, 55, 7136; d) J. Zheng, G. Tan, P. Shan, T. Liu, J. Hu, Y. Feng, L. Yang, M. Zhang, Z. Chen, Y. Lin, J. Lu, J. C. Neuefeind, Y. Ren, K. Amine, L.-W. Wang, K. Xu, F. Pan, *Chem* **2018**, 4, 2872; e) F. Wang, Y. Lin, L. Suo, X. Fan, T. Gao, C. Yang, F. Han, Y. Qi, K. Xu, C. Wang, *Energy Environ. Sci.* **2016**, 9, 3666; f) L. Suo, D. Oh, Y. Lin, Z. Zhuo, O. Borodin, T. Gao, F. Wang, A. Kushima, Z. Wang, H.-C. Kim, Y. Qi, W. Yang, F. Pan, J. Li, K. Xu, C. Wang, *J. Am. Chem. Soc.* **2017**, 139, 18670; g) L. Suo, F. Han, X. Fan, H. Liu, K. Xu, C. Wang, *J. Mater. Chem. A* **2016**, 4, 6639; h) F. Wang, O. Borodin, M. S. Ding, M. Gobet, J. Vatamanu, X. Fan, T. Gao, N. Eidson, Y. Liang, W. Sun, S. Greenbaum, K. Xu, C. Wang, *Joule* **2018**, 2, 927; i) C. Yang, J. Chen, T. Qing, X. Fan, W. Sun, A. von Cresce, M. S. Ding, O. Borodin, J. Vatamanu, M. A. Schroeder, N. Eidson, C. Wang, K. Xu, *Joule* **2017**, 1, 122; j) Y. Yamada, K. Usui, K. Sodeyama, S. Ko, Y. Tateyama, A. Yamada, *Nat. Energy* **2016**, 1, 16129; k) C. Yang, J. Chen, X. Ji, T. P. Pollard, X. Lü, C.-J. Sun, S. Hou, Q. Liu, C. Liu, T. Qing, Y. Wang, O. Borodin, Y. Ren, K. Xu, C. Wang, *Nature* **2019**, 569, 245.

[25] O. Borodin, J. Self, K. A. Persson, C. Wang, K. Xu, *Joule* **2020**, 4, 69.

[26] T. Yamamoto, T. Shoji, *Inorg. Chim. Acta* **1986**, 117, L27.

[27] C. Xu, B. Li, H. Du, F. Kang, *Angew. Chem. Int. Ed.* **2012**, 51, 933.

[28] a) W. Sun, F. Wang, S. Hou, C. Yang, X. Fan, Z. Ma, T. Gao, F. Han, R. Hu, M. Zhu, C. Wang, *J. Am. Chem. Soc.* **2017**, 139, 9775; b) N. Zhang, F. Cheng, Y. Liu, Q. Zhao, K. Lei, C. Chen, X. Liu, J. Chen, *J. Am. Chem. Soc.* **2016**, 138, 12894; c) H. Pan, Y. Shao, P. Yan, Y. Cheng, K. S. Han, Z. Nie, C. Wang, J. Yang, X. Li, P. Bhattacharya, K. T. Mueller, J. Liu, *Nat. Energy* **2016**, 1, 16039.

[29] a) P. Oberholzer, E. Tervoort, A. Bouzid, A. Pasquarello, D. Kundu, *ACS Appl. Mater. Interfaces* **2019**, 11, 674; b) P. He, M. Yan, G. Zhang, R. Sun, L. Chen, Q. An, L. Mai, *Adv. Energy Mater.* **2017**, 7, 1601920.

[30] a) Z. Liu, G. Pulletikurthi, F. Endres, *ACS Appl. Mater. Interfaces* **2016**, 8, 12158; b) D. J. Kim, Y. H. Jung, K. K. Bharathi, S. H. Je, D. K. Kim, A. Coskun, J. W. Choi, *Adv. Energy Mater.* **2014**, 4, 1400133; c) L. Zhang, L. Chen, X. Zhou, Z. Liu, *Adv. Energy Mater.* **2015**, 5, 1400930; d) R. Trócoli, F. La Mantia, *ChemSusChem* **2015**, 8, 481; e) V. Renman, D. O. Ojwang, M. Valvo, C. P. Gómez, T. Gustafsson, G. Svensson, *J. Power Sources* **2017**, 369, 146.

[31] Z. Li, X. Mu, Z. Zhao-Karger, T. Diemant, R. J. Behm, C. Kübel, M. Fichtner, *Nat. Commun.* **2018**, 9, 5115.

[32] F. Wang, E. Hu, W. Sun, T. Gao, X. Ji, X. Fan, F. Han, X.-Q. Yang, K. Xu, C. Wang, *Energy Environ. Sci.* **2018**, 11, 3168.

[33] J. Ding, Z. Du, L. Gu, B. Li, L. Wang, S. Wang, Y. Gong, S. Yang, *Adv. Mater.* **2018**, 30, 1800762.

[34] F. Wang, S. Xiao, Z. Chang, Y. Yang, Y. Wu, *ChemComm* **2013**, 49, 9209.

[35] M. Zhao, B. Zhang, G. Huang, H. Zhang, X. Song, *J. Power Sources* **2013**, 232, 181.

[36] Y. Wang, L. Mu, J. Liu, Z. Yang, X. Yu, L. Gu, Y.-S. Hu, H. Li, X.-Q. Yang, L. Chen, X. Huang, *Adv. Energy Mater.* **2015**, 5, 1501005.

[37] Y. Liu, Y. Qiao, W. Zhang, H. Xu, Z. Li, Y. Shen, L. Yuan, X. Hu, X. Dai, Y. Huang, *Nano Energy* **2014**, 5, 97.

[38] Y. Yang, Y. Tang, G. Fang, L. Shan, J. Guo, W. Zhang, C. Wang, L. Wang, J. Zhou, S. Liang, *Energy Environ. Sci.* **2018**, 11, 3157.

[39] F. Wang, O. Borodin, T. Gao, X. Fan, W. Sun, F. Han, A. Faraone, J. A. Dura, K. Xu, C. Wang, *Nat. Mater.* **2018**, 17, 543.

[40] H. Zhang, X. Wu, T. Yang, S. Liang, X. Yang, *ChemComm* **2013**, 49, 9977.

[41] F. Wang, Y. Liu, X. Wang, Z. Chang, Y. Wu, R. Holze, *ChemElectroChem* **2015**, 2, 1024.

[42] B. Zhang, Y. Liu, X. Wu, Y. Yang, Z. Chang, Z. Wen, Y. Wu, *ChemComm* **2014**, 50, 1209.

[43] S. Islam, M. H. Alfaruqi, D. Y. Putro, V. Mathew, S. Kim, J. Jo, S. Kim, Y.-K. Sun, K. Kim, J. Kim, *ChemSusChem* **2018**, 11, 2239.

[44] Z. Hou, X. Zhang, X. Li, Y. Zhu, J. Liang, Y. Qian, *J. Mater. Chem. A* **2017**, 5, 730.

[45] Q. Nian, S. Liu, J. Liu, Q. Zhang, J. Shi, C. Liu, R. Wang, Z. Tao, J. Chen, *ACS Appl. Energy Mater.* **2019**, 2, 4370.

[46] Y. Tao, C. Ding, D. Tan, F. Yu, F. Wang, *ChemSusChem* **2018**, 11, 4269.

[47] G. G. Yadav, J. Cho, D. Turney, B. Hawkins, X. Wei, J. Huang, S. Banerjee, M. Nyce, *Adv. Energy Mater.* **2019**, 9, 1902270.

[48] L. Ma, S. Chen, H. Li, Z. Ruan, Z. Tang, Z. Liu, Z. Wang, Y. Huang, Z. Pei, J. A. Zapien, C. Zhi, *Energy Environ. Sci.* **2018**, 11, 2521.

[49] L. Smith, B. Dunn, *Science* **2015**, 350, 918.

[50] a) Z. Rong, R. Malik, P. Canepa, G. Sai Gautam, M. Liu, A. Jain, K. Persson, G. Ceder, *Chem. Mater.* **2015**, 27, 6016; b) E. Levi, Y. Gofer, D. Aurbach, *Chem. Mater.* **2010**, 22, 860.

[51] a) B. Lee, H. R. Lee, H. Kim, K. Y. Chung, B. W. Cho, S. H. Oh, *ChemComm* **2015**, 51, 9265; b) B. Lee, H. R. Seo, H. R. Lee, C. S. Yoon, J. H. Kim, K. Y. Chung, B. W. Cho, S. H. Oh, *ChemSusChem* **2016**, 9, 2948.

[52] M. H. Alfaruqi, V. Mathew, J. Song, S. Kim, S. Islam, D. T. Pham, J. Jo, S. Kim, J. P. Baboo, Z. Xiu, K.-S. Lee, Y.-K. Sun, J. Kim, *Chem. Mater.* **2017**, 29, 1684.

[53] Q. Pang, C. Sun, Y. Yu, K. Zhao, Z. Zhang, P. M. Voyles, G. Chen, Y. Wei, X. Wang, *Adv. Energy Mater.* **2018**, 8, 1800144.

[54] P. He, G. Zhang, X. Liao, M. Yan, X. Xu, Q. An, J. Liu, L. Mai, *Adv.*

Energy Mater. **2018**, 8, 1702463.

[55] D. Kundu, P. Oberholzer, C. Glaros, A. Bouzid, E. Tervoort, A. Pasquarello, M. Niederberger, *Chem. Mater.* **2018**, 30, 3874.

[56] Z. Guo, Y. Ma, X. Dong, J. Huang, Y. Wang, Y. Xia, *Angew. Chem. Int. Ed.* **2018**, 57, 11737.

[57] W. Meng, R. Pigliapochi, P. M. Bayley, O. Pecher, M. W. Gaultois, I. D. Seymour, H.-P. Liang, W. Xu, K. M. Wiaderek, K. W. Chapman, C. P. Grey, *Chem. Mater*. **2017**, 29, 5513.

[58] a) Y.-L. Ding, Y. Wen, C. Wu, P. A. van Aken, J. Maier, Y. Yu, *Nano Lett.* **2015**, 15, 1388; b) K. West, B. Zachau-Christiansen, T. Jacobsen, S. Atlung, *J. Power Sources* **1985**, 14, 235; c) N. Xu, X. Ma, M. Wang, T. Qian, J. Liang, W. Yang, Y. Wang, J. Hu, C. Yan, *Electrochim. Acta* **2016**, 203, 171.

[59] T. Gustafsson, J. O. Thomas, R. Koksbang, G. C. Farrington, *Electrochim. Acta* **1992**, 37, 1639.

[60] M. Giorgetti, *J. Electrochem. Soc.* **1999**, 146, 2387.

[61] P. E. Stallworth, S. Kostov, M. L. denBoer, S. G. Greenbaum, C. Lampe-Onnerud, *J. Appl. Phys.* **1998**, 83, 1247.

[62] a) J. Lim, Y. Li, D. H. Alsem, H. So, S. C. Lee, P. Bai, D. A. Cogswell, X. Liu, N. Jin, Y.-s. Yu, N. J. Salmon, D. A. Shapiro, M. Z. Bazant, T. Tyliszczak, W. C. Chueh, *Science* **2016**, 353, 566; b) H. Liu, F. C. Strobridge, O. J. Borkiewicz, K. M. Wiaderek, K. W. Chapman, P. J.

Chupas, C. P. Grey, *Science* **2014**, 344, 1252817.

[63] K. H. Xue, *J. Electrochem. Soc.* **1993**, 140, 3413.

[64] a) H. J. Lee, J. Shin, J. W. Choi, *Adv. Mater.* **2018**, 30, 1705851; b) Y. Mizuno, M. Okubo, E. Hosono, T. Kudo, H. Zhou, K. Oh-ishi, *J. Phys. Chem. C* **2013**, 117, 10877; c) Y. Mizuno, M. Okubo, E. Hosono, T. Kudo, K. Oh-ishi, A. Okazawa, N. Kojima, R. Kurono, S.-i. Nishimura, A. Yamada, *J. Mater. Chem. A* **2013**, 1, 13055; d) D. Kundu, S. Hosseini Vajargah, L. Wan, B. Adams, D. Prendergast, L. F. Nazar, *Energy Environ. Sci.* **2018**, 11, 881; e) K. W. Nam, S. Kim, E. Yang, Y. Jung, E. Levi, D. Aurbach, J. W. Choi, *Chem. Mater.* **2015**, 27, 3721; f) S. Kim, K. W. Nam, S. Lee, W. Cho, J.-S. Kim, B. G. Kim, Y. Oshima, J.-S. Kim, S.-G. Doo, H. Chang, D. Aurbach, J. W. Choi, *Angew. Chem. Int. Ed.* **2015**, 54, 15094; g) S. Kim, S. Lee, K. W. Nam, J. Shin, S. Y. Lim, W. Cho, K. Suzuki, Y. Oshima, M. Hirayama, R. Kanno, J. W. Choi, *Chem. Mater.* **2016**, 28, 5488.

[65] S. Y. Lim, J. H. Lee, S. Kim, J. Shin, W. Choi, K. Y. Chung, D. S. Jung, J. W. Choi, *ACS Energy Lett.* **2017**, 2, 998.

[66] M. Rastgoo-Deylami, M. S. Chae, S.-T. Hong, *Chem. Mater.* **2018**, 30, 7464.

[67] J. Spencer Braithwaite, C. R. A. Catlow, J. H. Harding, J. D. Gale, *Phys. Chem. Chem. Phys.* **2001**, 3, 4052.

[68] B. Ravel, M. Newville, *J. Synchrotron Radiat.* **2005**, 12, 537.

[69] J. Filik, A. W. Ashton, P. C. Y. Chang, P. A. Chater, S. J. Day, M. Drakopoulos, M. W. Gerring, M. L. Hart, O. V. Magdysyuk, S. Michalik, A. Smith, C. C. Tang, N. J. Terrill, M. T. Wharmby, H. Wilhelm, *J. Appl. Crystallogr.* **2017**, 50, 959.

[70] G. Kresse, J. Furthmüller, *Comput. Mater. Sci.* **1996**, 6, 15.

[71] a) S. Grimme, J. Antony, S. Ehrlich, H. Krieg, *J. Chem. Phys.* **2010**, 132, 154104; b) J. P. Perdew, K. Burke, M. Ernzerhof, *Phys. Rev. Lett.* **1996**, 77, 3865; c) P. E. Blöchl, *Phys. Rev. B* **1994**, 50, 17953.

[72] L. Wang, T. Maxisch, G. Ceder, *Phys. Rev. B* **2006**, 73, 195107.

[73] H. J. Monkhorst, J. D. Pack, *Phys. Rev. B.* **1976**, 13, 5188.

[74] a) D. Sheppard, P. Xiao, W. Chemelewski, D. D. Johnson, G. Henkelman, *J. Chem. Phys.* **2012**, 136, 074103; b) D. Sheppard, G. Henkelman, *J. Comput. Chem.* **2011**, 32, 1769.

[75] A. Urban, D.-H. Seo, G. Ceder, *Npj Comput. Mater.* **2016**, 2, 16002.

[76] a) D. Prendergast, J. C. Grossman, G. Galli, *J. Chem. Phys.* **2005**, 123, 014501; b) M. W. Mahoney, W. L. Jorgensen, *J. Chem. Phys.* **2000**, 112, 8910.

[77] A. Y. Toukmaji, J. A. Board, *Comput. Phys. Commun.* **1996**, 95, 73.

[78] a) R. Wang, C.-C. Chung, Y. Liu, J. L. Jones, V. Augustyn, *Langmuir* **2017**, 33, 9314; b) V. Augustyn, Y. Gogotsi, *Joule* **2017**, 1, 443; c) R. Wang, J. B. Mitchell, Q. Gao, W.-Y. Tsai, S. Boyd, M. Pharr, N. Balke, V. Augustyn, *ACS Nano* **2018**, 12, 6032.

[79] M. Song, H. Tan, D. Chao, H. J. Fan, *Adv. Funct. Mater.* **2018**, 28, 1802564.

[80] X. G. Zhang, *Corrosion and Electrochemistry of Zinc*, Springer, **1996**.

[81] B. Beverskog, I. Puigdomenech, *Corros. Sci.* **1997**, 39, 107.

[82] J. Fu, Z. P. Cano, M. G. Park, A. Yu, M. Fowler, Z. Chen, *Adv. Mater.* **2017**, 29, 1604685.

[83] a) Y. Li, H. Dai, *Chem. Soc. Rev.* **2014**, 43, 5257; b) F. R. McLarnon, E. J. Cairns, *J. Electrochem. Soc.* **1991**, 138, 645; c) T. H. Wu, Y. Zhang, Z. D. Althouse, N. Liu, *Mater. Today Nano* **2019**, 6, 100032.

[84] B. Tang, L. Shan, S. Liang, J. Zhou, *Energy Environ. Sci.* **2019**, 12, 3288.

[85] J. F. Parker, C. N. Chervin, I. R. Pala, M. Machler, M. F. Burz, J. W. Long, D. R. Rolison, *Science* **2017**, 356, 415.

[86] K. Wippermann, J. W. Schultze, R. Kessel, J. Penninger, *Corros. Sci.* **1991**, 32, 205.

[87] a) C. Fang, J. Li, M. Zhang, Y. Zhang, F. Yang, J. Z. Lee, M.-H. Lee, J. Alvarado, M. A. Schroeder, Y. Yang, B. Lu, N. Williams, M. Ceja, L. Yang, M. Cai, J. Gu, K. Xu, X. Wang, Y. S. Meng, *Nature* **2019**, 572, 511; b) D.-J. Yoo, K. J. Kim, J. W. Choi, *Adv. Energy Mater.* **2018**, 8, 1702744; c) D.-J. Yoo, S. Yang, Y. S. Yun, J. H. Choi, D. Yoo, K. J. Kim, J. W. Choi, *Adv. Energy Mater.* **2018**, 8, 1802365.

[88] D. Lin, Y. Liu, Y. Cui, *Nat. Nanotechnol.* **2017**, 12, 194.

[89] J. Zhou, L. Shan, Z. Wu, X. Guo, G. Fang, S. Liang, *ChemComm* **2018**, 54, 4457.

[90] A. Naveed, H. Yang, J. Yang, Y. Nuli, J. Wang, *Angew. Chem. Int. Ed.* **2019**, 58, 2760.

[91] Q. Zhang, J. Luan, L. Fu, S. Wu, Y. Tang, X. Ji, H. Wang, *Angew. Chem. Int. Ed.* **2019**, 58, 15841.

[92] A. Bani Hashemi, G. Kasiri, F. La Mantia, *Electrochim. Acta* **2017**, 258, 703.

[93] Z. Liu, T. Cui, G. Pulletikurthi, A. Lahiri, T. Carstens, M. Olschewski, F. Endres, *Angew. Chem. Int. Ed.* **2016**, 55, 2889.

[94] J. Hao, J. Long, B. Li, X. Li, S. Zhang, F. Yang, X. Zeng, Z. Yang, W. K. Pang, Z. Guo, *Adv. Funct. Mater.* **2019**, 29, 1903605.

[95] L. Wang, Y. Zhang, H. Hu, H.-Y. Shi, Y. Song, D. Guo, X.-X. Liu, X. Sun, *ACS Appl. Mater. Interfaces* **2019**, 11, 42000.

[96] H. Qiu, X. Du, J. Zhao, Y. Wang, J. Ju, Z. Chen, Z. Hu, D. Yan, X. Zhou, G. Cui, *Nat. Commun.* **2019**, 10, 5374.

[97] C. Zhang, J. Holoubek, X. Wu, A. Daniyar, L. Zhu, C. Chen, D. P. Leonard, I. A. Rodríguez-Pérez, J.-X. Jiang, C. Fang, X. Ji, *ChemComm* **2018**, 54, 14097.

[98] H. Glatz, E. Tervoort, D. Kundu, *ACS Appl. Mater. Interfaces* **2020**, 12, 3522.

[99] C. W. Bock, A. K. Katz, J. P. Glusker, *J. Am. Chem. Soc.* **1995**, 117,

3754.

[100] M. Cui, Y. Xiao, L. Kang, W. Du, Y. Gao, X. Sun, Y. Zhou, X. Li, H. Li, F. Jiang, C. Zhi, *ACS Appl. Energy Mater.* **2019**, 2, 6490.

[101] H. Li, C. Xu, C. Han, Y. Chen, C. Wei, B. Li, F. Kang, *J. Electrochem. Soc.* **2015**, 162, A1439.

[102] M. Li, Q. He, Z. Li, Q. Li, Y. Zhang, J. Meng, X. Liu, S. Li, B. Wu, L. Chen, Z. Liu, W. Luo, C. Han, L. Mai, *Adv. Energy Mater.* **2019**, 9, 1901469.

[103] A. Xia, X. Pu, Y. Tao, H. Liu, Y. Wang, *Appl. Surf. Sci.* **2019**, 481, 852.

[104] Z. Zhao, J. Zhao, Z. Hu, J. Li, J. Li, Y. Zhang, C. Wang, G. Cui, *Energy Environ. Sci.* **2019**, 12, 1938.

[105] L. Kang, M. Cui, F. Jiang, Y. Gao, H. Luo, J. Liu, W. Liang, C. Zhi, *Adv. Energy Mater.* **2018**, 8, 1801090.

[106] K. Zhao, C. Wang, Y. Yu, M. Yan, Q. Wei, P. He, Y. Dong, Z. Zhang, X. Wang, L. Mai, *Adv. Mater. Interfaces* **2018**, 5, 1800848.

[107] X. Xie, S. Liang, J. Gao, S. Guo, J. Guo, C. Wang, G. Xu, X. Wu, G. Chen, J. Zhou, *Energy Environ. Sci.* **2020**, DOI: 10.1039/C9EE03545A.

[108] L.-P. Wang, N.-W. Li, T.-S. Wang, Y.-X. Yin, Y.-G. Guo, C.-R. Wang, *Electrochim. Acta* **2017**, 244, 172.

[109] Z. Wang, J. Huang, Z. Guo, X. Dong, Y. Liu, Y. Wang, Y. Xia, *Joule* **2019**, 3, 1289.

[110] a) Z. Kang, C. Wu, L. Dong, W. Liu, J. Mou, J. Zhang, Z. Chang, B.

Jiang, G. Wang, F. Kang, C. Xu, *ACS Sustain. Chem. Eng.* **2019**, 7, 3364; b) C. Li, X. Shi, S. Liang, X. Ma, M. Han, X. Wu, J. Zhou, *Chem. Eng. J.* **2020**, 379, 122248.

[111] J. Zheng, Q. Zhao, T. Tang, J. Yin, C. D. Quilty, G. D. Renderos, X. Liu, Y. Deng, L. Wang, D. C. Bock, C. Jaye, D. Zhang, E. S. Takeuchi, K. J. Takeuchi, A. C. Marschilok, L. A. Archer, *Science* **2019**, 366, 645.

[112] Q. Yang, G. Liang, Y. Guo, Z. Liu, B. Yan, D. Wang, Z. Huang, X. Li, J. Fan, C. Zhi, *Adv. Mater.* **2019**, 31, 1903778.

[113] C. Liu, Z. Neale, J. Zheng, X. Jia, J. Huang, M. Yan, M. Tian, M. Wang, J. Yang, G. Cao, *Energy Environ. Sci.* **2019**, 12, 2273.

[114] L. Wang, K.-W. Huang, J. Chen, J. Zheng, *Sci. Adv.* **2019**, 5, eaax4279.

[115] N. Zhang, F. Cheng, J. Liu, L. Wang, X. Long, X. Liu, F. Li, J. Chen, *Nat. Commun.* **2017**, 8, 405.

[116] T. Xiong, Z. G. Yu, H. Wu, Y. Du, Q. Xie, J. Chen, Y.-W. Zhang, S. J. Pennycook, W. S. V. Lee, J. Xue, *Adv. Energy Mater.* **2019**, 9, 1803815.

[117] K. Zhu, T. Wu, K. Huang, *Adv. Energy Mater.* **2019**, 9, 1901968.

[118] K. W. Nam, S. S. Park, R. dos Reis, V. P. Dravid, H. Kim, C. A. Mirkin, J. F. Stoddart, *Nat. Commun.* **2019**, 10, 4948.

[119] Q. Zhao, X. Chen, Z. Wang, L. Yang, R. Qin, J. Yang, Y. Song, S. Ding, M. Weng, W. Huang, J. Liu, W. Zhao, G. Qian, K. Yang, Y. Cui, H. Chen, F. Pan, *Small* **2019**, 15, 1904545.

[120] J. Huang, Z. Wang, M. Hou, X. Dong, Y. Liu, Y. Wang, Y. Xia, *Nat.*

Commun. **2018**, 9, 2906.

[121] Q. Zhao, W. Huang, Z. Luo, L. Liu, Y. Lu, Y. Li, L. Li, J. Hu, H. Ma, J. Chen, *Sci. Adv.* **2018**, 4, eaao1761.

[122] P. He, Y. Quan, X. Xu, M. Yan, W. Yang, Q. An, L. He, L. Mai, *Small* **2017**, 13, 1702551.

[123] F. Ming, H. Liang, Y. Lei, S. Kandambeth, M. Eddaoudi, H. N. Alshareef, *ACS Energy Lett.* **2018**, 3, 2602.

[124] N. Zhang, Y. Dong, M. Jia, X. Bian, Y. Wang, M. Qiu, J. Xu, Y. Liu, L. Jiao, F. Cheng, *ACS Energy Lett.* **2018**, 3, 1366.

6. 국 문 초 록

기존 상용 리튬이차전지는 높은 에너지밀도로 인해 이차전지 시장에서 우세한 점유율을 보이고 있으나, 화재로 인한 폭발의 위험이 여전히 존재한다는 단점이 있다. 화재 위험으로부터 안전을 확보하기 위해 일명 차세대 이차전지로 불리는 대안 기술의 연구가 활발히 이루어지고 있으며, 일례로 수계 아연 이차전지를 들 수 있다. 수계 이차전지는 물 기반의 수용액을 전해질로 채용하는 기술로, 유기 전해액을 사용하는 리튬이차전지와 달리 화재의 위험을 최소화할 수 있다는 것이 가장 큰 장점이다. 내부 단락이 일어날 경우, 순간적인 발열로 인한 화재가 발생될 수 있는데, 유기 전해액은 높은 발화성으로 인해 폭발로 이어질 수 있다. 그러나, 수계 전해액은 발화성이 없기 때문에 비교적 안전한 차세대 이차전지 기술로 평가받고 있다. 수계 아연 이차전지의 구성은 리튬 이차전지(반쪽 셀)와 유사하나, 관련 연구는 기초 연구 단계에 머무르고 있어 여러 기술적인 문제와 직면하고 있다. 이를 극복하기 위해 최근 다양한 연구가 활발히 진행되고 있으며, 크게 양극과 음극이 주축을 이룬다.

제 2 장에서는 수계 아연 이차전지용 양극재의 합성, 평가, 분석 연구에 대해 기술하고 있다. 아연 이온(Zn^{2+})과 가역적인 탈/삽입 반응을 보이는 양극 재료의 발굴 및 분석 연구가 주요 방향으로 자리잡고 있다. 전이금속 산화물이 가장 유망한 재료군으로 꼽히는 가운데, 망간(Mn)과 바나듐(V) 기반의 산화물이 높은 비중을 차지한다. 특히, 다양한 상을 형성할 수 있는 바나듐 산화물이 중점적으로 보고되고 있다. 본 연구에서는 Zn^{2+}를 가역적으로 탈/삽입할 수 있는 V_6O_{13} 양극재를 발굴하여 합성, 전기화학 평가, 분석, DFT 계산을 토대로 해당 재료의 성능을 평가하고 기초 현상을 규명한다. 전기화학 측면에서 V_6O_{13} 양극재는 높은 용량, 고율 특성, 긴 수명이 장점으로 평가된다. 또한, 방사광 가속기 시설을 활용하여 실시간 XRD 분석을 진행한 결과, 충/방전시 단일상 반응(single-phase reaction)을 통해 Zn^{2+}의 탈/삽입이 이루어지는 것으로 확인된다. 특히, 추가 분석과 DFT 계산으로부터 물의 역할이 중요하게 작용하는 것으로 파악되며, 일명 “수화 삽입” 기작을 통해 Zn^{2+} 이온의 탈/삽입을 원활하게 유도하는 현상이 발견됐다. 수화 삽입은 물 분자와 Zn^{2+} 이온이 배위된 상태로 V_6O_{13} 의 결정 내로 삽입 되는 현상으로, 두 가지 역할을 수행한다. 계면에서는 Zn^{2+} 이온의 de-solvation 으로 인한 과전압을

낮춰주며, 결정 안에서는 전하 이온과 모상의 정전기적 작용을 막아주어, 다가 이온임에도 불구하고 우수한 전기화학 특성을 보인다.

제 3 장에서는 Zn 음극에 대해 중점적으로 기술하고 있다. 초기 수계 아연 이차전지 관련 연구는 양극재에 치중하는 경향이 있었으나, 최근에는 Zn 금속 음극에 집중하는 추세이다. 양극 관련 연구에서는 음극의 영향을 배제하고 양극 활물질의 전기화학 특성에 집중하기 위해 음극을 과량으로 사용하게 된다. 음극의 비가역성으로 인한 전지의 성능 저하를 방지하는 셈이다. 그러나 음극을 과량으로 사용할 경우 상당한 중량/부피당 에너지밀도의 손실이 불가피해지며 실용성이 떨어진다. 따라서, 음극을 최소화하는 동시에 높은 성능을 구현하는 것이 핵심이며, 이는 음극의 가역성이 확보되어야 한다는 것을 의미한다.

Zn 금속은 표준환원전위, 수소 발생 억제, 가격 경쟁력, 친환경성 등 여러 측면에서 수계 환경에 적합한 음극 물질로 사료된다. 그러나 전기화학 거동 중에 발생하는 미시적인 현상이 Zn 음극의 성능을 저하시키게 된다. 이는 대부분 계면 현상으로부터 발생된다. 예컨대, 전류 밀도에 따라 Zn 금속 표면에서의 수소 발생 반응이

우세해질 수 있고, Zn 의 전착이 균일하지 못하여 수지상 형태로 성장할 수 있으며, 장기간 노출시 부식 반응이 동반될 수 있다. 많은 연구에서 양극재에 치중되어 앞서 기술된 음극의 잠재적인 문제를 중점적으로 다루지 않고 있다. 따라서, 제 3 장에서는 Zn 음극의 장/단점과 Zn의 전/탈착 과정에 대해 상세히 서술하고 있다. 또한, 최근까지 보고된 Zn 음극의 가역성을 확보하기 위한 각종 전략에 대한 요약과 고찰을 제시하고 있으며, 상황별 계산을 통해 초기 Zn 의 양과 전/탈착 효율이 에너지밀도에 막대한 영향을 미치는 것으로 판단된다. 그러므로 Zn 의 가역성이 최우선적으로 보장되어야 초기 사용량을 최소화할 수 있고, 향상된 에너지밀도로 이어질 수 있다. 결론적으로, 제 3 장에서는 수계 아연 이차전지의 실용성을 확보하기 위한 필수 조건과 여러 전략의 핵심을 전달함으로써 접근 방향을 제시하고 있다.

List of publications

International Publications

International Peer-Reviewed Journals (First Author)

1. **J. Shin** and J. W. Choi, "Opportunities and Reality of Aqueous Rechargeable Batteries" *Advanced Energy Materials*, *accepted***.**
2. **J. Shin**, J. Lee, Y. Park, and J. W. Choi, "Aqueous Zinc Ion Batteries: Focus on Zinc Metal Anodes" *Chemical Science*, **2020**, 11, 2028-2044.
3. **J. Shin***, D. S. Choi*, H. J. Lee, Yousung Jung, and J. W. Choi, "Hydrated Intercalation for High-performance Aqueous Zinc Ion Batteries" *Advanced Energy Materials*, **2019**, 1900083 (*Co-first author)

International Peer-Reviewed Journals (Co-author)

1. H. J. Kim, Y. Park, Y. Kwon, **J. Shin**, Y. –H. Kim, H. –S. Ahn, R. Yazami, and J. W. Choi. Entropymetry for non-destructive structural analysis of $LiCoO_2$ cathodes. *Energy & Environmental Science*, **2020**, 13, 286-296.
2. S. E. Jerng, T. Y. Kim, S. Bae, **J. Shin**, J. Park, and J. W. Choi. "Lewis acidity controlled heme catalyst for lithium-oxygen battery" *Energy Storage Materials*, **2019**, 19, 16-23.
3. J. H. Lee, H. J. Lee, S. H. Choi, **J. Shin**, S.-Y. Chung, and J. W. Choi. "Superlattice formation of crystal water in layered double hydroxides for long-term and fast operation of aqueous rechargeable batteries" *Advanced Energy Materials*, **2018**, 1703572.
4. S. B. Patil†, H. J. Kim†, H.-K. Lim, S. M. Oh, J. Kim, **J. Shin**, H. Kim, J. W.

Choi, and S.-J. Hwang. “Exfoliated 2D Lepidocrocite titanium oxide nanosheets for high sulfur content cathodes with highly stable Li-S battery performance” *ACS Energy Letters*, **2018**, 3, 412-419.

5. H. J. Lee, **J. Shin**, and J. W. Choi. “Intercalated water and organic molecules for electrodes of rechargeable batteries” *Advanced Materials*, **2018**, 1705851.
6. I. H. Son, J. H. Park, S. Park, K. Park, S. Han, **J. Shin**, S.-G. Doo, Y. Hwang, H. Chang, and J. W. Choi. “Graphene balls for lithium rechargeable batteries with fast charging and high volumetric energy densities.” *Nature Communications*, **2017**, 8, 1561.
7. D.-J Yoo†, J.-S. Kim†, **J. Shin**, and J. W. Choi. “Stable performance of aluminum metal battery by incorporating lithium ion chemistry” *ChemElectroChem*, **2017**, 4, 2345-2351.
8. S. Y. Lim, J. H. Lee, S. Kim, **J. Shin**, W. Choi, K. Y. Chung, D. S. Jung, and J. W. Choi. “Lattice water for the enhanced performance of amorphous iron phosphate in sodium-ion batteries” *ACS Energy Letters*, **2017**, 2, 998-1004. .
9. J. Park, E. T. Kim, C. Kim, J. Pyun, H.-S. Jang, **J. Shin**, J. W. Choi, K. Char, and Y.-E. Sung. “The importance of confined sulfur nano-domains and adjoining electron conductive pathways in sub-reaction regimes of Li-S batteries” *Advanced Energy Materials*, **2017**, 7, 1700074.
10. B. G. Kim, C. Jo, **J. Shin**, Y. Mun, J. Lee, and J. W. Choi. “Ordered mesoporous titanium nitride as a promising carbon-free cathode for aprotic lithium-oxygen batteries” *ACS Nano*, **2017**, 11, 1736-1746.
11. Y. Zhu†, S. H. Choi†, X. Fan, **J. Shin**, Z. Ma, M. R. Zachariah, J. W. Choi, and C. Wang. “Recent progress on spray pyrolysis for high performance

electrode materials in lithium and sodium rechargeable batteries" *Advanced Energy Materials*, **2017**, 7, 1601578.

12. T. Yim, N. H. Park, M.-S. Park, S. H. Han, J. H. Lee, **J. Shin**, J. W. Choi, Y. Jung, Y. N. Jo, J.-S. Yu, and K. J. Kim. "Effective polysulfide rejection by dipole-aligned $BaTiO_3$ coated separator in lithium-sulfur batteries" *Advanced Functional Materials*, **2016**, 26, 7817-7823.
13. S. Kim, S. Lee, K. W. Nam, **J. Shin**, S. Y. Lim, W. Cho, K. Suzuki, Y. Oshima, M. Hirayama, R. Kanno, and J. W. Choi. "On the mechanism of crystal water insertion during anomalous spinel-to-birnessite phase transition." *Chemistry of Materials*, **2016**, 28, 5488-5494.
14. J.-S. Kim, Y.-H. Lee, S. Choi, **J. Shin**, H.-C. Dinh, and J. W. Choi. An electrochemical cell for selective lithium capture from seawater. *Environmental Science and Technology*, **2015**, 49, 9415-9422.

Patents

1. 최장욱, 신재호 이차전지, 특허 제 10-2091802호 (2020. 03. 16) (특허 출원 10-2018-0119191, 2018.10.05)